OPTIMIZATION, CONTROL, AND IMPLEMENTATION OF CO_2 TRANSCRITICAL AIR CONDITIONING SYSTEMS

By

Ahmed Ali Okasha

A DISSERTATION

Submitted to
Michigan State University
in partial fulfillment of the requirements
for the degree of

Mechanical Engineering—Doctor of Philosophy

2020

ABSTRACT

OPTIMIZATION, CONTROL, AND IMPLEMENTATION OF CO_2 TRANSCRITICAL AIR CONDITIONING SYSTEMS

By

Ahmed Ali Okasha

The US EPA listed R134a as unacceptable refrigerant for newly light-duty vehicles manufactured or sold in the United States as of model year 2021. Carbon dioxide CO_2 (R744) has been revived as a natural environmentally friendly refrigerant and is considered a strong alternative to R134a as it has a global warming potential (GWP) of 1 compared to 1300 for R134a. In an air-conditioning system and due to the different thermodynamic properties of CO_2, the heat rejection process at the high-pressure side will take place above the critical point for high ambient/sink temperatures. Therefore, for a given ambient temperature, the GC pressure (high-side pressure) can be optimized and controlled independently. Either through simulations or experiments, researchers have been focusing on developing control correlations for the GC pressure to maximize the COP using offline control correlations or online methods. Maximizing COP does not mean that the system is working at its highest cooling/heating capacity that might be desired for example in a transient start-up operation to cool down or heat up the car cabin in the shortest possible time. In addition, offline control correlations suffer deviation from the true optimum as they rely on the system model. Online methods, on the other hand, can be more accurate but often lack the fast convergence to the optimum solution. The aim of this thesis was to develop a new strategy to optimize and control the CO_2 transcritical air conditioning system for not only optimum COP, but also optimum cooling/heating capacity or a tradeoff solution based on the system state i.e. transient, steady state, or capacity demand. To find the Pareto Front or the best non-dominated solutions between the COP and the cooling capacity for any set of operating conditions, the existing Non-Dominated

Sorting Genetic Algorithm II (NSGA-II) is used, and the results are generated based on a transcritical CO_2 thermodynamic model. The best solutions of both objectives COP and cooling capacity are presented by a Pareto Front for a given operating conditions. Each solution of the Pareto Front has a unique GC pressure and superheat. An optimization parameter k that ranges from 0 to 1 is introduced to easily select maximum COP, maximum cooling capacity, or any of trade-off solutions. Based on the system operating conditions, the high-level optimizer signals the system actuators, the GC pressure, and superheat reference values. The proposed optimization and control approach can be employed as a hybrid offline and online strategy. Based on the current operating conditions, the high-level optimizer will provide an initial estimate of the optimum solution to the online optimizer, which will start searching for the true optimum online from this close initial guess. An optional online optimizer can be integrated in the loop e.g. before the controller, resulting in conjunction with the offline optimizer in a hybrid solution. Such hybrid solution can reduce the time to approach the desired operating point compared to online only methods. Compared to offline only methods, this can additionally enhance COP and $\dot{Q}_c$ based on the actual system characteristics, while it is also able to adapt to changing system characteristics. While the results in this thesis are presented in terms of the cooling capacity, the same findings can be applied for the heating capacity. For further experimental investigations of the transcritical cycle, a modular transcritical CO_2 heat pump system and its coolant system have been constructed at the MSU Turbomachinery Lab that support cooling, heating, and dehumidification modes. Several parameters' effects on the system performance have been analyzed and the experimental results are reported.

To my beloved Father, Mother, and Brother
Ali, Mona, and Mohamed,
Thank you for your unlimited love, patience, and support

ACKNOWLEDGEMENTS

In the name of Allah, the most Merciful and Beneficent. All praise is due to God (Allah) Almighty, the Lord of the world, the Master of day of Judgement, for the all the blessing, the strength, and the determination to successfully complete this thesis work.

My sincere gratitude goes to my main adviser, Prof. Norbert Müller for his constant support and motivation from the early stage of my research. I thank him a lot for all the hours of meetings; his judgment of my work; and his clear and persuasive, directions, comments, and feedback.

A big thanks to Ford Motor Company for their generous support of this research and special thanks to Ford PI, James Gebbie, for his immense feedback and insights on my work from the early stage of the project. Likewise, I thank James Dyson Foundation for the Fellowship award while I was working on this research work.

Many thanks to Prof. Kalyanmoy Deb whom I learned a lot from his evolutionary multi-objective class at MSU and for his time and fruitful discussions on my thesis optimization portion. His innovative way of teaching made me love optimization and evolutionary methods. In addition, I extend my sincere gratitude to Prof. Abraham Engeda and Prof. Neil Wright for their support and encouragement of this work and being in this thesis committee.

Special thanks to my brother Mohamed for his help in designing the control circuits for the variable frequency drivers. I must also acknowledge Duy Nguyen, Ian Albert, Do Thong, and Basil Ahmed for their support in the experimentation. Many thanks to Haitham Seada for the several discussions on the multi-objective optimization. Thanks to Younis Najim for his guidance during the early stage of this work. Special thanks to Prof. Craig Gunn for his time in revising my technical writing documents.

I would also like to extend my sincere appreciation to Michigan State University for making all the needed resources available and for the constant support, learning activities, and guidance to be a better researcher.

Many thanks to all my Egyptian friends in the East Lansing area for the help and support they provided whenever I needed.

Finally, my deepest gratitude goes to my father Ali, my mother Mona, and my brother Mohammed for all the sincere love, tremendous patience, and unlimited support they offered me.

TABLE OF CONTENTS

LIST OF TABLES

LIST OF FIGURES

KEY TO ABBREVIATIONS

BPHE	Brazed plate heat exchangers
COP	Coefficient of performance
d	Distance
EPA	Environmental protection agency
EXV	Electronic expansion valve
G	Gain
GC	Gas cooler
GWP	Global warming potential
HEX	Heat Exchanger
HTF	Heat transfer fluid
IHX	Internal heat exchanger
ISO	International organization for standardization
L	Loss
N	Number of population
O	Offspring population
Obj	Objective
ODP	Ozone depletion potential
OHEX	Outside heat exchanger
OS	Oil Separator
P	Parent population
PAG	Polyalkylene Glycol

PI	Proportional-integral
POE	Polyolester
R	Lumped parent and offspring population
ref	reference
RTD	Resistance temperature detector
SG	Specific gravity
sub	Subcritical
sup	Supercritical
VFD	Variable frequency drive
VG	Viscosity grade

KEY TO SYMBOLS

1,2, etc.	Thermodynamic state points, [-]
A	Tube/pipe cross sectional area, [m^2]
c_p	Isobaric specific heat capacity, [J/(kgK)]
C_v	Valve flow coefficient, [-]
D_i	Inner tube diameter, [m]
D_o	Outer tube diameter, [m]
f_D	Darcy friction factor, [-]
g	Gravitational constant, [m^2/s]
h	Specific enthalpy, [J/kg]
h_{fg}	Latent heat of vaporization, [J/kg]
k	Bi-Objective optimization index, [-]
K	Factor for the 3K pressure drop calculation method, [-]
K_1, K_d, and K_∞	Constants extracted from tables for the 3K method, [-]
m	Refrigerant charge, [kg]
Nu	Nusselt number, [-]
p	Pressure, [bar or psi]
P	Power, [W]
Pr	Prandtl number, [-]
q	Volumetric flow rate, [GPM or m^3/s]
Q_v	Volumetric refrigeration capacity, [kJ/m^3]
Re	Reynolds number, [-]

r_p	Compressor pressure ratio, [-]
s	Specific entropy, [kJ/(kgK)]
T	Temperature, [°C or K]
v	Specific volume, [m^3/kg]
V	Volume, [m^3 or gallon]
V_d	Compressor displacement (swept volume), [m^3]
x	Vapor quality, [-]
y	Energy balance variable, [-]
Y	Constant which collects fixed parameters related to the geometry and operating conditions [kW^2/m^4]
$\dot{m}$	Refrigerant mass flow rate, [kg/s]
$\dot{Q}$	Capacity, [kW]
$\dot{W}$	Work per unit time (Power), [kW]
Δ	Difference, [-]

Greek

α	Constant of the compressor isentropic efficiency [-]
β	Slope of the compressor isentropic efficiency [-]
η	Efficiency, [-]
μ	Dynamic viscosity, [N.s/m^2]
ρ	Density, [kg/m^3]
υ	Flow speed, [m/s]
ω	Compressor speed, [rpm]

Subscripts

amb	Ambient
avg	Average
C	Cooling
comp	Compressor
cr	Critical
dis	Discharge
Evp	Evaporation
GCo	Gas cooler outlet temperature
H	Heating
i	Index
in	Inlet
is	Isentropic
opt	Optimum
out	Outlet
r	Refrigerant
ref	Reference
sat	Saturation
sh	Superheat
sp	Set-point
sub	Subcritical
sup	Supercritical

t	Current generation
v	Volumetric

Chapter 1: Introduction

1.1 Background

No matter where we live on earth, heat pumps form an essential and central part of our daily lives. A heat pump is a device that uses energy to move heat from one place to another using a refrigerant. Heat pump is a broad term that involves cooling or heating depending on the cycle's desired objective. For refrigeration, cooling, or air conditioning applications, the refrigerant pulls the heat from the cold refrigerated space (For example: a room or a passenger compartment) and rejects the heat to an outside warm environment. In the heating mode, the refrigerant picks up and transfers the heat from the outside environment to the heated space. Heat pumps are used widely in residential and commercial buildings, automotive, hospitals, theaters, restaurants, industrial processes, vending machines, and many other applications.

Heat pump operation is based on a typical vapor compression cycle that is shown in Figure 1-1. The main components of a heat pump system for either cooling or heating applications consist of a compressor, a condenser, an expansion device, and an evaporator. For the cooling mode cycle, the refrigerant enters on the suction side of the compressor at state 1 as a low temperature, low pressure, and saturated vapor and goes under isentropic compression to the condenser pressure. Vapor refrigerant exits the compressor at a temperature well above the outside environment or the surrounding medium. Refrigerant then enters the condenser as a superheated vapor at state 2, rejecting heat to the environment at a constant pressure, and leaves the condenser as saturated liquid at state 3. The expansion device then throttles the refrigerant, reducing its pressure to the evaporator pressure as well as dropping the temperature below the refrigerated space temperature. The expansion device can be a fixed area such as a capillary tube or an orifice, manually adjustable by a needle valve or metering valve, thermostatic, or electronically adjustable one by a stepper/servo motor. The refrigerant then enters the evaporator at state 4 as a mixture and evaporates while absorbing heat from the refrigerated space. The refrigerant leaves the evaporator as a saturated vapor at state 1 and the cycle repeats. For a heating mode, the cycle is similar; however, the refrigerant will reject heat from the condenser to the heated space and picks up heat through the evaporator from the outside environment.

There are several kinds of refrigerants, the selection of which depends on aspects such their thermodynamic and transport properties; their environmental impact, which includes their influence on global warming and the ozone layer; and properties such as toxicity and flammability.

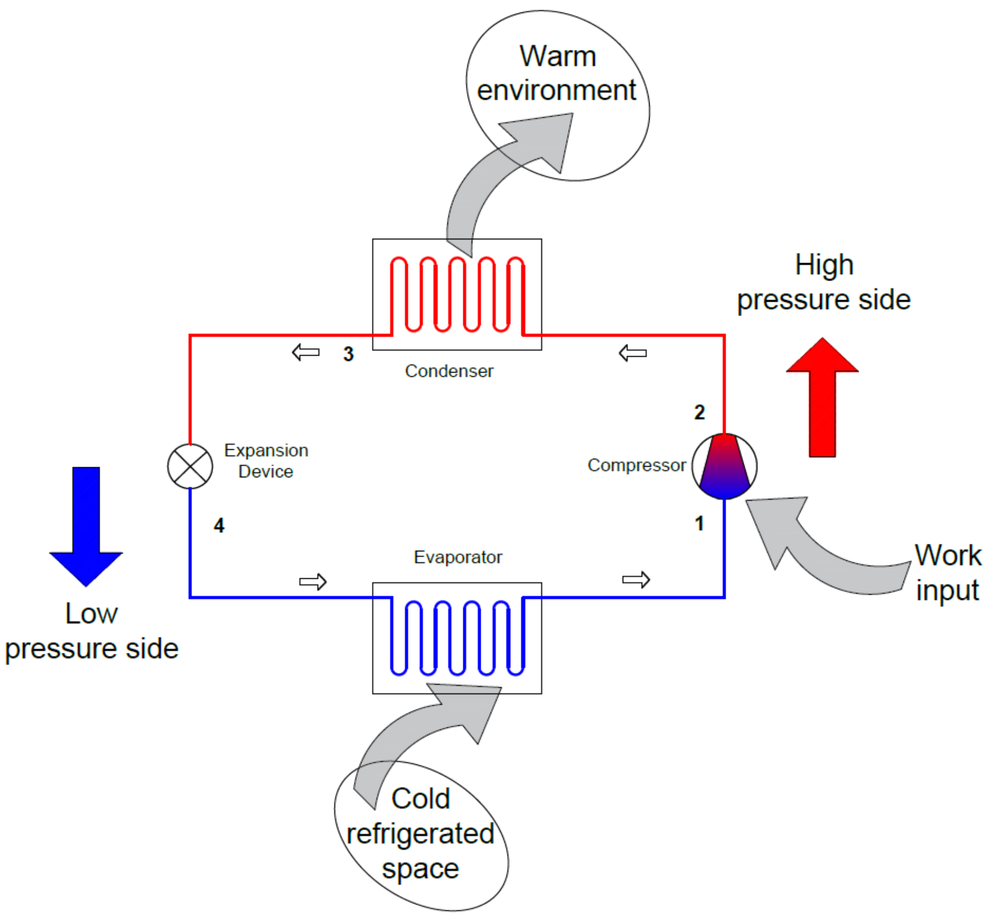

Figure 1-1. Heat pump cycle and its main components for the refrigeration, cooling, or air conditioning mode

Refrigerants can be categorized into two main types: synthetic and natural. Chlorofluorocarbons (CFCs), Hydrochlorofluorocarbons (HCFCs), and Hydrofluorocarbons (HFCs) are examples of synthetic refrigerants; while common natural refrigerants include air, water (R718), ammonia (R717), and carbon dioxide, CO_2 (R744).

Chlorofluorocarbons (CFCs) refrigerants were developed in the 1930s and contain Chlorine, Fluorine, and Carbon, such as R12 (brand name Freon 12). CFCs are non-toxic and non-flammable and were used in various industrial, commercial, and automotive applications. In 1973, it was revealed that when CFCs reach the upper atmosphere and get exposed to ultraviolet rays, they break down into base substances. The chlorine reacts with the oxygen atoms in the ozone and break apart the ozone molecule. Molina & Rowland [1] revealed that the chlorine emissions damage the ozone layer; and since then, governments and industrial firms began to phase out CFC refrigerants. One atom of chlorine can destroy more than a hundred thousand ozone molecules according to the U.S. EPA. Destruction of the ozone leads to what is known as the "Ozone Hole." Ozone is naturally formed in the atmosphere and it absorbs the sun's harmful ultraviolet rays. The ozone hole increases the risk of skin cancer and weakens the human immune system leading to diseases and other environmental effects. Ozone depletion potential (ODP) is a term introduced in 1983 that defines the relative amount of degradation to the ozone layer it can cause, with R11 refrigerant being fixed at an ODP of 1.0. Montreal Protocol [2] placed a regulation to phase out the production of numerous substances that were responsible for ozone depletion.

1.2 Global Warming Potential

Hydrochlorofluorocarbons (HCFCs) (which contain Hydrogen, Chlorine, Fluorine, and Carbon), pose only 10% of the ODP compared to CFCs. However, HCFCs are among the greenhouse gasses that have high global warming concerns. The energy from the sun reaches the earth as solar radiation. While some of the radiation is reflected by the earth and the atmosphere, most of the radiation is absorbed by the earth. The earth emits infrared radiation, some passes through the atmosphere, but a portion get trapped by the greenhouse gases making the earth's surface warmer than it would be. This destroys the energy balance of the earth and causes climate changes. The global warming potential (GWP) is an index that measures how much energy the emissions of 1 ton of a gas will absorb over a given period of time relative to the emissions of 1 ton of carbon dioxide (CO_2) over 100-year period [3].

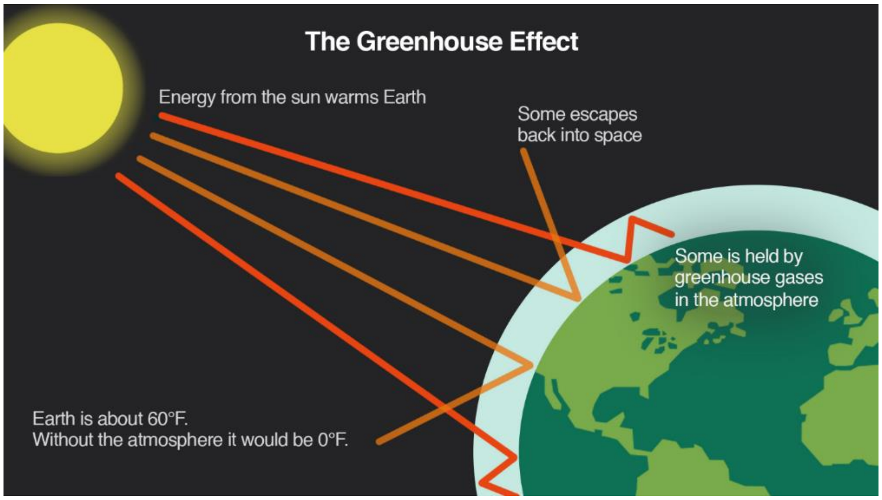

Figure 1-2. The greenhouse effect. Credit: climatecentral.org.

Hydrofluorocarbons (HFCs) that contain Hydrogen, Fluorine, and Carbon do not have any ODP; and although they have lower GWP than HCFCs, their GWP is still relatively large in the range 1300-1900. According to the Intergovernmental Panel on Climate Change (IPCC) [4], which includes more than 1,300 scientists, a forecast of a temperature rise of 2.5 to 10 degrees F (over the next century is predicted due to greenhouse gases. Figure 1-3 shows the increase in the average annual global temperatures since 1880. NASA [5] projects the long-term effects associated with climate change to be (1) Temperatures will continue to rise, (2) Hurricanes will become stronger and more intense, (3) Increased droughts and heat waves, (4) Sea level will rise 1-4 feet by 2100 and (5) The Arctic Ocean is expected to become essentially ice free in summer before mid-century. As a matter of fact, some of these effects have been more obvious in the past few years. The intensity, frequency, and duration of North Atlantic hurricanes, as well as the frequency of Category 4 and 5 hurricanes have all increased in the last decade. Hurricane Irma in 2017 was a Category 5 storm peaked with 180 mph winds, caused widespread and devastating damage throughout the Caribbean and the Florida Keys. In southern Texas, Hurricane Harvey barreled down as a Category 4 storm and caused extensive flooding in the Houston metro area.

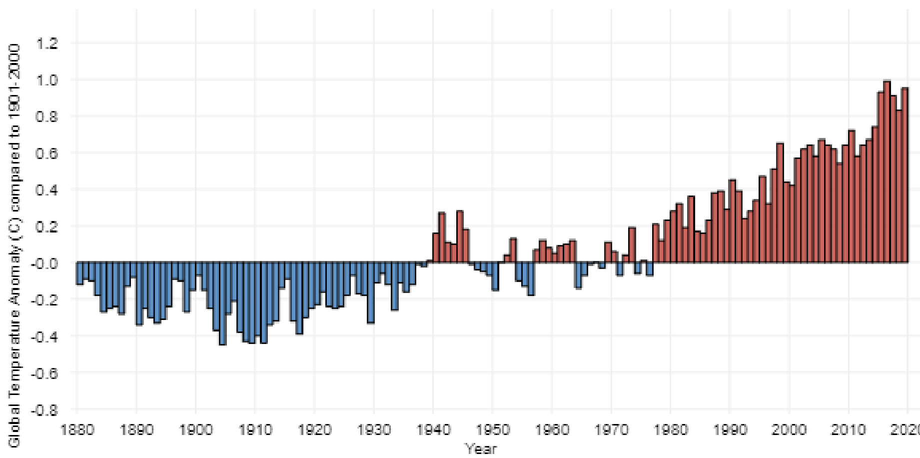

Figure 1-3. The average annual global temperatures since 1880. Credit: www.climate.gov

1.3 Motivation behind using CO_2 as a refrigerant

1.3.1 Unity GWP

Under Kyoto protocol regulations [6] (adopted in 1997 and entered into force in 2005), the phasing out of HFC refrigerants is underway due to their global warming concerns. In 2015, the US EPA listed R134a as unacceptable refrigerant for newly manufactured light-duty vehicles manufactured or sold in the United States as of model year 2021. The regulations are pushing to actively look for a long-term, environmentally friendly alternative refrigerant. Ammonia (R717), although it has zero ODP and GWP, is highly flammable and toxic. Water (R718) has two main disadvantages:

first its high freezing point limits the evaporation temperature to be above 0 °C, and secondly it requires compressors to be able to handle large volume flows and high pressure ratios due to its low operating pressures and vapor density [7]. Hydrocarbons such as propane (R290) are highly flammable and can be explosive. Carbon dioxide (CO_2 or R744) on the other hand is a non-flammable, non-toxic fluid that has zero ODP and GWP of unity, which is negligible compared to 1300 of R134a. Table 1-1 summarizes environmental impact characteristics of CO_2 and other common refrigerants.

Table 1-1. Environmental impact characteristic of common refrigerants

Refrigerant	**Type**	**Chemical Formula**	**ODP**	**GWP**	**Flammable**	**Toxic**
R12	CFC	CCl2F2	1	2400	No	No
R22	HCFC	CHClF2	0.05	1700	No	No
R134a	HFC	CF3CH2F	0	1300	No	No
R410a	HFC blend	50%CH_2F_2/50%CHF_2CF_3	0	2000	No	No
R1234yf	HFO	C3H2F4	0	4	Yes	No
R717 (Ammonia)	Natural ref.	NH3	0	0	Yes	Yes
R774	Natural ref.	CO_2	0	1	No	No

1.3.2 Heating Mode for Electric Vehicles

Vehicles powered by internal combustion engines use the waste heat from the coolant to heat the passenger compartment. They also use the engine to run the air conditioning compressor. Modern cars with fuel-injection engines often have insufficient waste heat for heating of the passenger compartment in the winter season. The long heating-up period and slow defroster action is unacceptable both in terms of safety and comfort. Supplementary heating is therefore necessary, and one attractive solution may be to operate the heat pump in the heating mode. On the other hand, electric vehicles rely exclusively on the energy stored in their batteries for heating and cooling since there is no engine to power the AC. The more efficient those systems are, the longer the mileage range the vehicle can make. Many electric vehicles rely on old fashioned resistance heaters to warm the passenger compartment. It is effective but uses a lot of electricity to meet the desired heating capacity or the desired temperature set point. To illustrate, electric heaters provide heating energy output equal to the electric energy input. For example, if the cabin heating demand is ~3 kW, the electric heater will consume 3 kW (or more due to the losses) regardless of the ambient and set point operating conditions; hence the efficiency is ideally 1. On the other hand, for a CO_2 air conditioning system running in the heating mode and to meet a heating demand of 3 kW for a system running at -20 °C ambient temperature, the system will have COP of ~3, thus, consuming only 1 kW of power compared to 3 kW which is one third the energy demand. Although similar COP can be achieved with other refrigerants, CO_2 systems have other benefits in the heating mode due to the compression high discharge pressure and temperature, high capacity and COP can be achieved also at low ambient temperatures and the high outlet temperature will allow instant defrosting of automobile windshields.

1.3.3 Smaller Component Weight

The operating pressure encountered in CO_2 air conditioning systems is significantly higher than other traditional refrigerants, up to around 10 rimes. High pressure means higher density for any fluid, which leads to higher refrigeration capacity (which is the product of the vapor density times the latent heat of vaporization). Therefore, a volume amount of CO_2 refrigerant can transport much more heat compared to traditional refrigerant with the same volume. It also means that CO_2 can transport the same amount of heat with much less volume; and, hence, we can use smaller and more compact components, therefore, allowing miniaturization of the systems for the same heat pumping power requirements.

1.4 Thesis Structure

This thesis is structured as follows. In Chapter 2, we explore the history of using CO_2 as a refrigerant, highlight the important CO_2 thermophysical properties, and then introduce the transcritical cycle and emphasize the main differences compared to the conventional subcritical heat pump cycle. Afterwards, we detail the state-of-the-art CO_2 transcritical systems and mention the main contribution(s) of previous works; and most importantly, critically assesses their methods and strategies. We conclude the chapter by pointing out the open issues and presenting the thesis work contributions.

Chapter 3 presents the transcritical cycle thermodynamic modeling and evaluates the effects of the several system parameters on the cycle performance. We present the developed volumetric and isentropic efficiency correlations for the commercial compressor used in the experimental test rig. We also present the developed offline control correlation to optimize the COP for the cycle that relates the GC pressure to the GC outlet temperature, which is the most dominant factor.

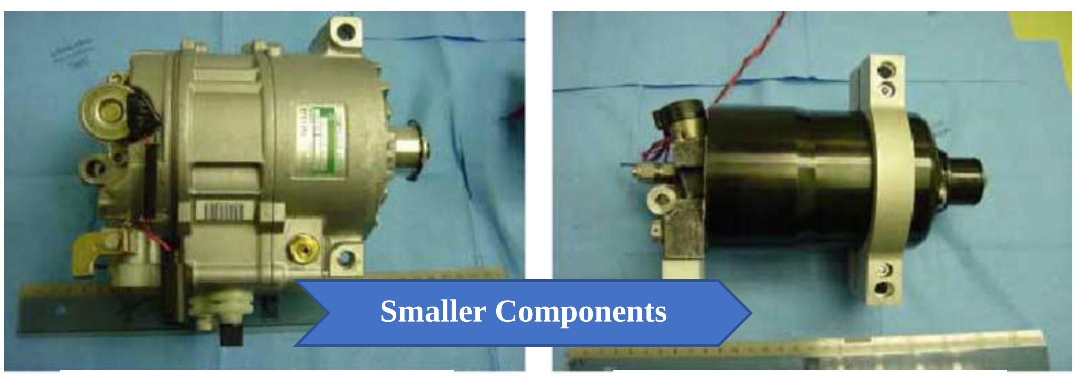

R134a compressor CO2/R744 compressor

Figure 1-4. Two compressor photographs of R134a and CO_2/R744 showing the reduction in volume and space required. Credit: Kim, et al. [2004]

Chapter 4 introduces the new developed optimization and control technique for the CO_2 transcritical cycle based on the Non-dominated Sorting Genetic Algorithm II. The algorithm is used to study the trade-off between the COP and the cooling capacity, generating for different operating conditions the best non-dominated solutions or the Pareto Front. The effect on the Pareto Front of each optimization variable is shown and discussed separately. A control methodology is proposed where according to a pre-defined preference, steady-state or transient operation, an optimization parameter is set to either maximize cooling or heating capacity (for obtaining comfort as soon as possible in transient operation), maximize COP (for minimum energy consumption) or operate at a trade-off point as desired.

Chapter 5 details the experimental apparatus by presenting the schematics for the CO_2 and the HTF for cooling, heating, and two dehumidification modes. We also describe the simulations and the selection criteria for the different components including the compressor, plate heat exchangers, expansion device, suction line accumulator, oil separator, valves, and tubing components. We show the sizing of the HTF loops based on steady-state and transient capacities. The instrumentation and various sensors used for acquiring the systems measurement signals are also presented.

Chapter 6 presents the testing method, validation, and experimental results. We investigate the effect of various parameters on the COP including HTF GC outlet and evaporator inlet temperatures, the CO_2 mass flow rate, and the useful superheat.

Chapter 7 contains the conclusions from the thesis findings and discuss several future research pathways.

Chapter 2: Literature Review

2.1 Rise - Decline - Revival of CO_2 as a Refrigerant

CO_2 was first presented as a refrigerant for vapor-compression systems through a British patent in 1850 by Alexander Twining [8]. In 1867, Thaddeus Lowe earned a patent after conducting experiments and confirming the possibility of using CO_2 as a refrigerant. Carl Linde designed a CO_2 machine for a German company in 1882. W. Raydt received a patent in 1884 for a compression CO_2 ice-making machine. Significant progress was made when Franz Windhausen invented a CO_2 compressor, which was patented in 1886. The patent was acquired by the J&E Hall Company in Great Britain and a CO_2-based marine plant was built in 1890, which received broad attention. In the United States, CO_2 started to be used in the 1890s in refrigeration systems such as supermarkets, kitchens, and small cold storage systems; and since the 1900s it has been used in comfort cooling applications such as hospitals, theaters, and restaurants [3].

In the 1940s, the marketing for CFC refrigerants led to phasing out the existing refrigerants, including CO_2. By 1960, CO_2 had been almost completely replaced in marine-based systems. There are several reported reasons for why CO_2 has been phased out at that time as reported in [3]

- The capacity and COP loss at high temperatures (Most likely because CO_2 transcritical cycle was not studied and optimized sufficiently at that time)
- The high working pressures and the need to redesign the system
- The unsuccessful trials of CO_2 system manufacturers to improve and modernize the design of machinery and equipment
- The aggressive marketing of CFC products

The revival of CO_2 was initiated in the late 1980s when Lorentzen [9] introduced a breakthrough patent that showed that the high-side pressure in the CO_2 transcritical cycle can be controlled by a throttling valve. Lorentzen & Pettersen [10] created a prototype CO_2 automotive AC for comparison with an R12-based system with equivalent capacity. Since then, the automotive industry become actively engaged in conducting further studies on CO_2 systems. As reported by [11], the European RACE project that included car manufacturers (BMW, Daimler-Benz, Rover, Volvo, and Volkswagen), along with system suppliers (Behr and Valeo), and the compressor manufacturer (Danfoss) developed and tested from 1994 to 1997 a car-installed prototype system, with results confirming the potential for CO_2-based car air conditioning. BMW, Audi, and DaimlerChrysler showed consistent results through independent studies.

2.2 Thermophysical Properties

Besides the refrigerant environmental aspects, the cycle-efficient operation and component design are among the other criteria for the refrigerant selection. Understanding refrigerant thermophysical properties including thermodynamic properties (vapor pressure, enthalpy, etc.), and transport properties (thermal conductivity and viscosity) are important for design analysis and optimization. Most of the upcoming discussion and analysis is inspired from [3] and [12]. All the properties and plots are calculated in MATLAB using NIST REFPROP database [13].

Table 2-1 shows comparison of selected thermodynamic properties for various refrigerants. CO_2 distinguishes itself from common refrigerants by its relatively low critical temperature and high critical pressure of 31.1 °C and 73.8 bar respectively. Hence, for a CO_2 heat pump cycle, the heat rejection process at the high-pressure side will take place above the critical point for high ambient/sink temperatures. This area is called the "supercritical" region where there is no clear distinction between gas/vapor and liquid. This area is highlighted in red in the p-h diagram in red in Figure 2-1.

Table 2-1. Thermodynamic properties & refrigeration capacity of common refrigerants

Refrigerant	**Critical pressure (bar)**	**Critical temperature (°C)**	**Triple point temperature (°C)**	**Vapor density at 20 °C (kg/m3)**
R12	41.4	112.00	-157.05	17.9
R22	51.0	96.15	-157.42	21.2
R134a	40.6	101.06	-103.30	14.4
R410a	49.0	71.34	-73.15	30.6
R1234yf	33.8	94.7	-53.15	17.6
R717(Ammonia)	113.3	132.25	-77.66	3.5
R774 (CO_2)	73.8	31.1	-56.56	97.6

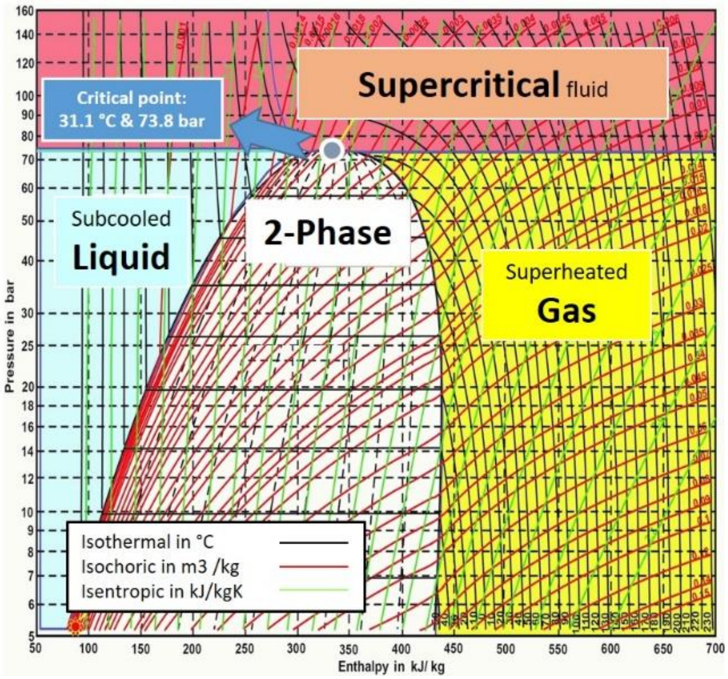

Figure 2-1. CO_2 pressure enthalpy diagram

Figure 2-2 shows the p-T or phase diagram of CO_2. The triple point temperature of CO_2 is -57 °C, below which solid CO_2 will be formed.

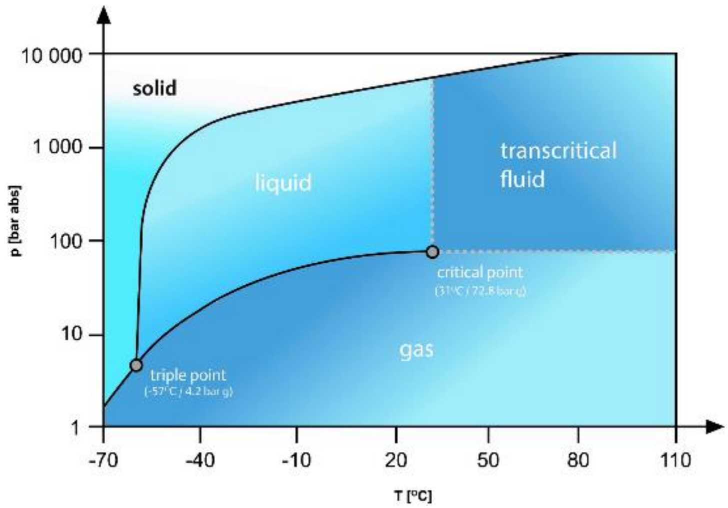

Figure 2-2. CO_2 p-T or phase diagram

CO_2 has relatively higher vapor pressure than other common refrigerants as shown in Figure 2-3. At 20 °C, CO_2 and R134a saturation pressure are 57.3 bar and 5.71 bar, respectively, forming a ratio of ~10. While at -40 °C, this ratio increases to 20. As a clear consequence of the high vapor pressure, CO_2 vapor density is higher compared to other refrigerants at the same temperature as shown in Figure 2-4.

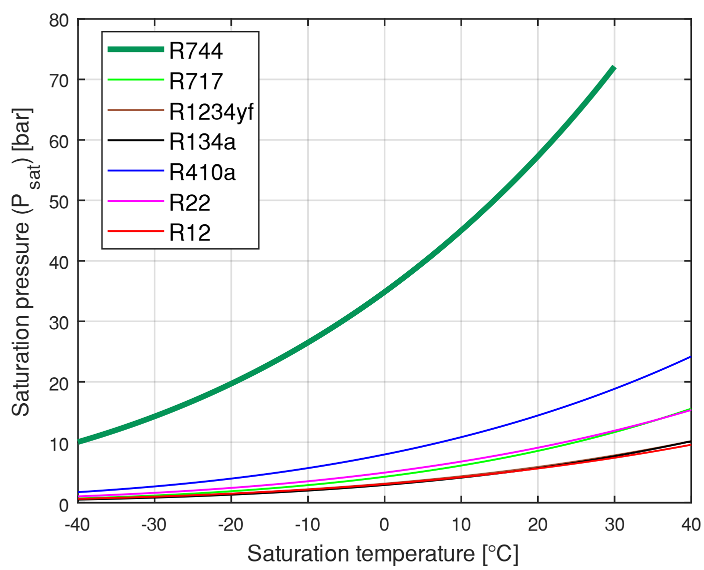

Figure 2-3. Saturation pressure of R744 compared to selected refrigerants

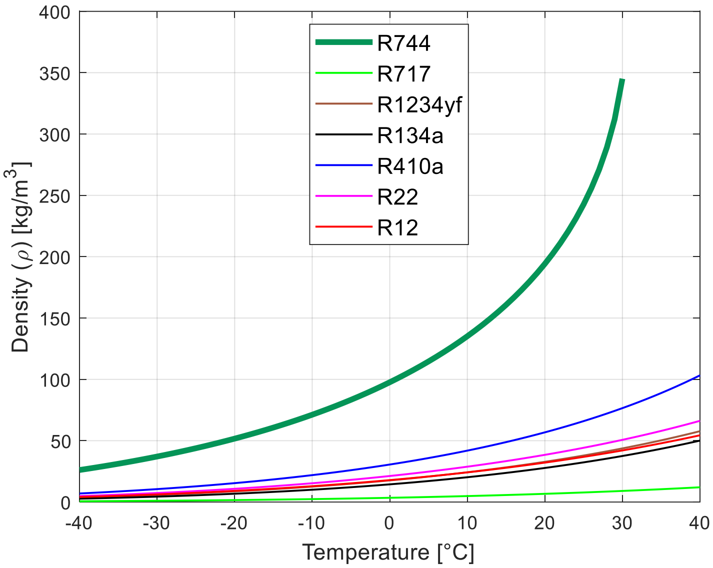

Figure 2-4. Vapor density of R744 compared to selected refrigerants

The heat of vaporization of CO_2 is in the same range of other refrigerants except for Ammonia (R717), which has relatively higher values as shown in Figure 2-5. The volumetric refrigeration capacity is the product of the vapor density and the heat of vaporization. Figure 2-6 shows the volumetric refrigeration capacity for CO_2 and other selected refrigerants. Clearly, CO_2 has a higher refrigeration capacity than the other refrigerants. For instance, at 20 °C, the ratio of the refrigeration capacity of CO_2 to R134a is 5.8. While at -40 °C, this ratio increases to 13.5. Higher volumetric refrigeration capacity means that a volume of CO_2 can absorb more heat than same volume of R134a. This implies that less CO_2 volume flow rate is required to obtain the same cooling effect [12]. The higher the volumetric refrigeration capacity, the smaller compressor displacement. This enables CO_2 systems to have smaller and more compact compressors, which makes CO_2 systems suitable for mobile air conditioning systems where reducing the component space size is desirable.

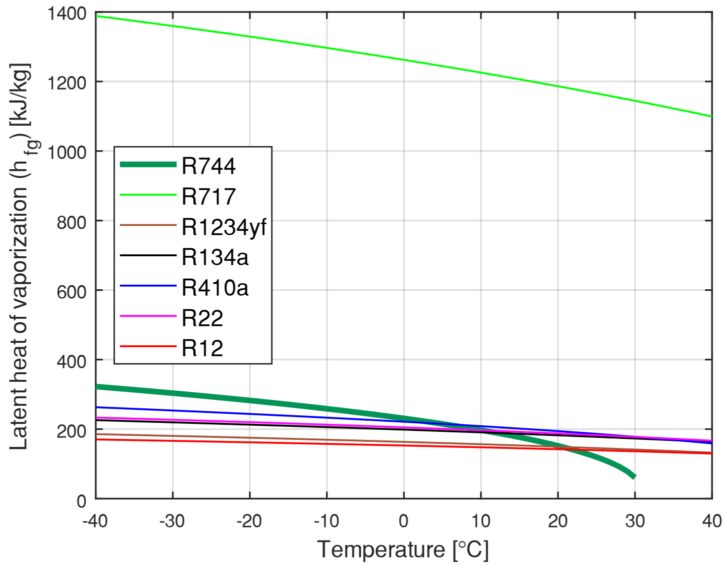

Figure 2-5. Latent heat of vaporization of R744 compared to selected refrigerant

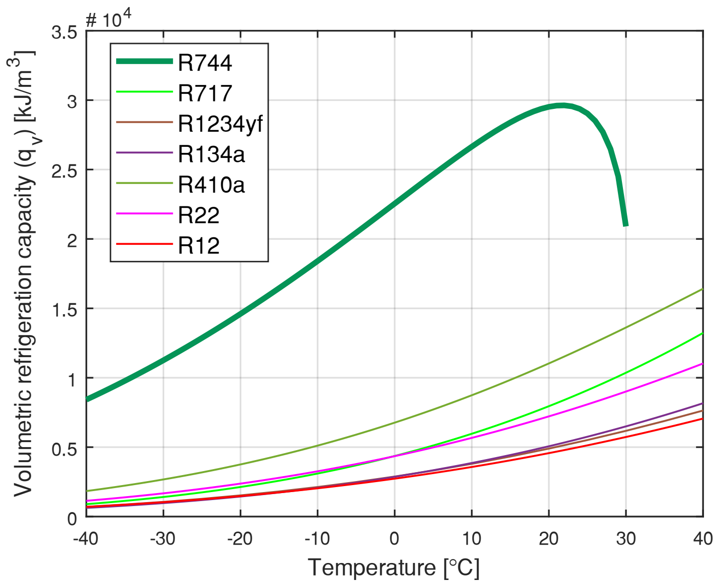

Figure 2-6. Refrigeration capacity of R744 compared to selected refrigerants

Thermal conductivity as a transport property is an important parameter for heat transfer coefficient computation in both single-phase and two-phase flow [3]. Figure 2-7 and Figure 2-8 show the thermal conductivity of CO_2 and selected refrigerants for vapor and liquid respectively. The thermal conductivities of saturated CO_2 vapor at 20 °C is 2.5 times higher than that of R134a vapor, while thermal conductivities are similar for saturated liquids at 20 °C.

In conclusion, CO_2 is a natural environmentally friendly strong alternative refrigerant for HFCs. CO_2 has various attractive properties, which make it a strong candidate to replace R134a. CO_2 is currently used in vending machines and supermarkets where the cycle operates subcritically as the conventional heat pump cycle. The transcritical cycle is under focus by the academic community to further optimize the cycle COP under steady-state and transient operating conditions.

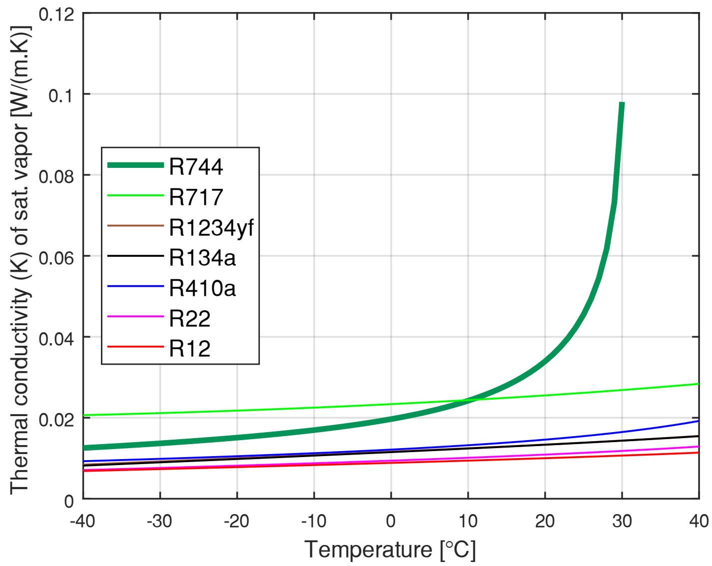

Figure 2-7. Vapor thermal conductivity of R744 compared to selected refrigerants

2.3 Transcritical Cycle

For vapor compression cycles operating at ambient temperature above 31.1 °C, the cycle operates in the supercritical region with high-side pressure above the critical point and operates in the subcritical region with low-side pressure below the critical point. This transitioning from the subcritical to the supercritical gives the cycle its name "transcritical". Since there is no phase change in the supercritical area, the heat exchanger that would ordinarily condense the refrigerant leaving the compressor is instead referred to as a "gas cooler" or GC. This follows the convention of referring to a supercritical fluid as a gas, recognizing that this is something of a misnomer. Since no latent heat effects (phase change) can take place above the critical point, the gas cooler exchange heat by decreasing the gas temperature and increasing its density.

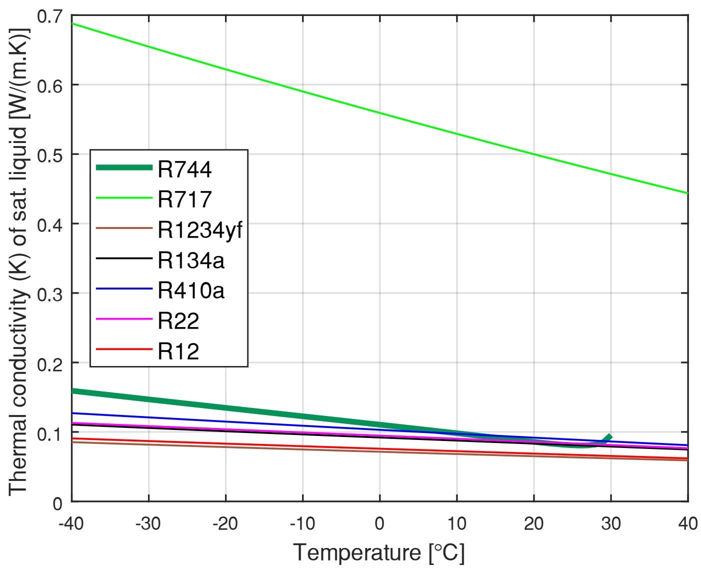

Figure 2-8. Liquid thermal conductivity of R744 compared to selected refrigerants

While in the subcritical two-phase region, pressure and temperature are coupled by the saturation curve, or in other words, the condenser pressure is governed by the condenser temperature; in the supercritical region, pressure and temperature are independent of each other. Therefore, for a given ambient temperature that can be related to the GC outlet temperature [14], the GC pressure (high-side pressure) can be controlled independently. The regulation of the high-side pressure affects the cycle COP [10].

To further illustrate how the change of the GC pressure affects the COP, Figure 2-9 shows four cycles on the p-h diagram that operate at the same evaporation temperature. The first one is a subcritical cycle shown in blue, where the high-side pressure is governed by the condensation temperature. For the three other transcritical cycles, the GC outlet temperature is the same for all of them, but they operate with different GC pressures. The first transcritical cycle shown in gray operates with a GC pressure of 78.0 bar and has a COP of 1.5. By increasing the GC pressure to

86.0 bar, the specific work of compression increases; but the increase in the cooling capacity is larger, hence the COP increases to 3.4 and this cycle shown in green represents the optimum COP cycle. By increasing the GC pressure to 120 bar, the increase of the specific work of compression is larger than the increase of the cooling capacity; hence, COP decreases to 2.0 for the second cycle shown in gray. The isothermal line in the supercritical region has S shape (like the shown T_3 = 35 °C), which implies that for a given GC outlet temperature, as the high-side pressure is increased, the COP reaches a maximum above, which the added capacity no longer fully compensates for the additional work of compression [3]. Therefore, for each GC outlet temperature, there is an optimum GC pressure that can be optimized to find the maximum COP.

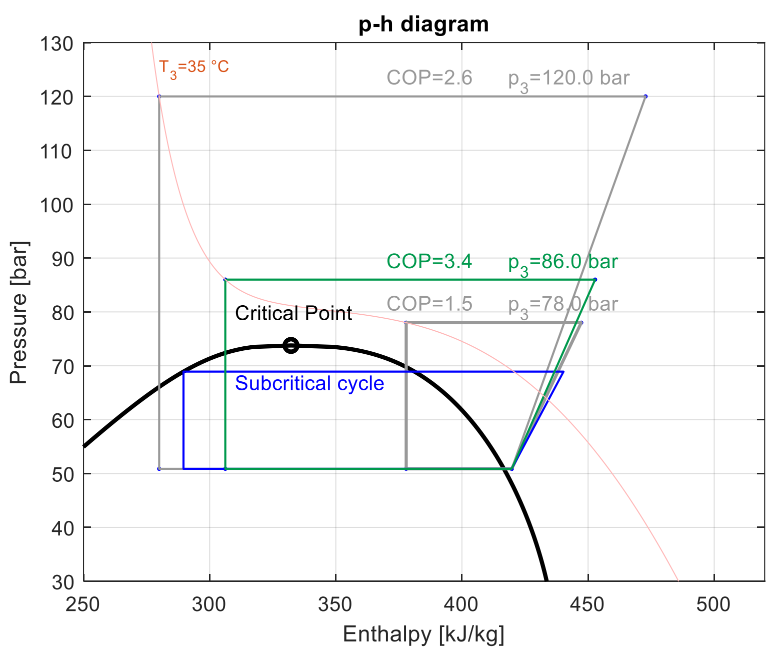

Figure 2-9. p-h diagram for a subcritical and transcritical cycles

2.4 Related Studies

Several contributions to the CO_2 transcritical cycle analysis and understanding were carried out in [3], [11], [15], and [16]. Many of these studies involved an internal heat exchanger that exchanges heat from the section of the line between the GC and the expansion valve with the section of the line between the evaporator/accumulator and the compressor. For that reason, it is usually called a liquid-line/suction-line or just as we will refer to it here by IHX. Also, several control correlations will be reported from the literature. In all these correlations that will be presented, the pressure and temperature units are in bar and °C respectively.

Inokuty [17] deduced a graphical method to determine the optimum high-side pressure of the transcritical cycle. The drawback of this method is that if operating conditions change, the method must be revisited to obtain a new optimal pressure value. It was not then until 1990, when Kauf [14] assessed the graphical method developed by Inokuty [17]. He reported that "the graphical method is too time consuming and not very accurate". He was the first one to develop a control function or offline correlation that relates the optimum GC pressure to the ambient temperature. Kauf [14] reported the difference between the ambient temperature and the GC outlet temperature to be known as the approach temperature. It is written as

$$\mathrm{T_{GCo}} = \mathrm{T_{amb}} + 2.9 \tag{2.1}$$

His developed control function can be written as a function of the ambient or the GC outlet temperature

$$\mathrm{p_{GC,opt}} = 2.6\ \mathrm{T_{amb}} = 2.6\ \mathrm{T_{GCo}} - 7.54 \tag{2.2}$$

where 35 °C ≤ $\mathrm{T_{amb}}$ ≤ 55 °C, and consequently 37.9 °C ≤ $\mathrm{T_{GCo}}$ ≤ 52.9 °C. Therefore, 91 bar ≤ $\mathrm{p_{GC,opt}}$ ≤ 130 bar. It shall be noted, that the original paper has a sign mistake that was corrected in the equation above, thanks to Yang, et al. [18]. The maximum deviation of COP was below 5.8% due to the estimation of the control function. Kauf [14] also reported that the maximum COP for a certain ambient temperature is independent of the compressor speed/frequency.

Boewe et al. [19] conducted a comparative experimental study and performance investigation of CO_2 and R134a refrigeration systems. The R134a system was represented by the Ford Escort mobile air conditioning system with the addition of an IHX. Their results showed that the CO_2 system has a much higher capacity and COP at lower ambient temperatures but slightly lower capacity and COP (a few percent) at very high ambient temperatures (above 45 °C). The IHX was found to improve efficiency by up to 25%. This was especially present at high ambient temperatures while idling (low compressor speed).

Liao at al. [20] studied the transcritical air conditioning cycle that involves an IHX. It was shown mathematically that the optimal GC pressure is dependent on the refrigerant GC outlet temperature, the evaporation temperature, the compressor performance (the isentropic efficiency), and the amount of superheat at the compressor inlet. The effect of each parameter on the COP was studied; and the influence of superheat was found to be weak and, hence, was neglected. Two correlations for the optimal GC pressure were developed. The first one relates the optimal GC pressure to the GC outlet temperature, the evaporation temperature, and the compressor performance as

$$p_{GC,opt} = \frac{2.7572 + 0.1304T_{Evp} - 3.072\alpha/\beta}{1 + 0.0538T_{Evp} + 0.1606\alpha/\beta} T_{GCo} - \frac{8.7946 + 0.02605T_{Evp} - 105.48\alpha/\beta}{1 + 0.0156T_{Evp} + 0.2212\alpha/\beta} \quad (2.3)$$

The second correlation is simplified to neglect the compressor performance effect

$$p_{GC,opt} = (2.778 - 0.0157T_{Evp})T_{GCo} + (0.381T_{Evp} - 9.34) \quad (2.4)$$

In both correlations, -10 °C $\leq T_{Evp} \leq$ 20 °C, 30 °C $\leq T_{GCo} \leq$ 60 °C, and $0 \leq \alpha/\beta \leq 0.3$, therefore, 71 bar $\leq p_{GC,opt} \leq$ 120 bar.

Yoshioka and Miura [21] performed an experiment on the transcritical CO_2 heat pump cycle with an IHX. Their study revealed that a COP equivalent to or higher than that of R134a can be achieved by controlling the GC pressure against the ambient temperature.

Brown et al. [22] theoretically compared a CO_2 and an R134a automotive air conditioning cycle. Both cycles were similar except that the CO_2 cycle incorporated an IHX. It was found that the CO_2

cycle had a lower COP, and the disparity between the COP of the R134a and CO_2 cycles gets larger at higher compressor speed or higher ambient temperatures. Entropy studies showed that CO_2 had better performance in the evaporator, but the GC had poorer performance than the R134a condenser. The large CO_2 temperature glide or change in the GC is the main reason for the high entropy generation and, hence, lowers its performance.

Casson et al. [23] simulated different expansion systems for a CO_2 refrigeration transcritical cycle. The paper introduced and explained a patented cycle design that uses two expansion devices and a liquid receiver in between. The valve after the GC is a differential one that controls the high-pressure side, and the one after the liquid receiver is a thermostatic valve that controls the amount of superheat leaving the evaporator. The liquid receiver ensures saturation conditions at the thermostatic expansion valve entrance. The amount of refrigerant inside the liquid receiver varies as a response to different operating conditions of the circuit. The simulation revealed that:

- COP decreases with the increase of water inlet temperature of the GC.
- The optimal GC pressure increases with the increase of the inlet water temperature of the GC. The same behavior occurs for the upper pressure of the differential valve at fixed ΔP.
- The thermostatic expansion valve can operate only with water temperatures lower or equal to 25 °C (subcritical cycle), and in this case provides better COP than the using two valves; however, it requires a larger flow rate (five times the flow rate in the case of the transcritical cycle.)

Sarkar et al. [24] modeled and conducted an exergy analysis for the transcritical CO_2 heat pump cycle with an IHX for simultaneous cooling and heating applications. Based on the cycle analysis, the paper developed a control correlation in terms of the GC outlet temperature and evaporation temperature. The authors concluded that to increase the COP, the system must operate at the lowest possible GC outlet temperature and highest possible evaporation temperature. The exergy loss through the expansion device was estimated as 18%, which was the highest component loss. The loss is relatively large due to the pressure difference between the high-side and low-side, and also due to the fact that near the critical point the entropy as well as other properties change rapidly, as pressure drops from supercritical to subcritical. The developed control correlation is valid for -10 °C ≤ T_{Evp} ≤ 20 °C and 30 °C ≤ T_{GCo} ≤ 60 °C, and is obtained as

$$p_{GC,opt} = 4.9 + 2.256T_{GCo} - 0.17T_{Evp} + 0.0023T_{GCo}^2 \tag{2.5}$$

Chen and Gu [25] studied and modeled the transcritical CO_2 refrigeration cycle. The authors evaluated the effect of several parameters related to the IHX on the cycle performance. A control correlation is developed for the optimum high pressure where its coefficients are close to the one developed by Kauf [14]. Considering a 2.9 °C approach temperature, the correlation is proposed as

$$p_{GC,opt} = 2.68T_{GCo} - 6.797 \tag{2.6}$$

Liu et al. [26] performed an experiment on a prototype automotive CO_2 air conditioner system with an IHX. Their major findings have been:

- The reported COP was similar for both oil types: ISO VG 56 PAG and ISO VG 68 POE, although the cooling capacity and the compressor work of POE system was higher,
- The COP has a maximum value at a specific CO_2 charge; undercharged CO_2 systems could result in a fast decrease of the cooling capacity and the COP. However, overcharged CO_2 systems could cause an abrupt increase of the compressor consumed work.
- The air flow rate is recommended to be high in the evaporator and the GC to increase the COP of the system.

- The system needs a high-side pressure controller to prevent a decrease in the efficiency with the increase in the evaporator pressure.

Yang et al. [27] performed a simulation of a CO_2 transcritical heat pump cycle with an IHX. It was found that the COP of the system is heavily affected by the GC pressure, which in turn influenced by the GC outlet temperature and to a lesser extent by the ambient temperature. The influence of the GC outlet temperature and the ambient temperature weakens as the compressor speed increases. Several correlations were developed that relate the optimum GC pressure with the GC outlet temperature and the GC outlet temperature with the ambient temperature. The correlations are developed at speeds of 950, 1800, and 3000 rpm.

Tamura et al. [28] carried out a theoretical study on a CO_2 transcritical automobile AC system, replacing the auxiliary electric heater (used with high efficiency automobiles where the engine heat release is low) with a heating method utilizing the heat released during dehumidification. The heat released from the refrigerant in the high-side pressure during dehumidification is transferred to the engine coolant through a water refrigerant heat exchanger. Thus, the air is warmed using the heated engine coolant. Using this method, the cycle total work input decreased by 20% compared to R134a system for a medium sized automobile. Another finding is that the optimum amount of refrigerant in the heating/dehumidification mode is larger than the optimum amount in the cooling mode due to the fact that the outdoor temperature is generally less in case of the heating mode compared to the cooling mode; thus, the amount of refrigerant held in the outdoor heat exchanger during the heating operation is greater than the amount during the cooling operation. The paper deduced a control method using two expansion devices to adjust the refrigerant optimum charge for cooling and heating/dehumidification modes.

Cho et al. [29] analyzed experimentally the cooling performance of a variable speed CO_2 transcritical cycle equipped with a scroll compressor. Parameters considered are the refrigerant charge, compressor frequency, EXV opening, and the length of the IHX. The optimum charge was determined by varying the charge from 1.1 to 1.5 kg and measuring the COP. The compressor frequency was swept from 30 to 60 Hz in an increment of 10 Hz. The EXV opening was varied from 35 to 56% in an increment of 7%. The IHX length was varied from 2 to 3 m. It was found that:

- Increasing the compressor frequency decreases the cooling COP because the increase of compressor power consumption was significant while the increase of mass flow rate was relatively small at high frequencies.
- The system showed maximum COP at a specific system charge at all compressor frequencies. Therefore, the optimum refrigerant charge determined at the rated compressor frequency can be applied at all compressor frequencies.
- The optimum EXV opening determined at the maximum COP at a given compressor frequency increases by increasing the frequency.
- Simultaneous control of the EXV opening and the compressor frequency allow the optimal control of the GC pressure.
- The presence of an IHX increased the compressor power consumption by 0.8 to 2.5% and increased the cooling capacity by 6.2 to 11.9%; hence, COP increased by 7.1 to 9.1%. The COP remained nearly constant by increasing the length of the IHX beyond 2 m.

Cabello et al. [30] carried out an experiment on a CO_2 transcritical refrigeration cycle that has two expansion stages with a liquid receiver in between. The first expansion device is a back-pressure valve to control the GC pressure, while the second expansion device is an EXV to control the amount of superheat at the evaporator outlet. The article looked at how the cooling capacity, compressor power input, and refrigerant mass flow rate change as a function of the GC pressure in the range from 89 to 105 bar. The optimal GC pressure determined experimentally was compared to commonly used correlations in the literature namely, Kauf [14], Liao et al. [20], Sarkar et al. [24], and Chen and Gu [31]. A maximum deviation of 15.7%, 4.6%, 1.5%, and 7.5% is reported respectively. Thus, the correlation of Sarkar et al. [24] has the smallest deviation from the experimental results. It was also concluded that a small error in the estimation in the GC pressure is more sensitive close to the critical point, meaning that it causes a bigger reduction in the COP. Also, the COP reduction is less if the GC pressure is overestimated rather than underestimated.

Kim et al. [32] performed an experiment on a CO_2 transcritical air conditioning system with an IHX. The study found that increasing the compressor speed increases the cooling capacity but reduces the COP. By numbers, at idle conditions (compressor speed of 900 rpm), the COP was 2.7; while at driving conditions (compressor speed of 1800 rpm), the COP was reduced to 1.9. The paper also proposed a control function for the optimum GC pressure to achieve maximum COP, the equation is obtained as

$$\mathrm{p_{GC,opt}} = 1.938\mathrm{T_{GCo}} + 9.872 \tag{2.7}$$

Xiaowei et al. [33] conducted an experiment on a transcritical CO_2 heat pump water heater with an IHX and two manual expansion devices with a liquid receiver in between. The GC pressure was found to be mostly dependent on the GC outlet temperature and the evaporation temperature. The GC pressure is regulated by adjusting the first-stage manual valve. The smaller the opening of the valve causes a higher GC pressure. The study reported that the GC pressure could not be decreased any more when the first-stage valve was at the maximum opening. Thus, the pressure is not optimized at some operating conditions. It was also found that the superheat at the inlet of the compressor had little effect on the optimum heat rejection pressure.

Cecchinato et al. [34] analyzed the CO_2 transcritical refrigeration cycle. The study concludes that the control correlations obtained from the GC outlet temperature, being taken as the independent variable, behaved better than correlations with the secondary fluid inlet temperature as independent variable.

Zhang et al. [35] performed simulations and experimental testing on a transcritical CO_2 heat pump system with two expansion devices and an IHX. It was found that the optimal GC pressure mainly depends on the GC refrigerant outlet temperature, the evaporation temperature, and the performance of the compressor. The effect of superheat was found to be weak. The two-stage expansion configuration enabled the control of the high pressure and evaporating pressure, however, the manual regulation of GC pressure exhibits some unsteadiness, especially for higher pressure, as the study reported. The correlation developed by Liao et al. [20] was corrected based on the experimental results as

$$p_{GC,opt} = \frac{2.7572 + 0.1304T_{Evp} - 3.072\alpha/\beta}{1 + 0.0538T_{Evp}} T_{GCo} - \frac{8.7946 + 0.02605T_{Evp} - 105.48\alpha/\beta}{1 + 0.0516T_{Evp} + 0.2212\alpha/\beta} - 0.1801 + 0.00473T_{GCo} \tag{2.8}$$

Zhang and Zhang [36] introduced an online correlation-free or real time control method for the basic CO_2 transcritical heat pump cycle. They simulated their work to test the algorithm, but no experimental work was reported. The optimized GC pressure formula is obtained using the steepest descent method to track the optimal pressure set point. The formula is written in terms of the GC pressure from current and previous iterations, cooling capacity, and compressor power consumption per unit mass flow. Therefore, measurements of the compressor suction and discharge temperatures, GC pressure, and outlet temperature are needed for the optimization formula. The authors used previously numerical models for the heat exchangers [37]. The study showed few simulation test cases that evaluated the optimization technique performance. In one of their test cases, the algorithm adjusted the GC pressure from an initial pressure of 85 bar close to the optimal value of 100 bar, taking around ≈ 17 min. In another case, where the compressor speed changed during operation from 70 to 60 Hz, it took the algorithm around 30 min to adjust the GC pressure from 100 bar initially close to the optimal value of 104 bar. It can be noted that the time needed to optimize the COP is relatively long.

Cecchinato et al. [38] proposed a real-time algorithm based on a neural network technique to determine the optimal GC pressure for a CO_2 heat pump water heater system with an IHX. The algorithm was tested statically and dynamically. In static tests, the algorithm was trained by 240 simulation test results. This resulted in a maximum pressure deviation of ≈-1.5 bar and COP deviations ranging from 0% to 1.5%. In dynamic testing, the operation of heat pump system was simulated over two years. The average pressure deviation was ≈0.9 bar. It took the system a few days for the training to adjust the optimal high pressure. Although the algorithm provides acceptable optimal pressure and COP deviations, it requires either large number of simulation data for training the algorithm or consistent observation to train the algorithm, which took few days in their dynamic testing.

Qi et al. [39] experimentally studied the transcritical CO_2 heat pump water heater. The GC is cooled by water while the evaporator is cooled by air. It was found that the optimal GC pressure was largely dependent on the refrigerant GC outlet temperature. The effect of the evaporation temperature, which is dependent on the ambient temperatures, was found to be weak on the optimal GC pressure. The COP for the optimal GC pressure decreases substantially as the refrigerant GC outlet temperature increases in the temperature range from 25 °C to 45 °C. A correlation of the optimal GC pressure is obtained, which was found to be in a good agreement with the correlation of Chen and Gu [25]. The developed correlation is valid for 25 °C ≤ T_{GCo} ≤ 45 °C and is proposed as

$$p_{GC,opt} = 132.3 - 8.4T_{GCo} + 0.3T_{GCo}^2 - 27.7 * 10^{-4}T_{GCo}^3 \tag{2.9}$$

Boccardi et al. [40] performed experiments on a CO_2 transcritical heat pump plant with two hermetic single stage reciprocating compressors and an IHX, for light commercial applications. It was found that both the CO_2 mass flow rate and the compressor absorbed power increase as the evaporation pressure increases. At a certain evaporation pressure, increasing the GC pressure reduces the mass flow rate, mainly due to the corresponding reduction of the volumetric efficiency, while the compressor power increases because of both the increase of discharge enthalpy and the decrease of compressor efficiency. The study showed that higher values of the GC pressure correspond to higher evaporator inlet enthalpies, which leads to reducing the cooling capacity.

Baek et al. [41] conducted an experiment on a CO_2 heat pump basic cycle. The study normalized the system charge using the equation

$$m_{normalized} = \frac{m_{actual} - m_{vapor}}{m_{liquid} - m_{vapor}} \tag{2.10}$$

where m_{liquid} and m_{vapor} are calculated by multiplying the system total volume by the densities of the saturated liquid and vapor at a room temperature of 25 °C. Therefore, if the system is charged with liquid refrigerant, then $m_{normalized}$=1, and if the system is charged with vapor refrigerant, then $m_{normalized}$=0. Several conclusions can be made from this paper:

- Increasing the normalized charge results in decreasing the optimum EXV opening; hence, the GC pressure increases by increasing the normalized charge, which therefore increases the enthalpy difference across the GC.

- The cooling capacity increases with the increase in the normalized charge due to the increase of the enthalpy difference across the GC and the increase of the mass flow rate that increases the heat exchange in the GC.
- The compressor power input increases linearly with the increase in the normalized charge due to the increase in the compression ratio and therefore COP peaks at a specific normalized charge.
- The GC pressure decreases with the increase in the EXV opening due to the decrease in the flow restriction through the EXV, which in turn decreases the compression ratio.
- As the EXV opening increases, the mass flow rate increase; but the enthalpy difference across the GC decreases due to the decrease of the GC pressure.
- Because of the previous point, the cooling capacity reaches its maximum value at a specific EXV opening, due to the trade-off between the increase in the mass flow rate and the decrease in the enthalpy difference across the GC, according to the EXV opening.
- The compressor power input decreases with the increase of the EXV opening due to the decrease in the compression ratio, therefore, the COP is maximized at a specific EXV opening.

Kim et al. [42] utilized a previously proposed real time algorithm by the same authors to search for the optimal GC pressure and applied the algorithm to a transcritical CO_2 refrigeration cycle with an IHX. The algorithm determines the expansion valve percentage opening to obtain the corresponding optimum GC pressure. The algorithm relies on the online measured data of the refrigerant's pressure and temperature at the GC outlet, pressure at compressor suction, and the compressor consumed power. This method calculates a ratio of the expected increment cooling capacity and the compression work with the expansion valve slightly closed. This ratio is compared with the current COP to determine whether the expansion valve needs to be opened or closed. The algorithm has several limitations as reported by the authors. First, the degree of superheat change at the compressor suction can generate a decrement or increment of specific cooling capacity, which is undetectable by the real time controller. Second, the GC heat exchanger size must be sufficiently large for the controller to give acceptable results. Third, any change of the evaporation pressure will not be detected by the algorithm; and as a result, the controller will underestimate the increment of the specific compressor work.

Peñarrocha et al. [43] showed mathematically that maximizing the COP is equivalent to minimizing the compressor power consumed, which avoids the need to use several sensors. The cycle experimented in this work had two stage expansion devices with an accumulator in between. A back-pressure regulator to control the GC pressure and an electronic expansion valve to control the evaporator superheat. The paper utilized a real-time optimization method called "perturb and observe" to minimize the compressor power while measuring the evaporator secondary fluid exit temperature, the GC pressure, and the compressor consumed power. Based on these measurement signals, the controller decides the compressor speed and the position of a stepper motor that modifies the opening degree of the back-pressure valve, which are the controllable parameters. A drawback of this method is that the achievement of the optimum operating point is delayed if the environmental temperature has fast and long variations. In that case, the controller will evolve in the wrong direction during the transient time until the algorithm achieves the boundary of the max/min allowed pressure and then changes the direction towards the optimum value. The results of this work yielded the decrease of the compressor consumed power; and, hence, the increase of the COP, however, the time the algorithm takes to reach to the optimum is long. For example, the COP took two hours to increase from 1.47 1.6, and it took 12 hours to increase from 1.47 to 1.75.

Hu et al. [44] applied and simulated an optimization strategy called "Extremum seeking control (ESC)" on a CO_2 transcritical heat pump water heater system with an IHX. The optimization strategy can search for the optimal input in real time without need for a system model. The control input parameter is the GC pressure, while COP is also fed back to the controller. A high-level controller based on the ESC optimization finds the opium GC pressure. Then it communicates to a low-level controller that involves an inner PI control loop to adjust the EXV opening to achieve the desired GC pressure. The simulation results showed that for fixed operating conditions where the hot water outlet temperature and the evaporation temperature are constant, the GC pressure is adjusted from an initial value of 80 to 83.8 bar to reach the optimum COP within 2% settling time in about 33 min. This time increased to around 93 min when the initial pressure changed to 92 bar. The authors explained that this is due to the process nonlinearity. To reflect varying operating conditions, a step input was applied on the water outlet temperature from 60 °C to 70 °C. The algorithm took around 83 min to reach the new optimum COP. The algorithm used has a major advantage that it is model free algorithm, although it lacks the speed of the convergence to the optimum COP value.

Hazarika et al. [45] simulated a CO_2-based air conditioning system with two expansion valves. Fin and tube heat exchangers are modeled based on a discretized approach. It was found that increasing the GC air inlet temperature reduces COP while increasing the evaporator air inlet temperature increases the COP.

Yang et al. [46] simulated the transcritical CO_2 refrigeration cycle with an expander and compared its performance to a throttle valve cycle. The authors referred to another study that replaced the throttling valve by an expansion turbine and could reduce the total irreversibility by 35% and increase the system COP by 25%. The optimal GC pressure was found to be strongly affected by the GC outlet temperature and to less extent by the evaporation temperature, as in cycles that use throttling valves. By increasing either compressor or expander efficiency, the GC pressure increases. Control correlations have been developed for the optimal GC pressure in terms of GC outlet temperature and evaporation temperature. The reported linear version of the correlation is

$$\mathrm{p_{GC,opt}} = 0.01674\mathrm{T_{Evp}} - 0.3317 + (0.2525 - 0.0007\mathrm{T_{Evp}})\mathrm{T_{GCo}} \tag{2.11}$$

[47] theoretically compared various modifications of transcritical CO_2 heat pump systems. The relevant paper conclusions are:

- Systems with an IHX have COP relatively better than the basic cycle at higher ambient temperature.
- Systems with an IHX have a lower mass flow rate at higher ambient temperature allowing for operation with lower GC pressure.
- COP of systems with work recovery (expanders) is comparatively high due to work recovered.
- Multi-stage systems are found to have similar performance as the basic system for applications like refrigeration.

2.5 Summary and Thesis Contributions

Summarizing the above, researchers have been focusing on understanding the effects of the system parameters such as the refrigerant GC outlet temperature, the evaporation temperature, the compressor efficiency, the system charge and other parameters on the COP, the cooling/heating capacity, and the compressor power for the system the considered/built. Many control correlations have been developed for the GC pressure to maximize the COP either through simulations or experiments. These correlations are developed as a function of the GC outlet temperature such as [14], [25], [32], and [39]; and in a few cases as a function of both the GC outlet temperature and evaporation temperature such as [24] and [20] where the last one includes a term for the compressor isentropic efficiency as well. The evaporation temperature has less effect on the COP compared to the GC outlet temperature, while the compressor performance depends on the selected compressor isentropic efficiency. Each of these correlations is ideally valid for the system it was simulated or experimented with including the compressor efficiency correlations and the specific parameters ranges.

On the other hand, few real time algorithms such as [36], [38], [42], and [44] have been recently developed to maximize the COP online. This requires continuous pressure and temperature measurements at different locations. As highlighted in the previous subsection, in some of these methods the convergence time to the optimum value is relatively long. The improvement of these approaches is still in progress especially for transient operation. In addition, not all these developed methods have been verified experimentally. Therefore, the developed offline control correlations are still a good guide for the system to maximize the COP, even if they may have some deviations due to their reliance on the system model.

To the best of our knowledge, all the developed correlations in the literature focus on optimizing the COP. However, this does not mean that the system is working at its highest cooling/heating capacity that may be desired for example in a transient start-up operation or based on the passenger preference to maximize the thermal comfort (i.e. reaching the set point quicker) to cool down or heat up a space as quickly as possible to a certain condition. For that purpose, a multi-objective optimization study will be conducted to better understand the trade-off between COP and cooling capacity; and based on that, a control and optimization strategy will be developed that can alter the system operation to work on its optimum COP, optimum cooling/heating capacity, or a tradeoff point as desired. Since the commercial compressor we are using in our experimental apparatus has no available efficiency correlations either from the manufacturer or the literature, we will model the compressor by developing the isentropic and volumetric efficiency correlations for this compressor. The developed efficiency correlations are compared to several ones available in the literature. In addition, and to facilitate the multi-objective study and optimization strategy, the CO_2 transcritical cycle performance is modeled in a MATLAB environment and analyzed to investigate the effect of the GC outlet temperature, the evaporation temperature, and the superheat on the COP for the system considered in the experimentation. Furthermore, since the offline correlations depend mainly on the type of the compressor and the system under investigation, an optimized control correlation is generated and compared to the common ones in the literature, which relates the optimized GC pressure to the GC outlet temperature. The correlation can be used to maximize the COP in the specified range of operating conditions for the considered system.

For further experimental investigations of the system, a CO_2 air conditioning system and its coolant system have been constructed at the MSU Turbomachinery Lab that support cooling, heating, and dehumidification modes. Several system parameters' effects on the cooling and heating COP will be analyzed and reported.

The thesis contributions can be summarized as follows:

- Developing the transcritical thermodynamic model, the compressor efficiency correlations, and an offline control correlation for our experimental system.
- Understanding the tradeoff between the COP and cooling/heating capacity and how the Pareto Fronts are affected by the GC outlet temperature, evaporation temperature, superheat, compressor speed, and compressor performance.

- Development of a bi-objective optimization and control strategy to either operate at the optimum COP, the optimum cooling/heating capacity, or a tradeoff point based on a predefined preference
- Proposing a hybrid offline and online control methodology for optimizing the system COP and/or the cooling/heating capacity. The hybrid approach reduces the time to approach the desired optimum solution compared to online methods only.
- Designing, building, testing, and validating a CO_2 heat pump test rig facility with plate heat exchangers that support cooling, heating, and dehumidification modes
- Experimentally investigating several system parameters' effects on the cooling and heating COP for the CO_2 transcritical system.

Chapter 3: Thermodynamic Modeling and Analysis

This chapter presents the thermodynamic modeling of the CO_2 transcritical cycle and analyzes its performance. The basic CO_2 transcritical cycle schematic that consists of a compressor, GC, expansion device, and an evaporator is shown in Figure 3-1 along with the p-h and T-s diagrams. The assumptions considered for the cycle simulation and analysis are as follows: the cycle is assumed to operate at steady-state, the compression process is adiabatic but non-isentropic, the heat transfer with the ambient of components other than the heat the exchangers is neglected, the evaporation and the gas cooling processes are isobaric, the pressure drop in heat exchangers and CO_2 tube lines are neglected, and CO_2 is considered as a pure fluid neglecting the effect of the lubricant on the properties.

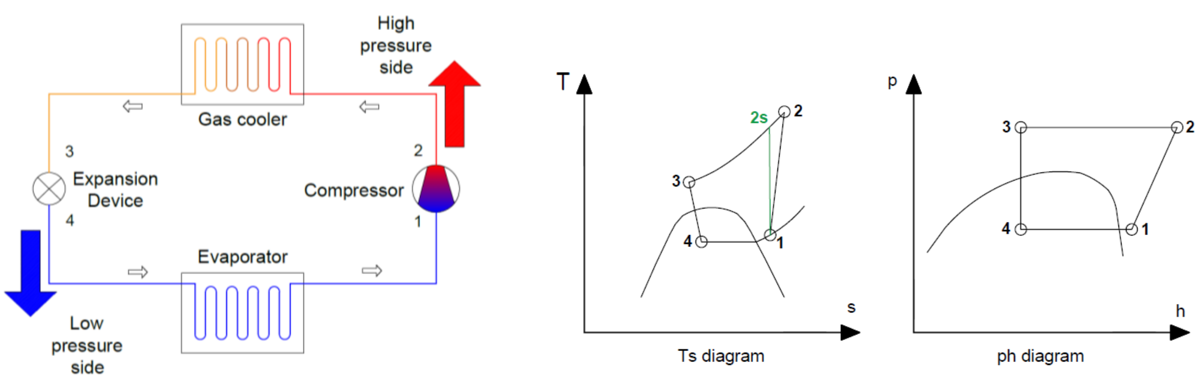

Figure 3-1. Basic CO_2 Transcritical system with the corresponding T-s and p-h diagrams

3.1 Compressor Modeling

The compressor selected for this study is a Dorin CD200 - CD180H, 3-phase, 230 V, and 60 Hz with 1.34 kW rated input power. The compressor supports evaporation temperatures ranging from -30 °C to 15 °C. To simulate the cycle behavior, the compressor efficiency correlations are needed to calculate the compressor discharge enthalpy and the mass flow rate. The compressor isentropic and volumetric efficiency correlations are expressed as [19]

$$\eta_{is} = \frac{\dot{m}_r\,(h_{2s} - h_1)}{\dot{W}_{comp}} \tag{3.1}$$

$$\eta_v = \frac{\dot{m}_r\,v_1}{\omega\,V_d} \tag{3.2}$$

Since there were no available efficiency correlations from the manufacturer, the manufacturer's software was used to simulate the compressor behavior at different operating conditions. The compressor discharge pressure p_2 was swept from 75 to 140 bar at constant GC outlet temperature of 35 °C and a total superheating of 1 K. The superheat can take place either inside the evaporator, which adds to the cooling capacity, and/or it can be generated outside the evaporator, which is usually due to the pressure drop in the connecting lines between the evaporator outlet and the compressor suction and/or external heat transfer to the line. Eqns. (3.1) and (3.2) are used to calculate the isentropic and volumetric efficiency for each data point. A MATLAB code was written to determine the efficiency correlations using regression analysis. For each iteration, the code takes the mass flow rate $\dot{m}$, and the compressor consumed power $\dot{W}_{comp}$ as input from the manufacturer's software and calculates the efficiency. The NIST REFPROP database (Lemmon *et al.*, 2013) is used within the MATLAB code to retrieve the thermodynamic properties of CO_2.

The compressor envelope is shown in Figure 3-2 which shows the compressor's maximum high-side pressure for the evaporation temperature range from -30 °C to 15 °C. This line can be expressed with Eqn. (3.3). This equation is used to ensure that the high-side pressure in each sweep iteration is within the compressor envelope.

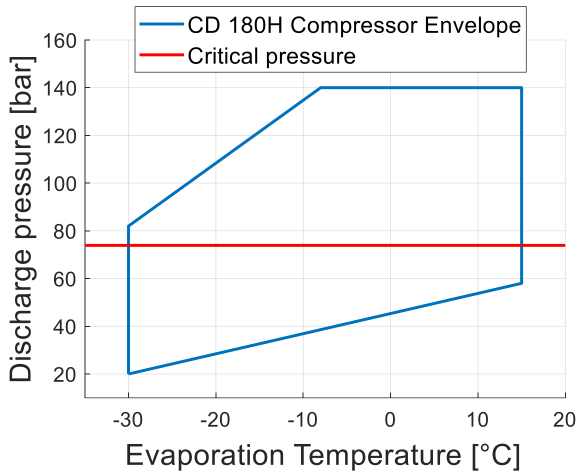

Figure 3-2. Dorin CD200-CD180H Compressor Envelope

$$\text{Discharge pressure } (\mathrm{p}_2) < \begin{cases} 2.63\ \mathrm{T}_1 + 160.9, & -30\ ^\circ\mathrm{C} \leq \mathrm{T}_1 \leq -8\ ^\circ\mathrm{C} \\ 140, & -8\ ^\circ\mathrm{C} < \mathrm{T}_1 \leq 15\ ^\circ\mathrm{C} \end{cases} \tag{3.3}$$

Most of the compressor's efficiency correlations found in the literature were developed at a selected evaporation temperature. For the work discussed here, the efficiency correlations are developed at evaporation temperatures of -8 °C, 0 °C, and 15 °C. Compared to relying on a set of correlations developed at a single evaporation temperature, this was found to provide more accurate results when the correlations are used at different evaporation temperatures in the cycle analysis.

A third-order polynomial fit that takes the form of Eqns. (3.4) and (3.5) has been adapted for the resulting efficiencies as a function of the compressor pressure ratio $r_p = p_2/p_1$. Table 3-1 presents the polynomial coefficients for the different evaporation temperatures. Using the developed correlations, the maximum deviation of the calculated mass flow rate and the compressor power from the manufacturer's software values used in generating the correlations was ±0.34 %. Figure 3-4 shows the developed compressor volumetric and isentropic efficiency correlations represented by Eqns. (4) and (5) along with Table 3-1, compared to CO_2 compressor correlations used in the literature. The correlations of Sarkar *et al.* (2009), Casson *et al.* (2003), Ortiz *et al.* (2003), and

Liao *et al.* (2000) are based on experimental data fitting for a semi-hermetic compressor, while no information was provided for the Robinson and Groll (1998) correlations. It can be noted that the isentropic efficiency varies considerably between different compressors; hence, selecting the right correlations for the selected compressor is important for the cycle accurate simulations.

$$\eta_v = a_0 + a_1 r_p + a_2 r_p^2 + a_3 r_p^3 \quad (3.4)$$

$$\eta_{is} = b_0 + b_1 r_p + b_2 r_p^2 + b_3 r_p^3 \quad (3.5)$$

Table 3-1. Developed volumetric and isentropic efficiency correlations at different evaporation temperatures

	η_v				η_{is}			
T_1(°C)	a_0	a_1	a_2	a_3	b_0	b_1	b_2	b_3
-8	1.0904	-0.1929	0.0189	-0.0003	0.7532	-0.1378	0.0351	-0.0029
0	1.0829	-0.1965	0.0202	-0.0001	0.7191	-0.1358	0.0455	-0.0048
15	1.0380	-0.2044	0.0249	0.0002	0.0561	0.5536	-0.1961	0.0240

3.2 Cycle Modeling

For the basic transcritical cycle shown in Figure 3-1, and considering the compressor isentropic efficiency, the enthalpy at state 2 is calculated by

$$h_2 = h_1 + \frac{h_{2is} - h_1}{\eta_{is}} \quad (3.6)$$

The refrigerant mass flow rate is determined based on the compressor volumetric efficiency

$$\dot{m} = \frac{\eta_v \, \omega \, V_d}{\nu_1} \quad (3.7)$$

The expansion process is considered isenthalpic, hence

$$h_4 = h_3 \quad (3.8)$$

The cooling capacity is

$$\dot{Q}_c = \dot{m}\,(h_1 - h_3) \quad (3.9)$$

The compression power is calculated by

$$\dot{W}_{comp} = \dot{m}\,(h_2 - h_1) \tag{3.10}$$

The cooling coefficient of performance is calculated as

$$COP = \frac{h_1 - h_3}{h_2 - h_1} \tag{3.11}$$

A parametric study is carried out to show the effect of several parameters on the cooling COP. The range of the GC pressure is varied from 75 to 140 bar, the GC outlet pressure from 32 °C to 53 °C, the evaporation temperature from -30 °C to 15 °C, and the superheat from 0.5 K to 15 K.

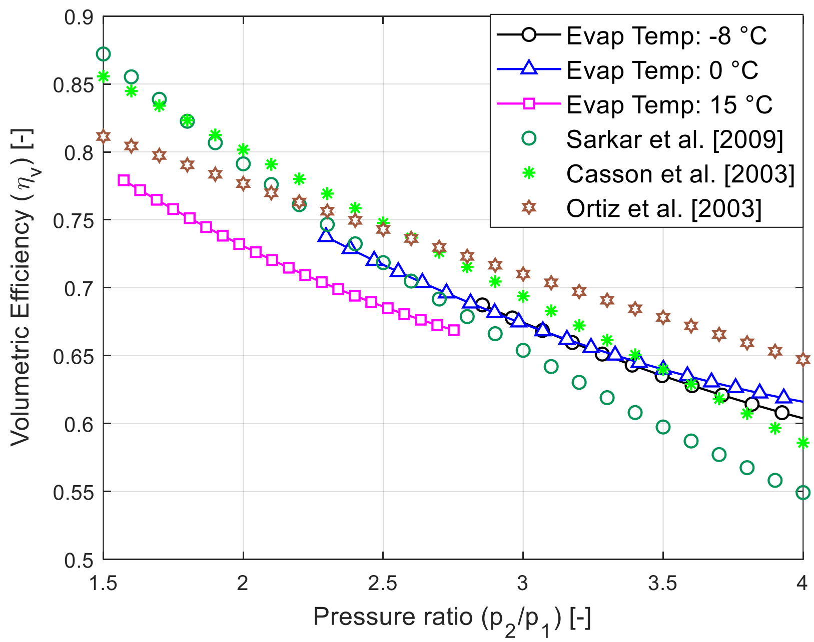

Figure 3-3. Compressor developed volumetric efficiency correlations compared to correlations from the literature

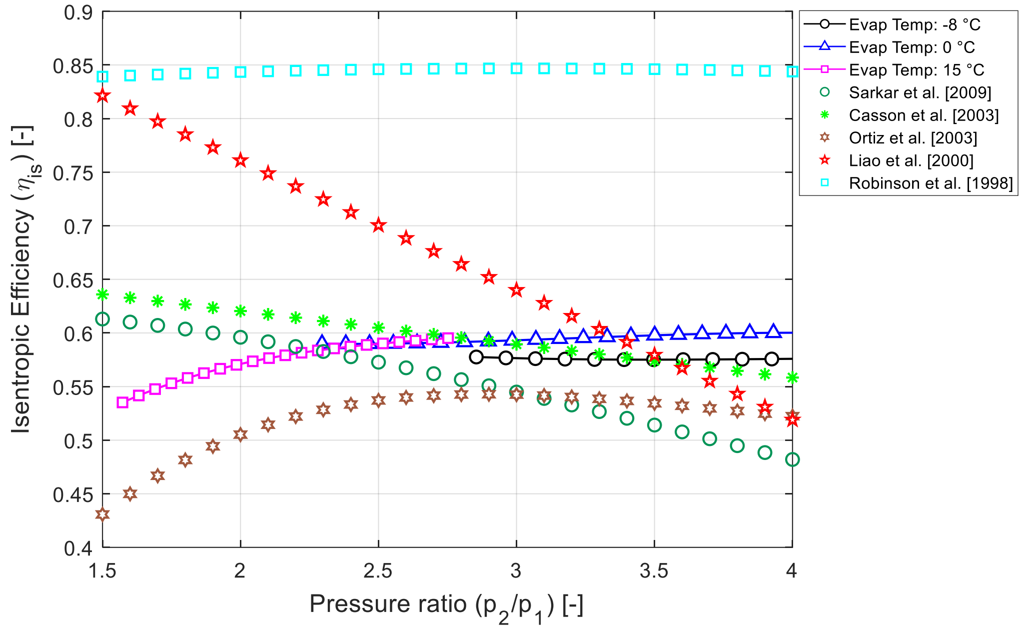

Figure 3-4. Compressor developed isentropic efficiency correlations; compared to correlations from the literature

3.3 Analysis

Figure 3-5 shows the influence of varying GC pressure on the COP at different GC outlet temperatures at 15 °C evaporation temperature and 1K superheat. Clearly, there is an optimum GC pressure for each GC outlet temperature where the COP is maximum. This is shown by the green curve polynomial fit connecting those optimum points. Apparently, and as indicated by Yang et al. [18], the accurate determination of the optimum GC pressure is much more sensitive close to the critical point than at higher pressures. At higher GC pressures, the COP curves are flatter; hence, the maximum COP becomes almost insensitive to the estimate of optimal high pressure.

The effect of changing the GC pressure on the COP at different evaporation temperatures at 35 °C GC outlet temperature is shown in Figure 3-6. The evaporation temperature of -30 °C was excluded from this simulation because of the limited allowed high-side pressure of 82 bar at this evaporation temperature. The green curve connects the optimum pressure points. From the graph, at the two extreme evaporation temperatures, -25 °C and 15 °C, the optimum GC pressure is 90.5 bar and

86.2 bar respectively. In fact, if 86.2 bar pressure is applied as a GC pressure for the whole evaporation temperature range, the resulting COP is no more than 1.5% (at either -15 °C or -25 °C) away from the optimum COP. Hence, the effect of the evaporation temperature on the optimum GC pressure is negligible compared to the more considerable effect that the GC outlet temperature has on the optimum GC pressure.

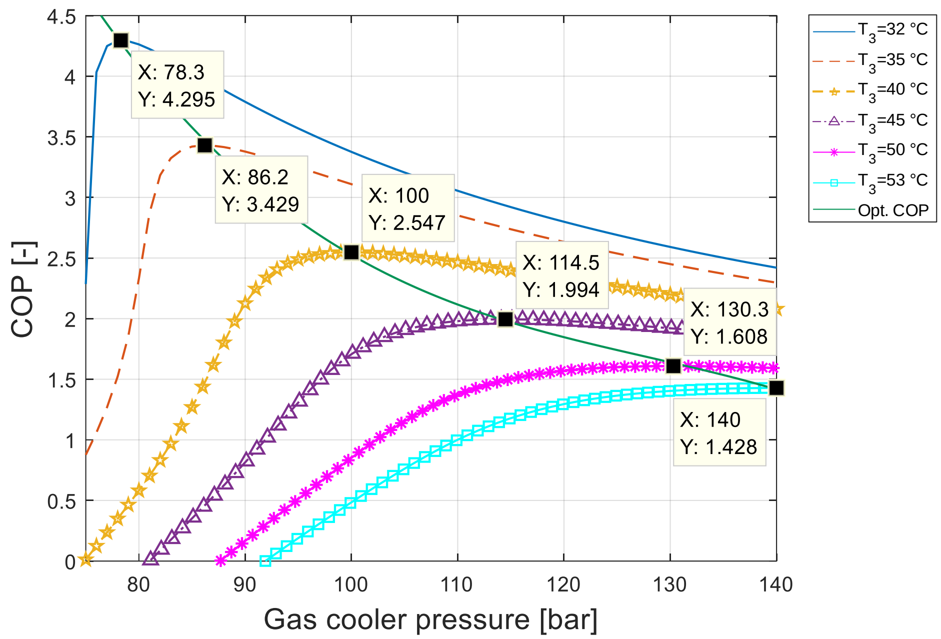

Figure 3-5. The effect of varying the GC pressure on the COP at different GC outlet temperatures and at 15 °C evaporation temperature

The effect of changing the GC outlet temperature on the COP at different GC pressures at 15 °C evaporation temperature is shown in Figure 3-7. It can be noted that the optimum GC pressure increases with the increase of the GC outlet temperature. It is also clear for the shown range that the COP is maximum at the lowest GC outlet temperature. Hence, for the best COP the cooling process in the GC should be the best possible.

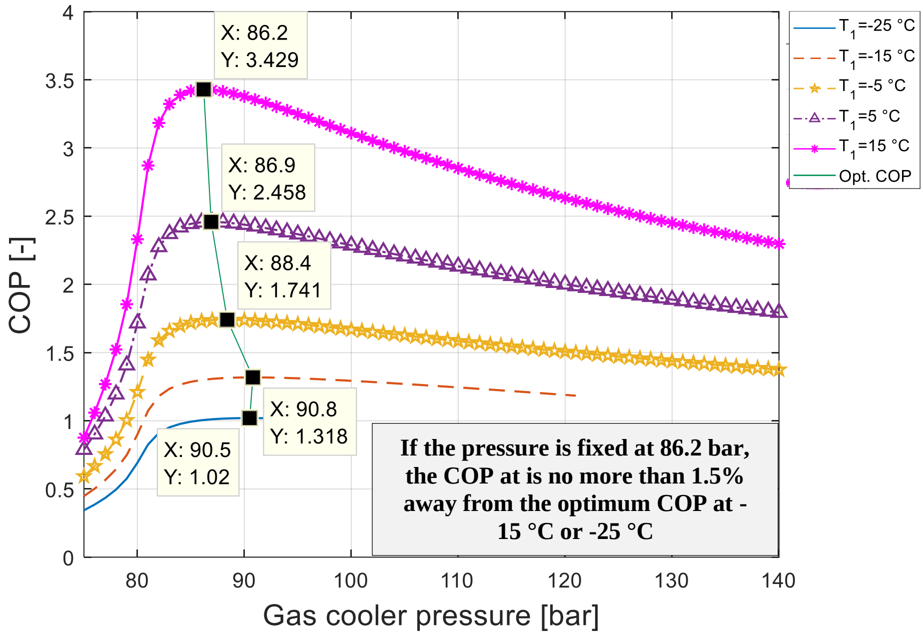

Figure 3-6. The influence of varying the GC pressure on the COP at different evaporation temperatures and at 35 °C GC outlet temperature

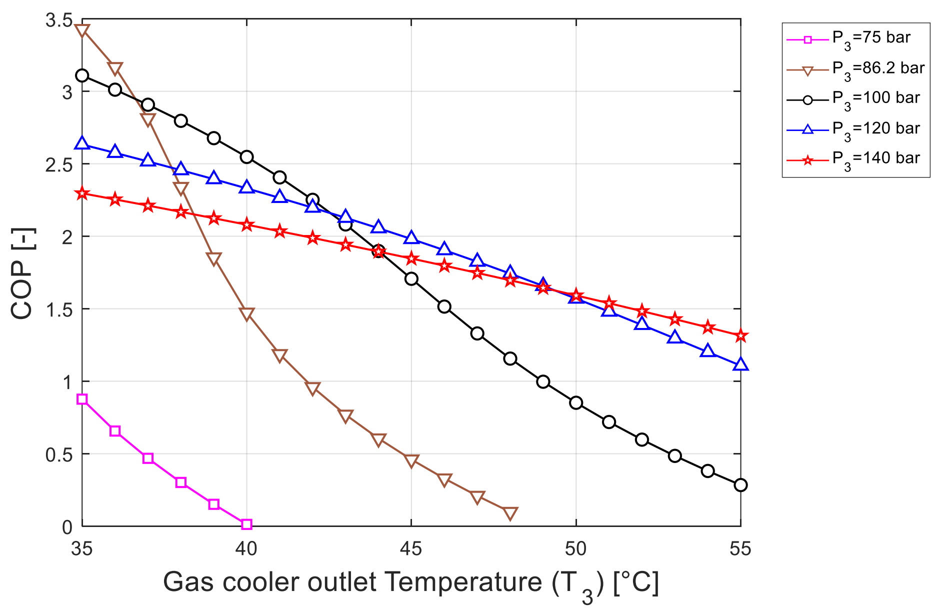

Figure 3-7. The impact of varying the GC outlet temperature on the COP at different GC pressures and at 15 °C evaporation temperature

Figure 3-8 shows that COP increases with the increase of the evaporation temperature as in conventional (subcritical) heat pump cycles. This graph is generated for GC outlet temperature of 35 °C where the 86.2 bar GC pressure line represents the maximum COP line neglecting the effect that the changing evaporation temperature has on the optimum GC pressure. Considering the GC pressure curves for 75, 86.2, and 100 bar, it can be noted that the under-estimation of the optimum GC pressure generates higher reduction in COP compared to the over-estimation of the optimum GC pressure. For instance, at 10 °C evaporation temperature, the COP is 2.85 at 86.2 bar, while the COP at 75 and 100 bar is 0.82 and 2.65 respectively.

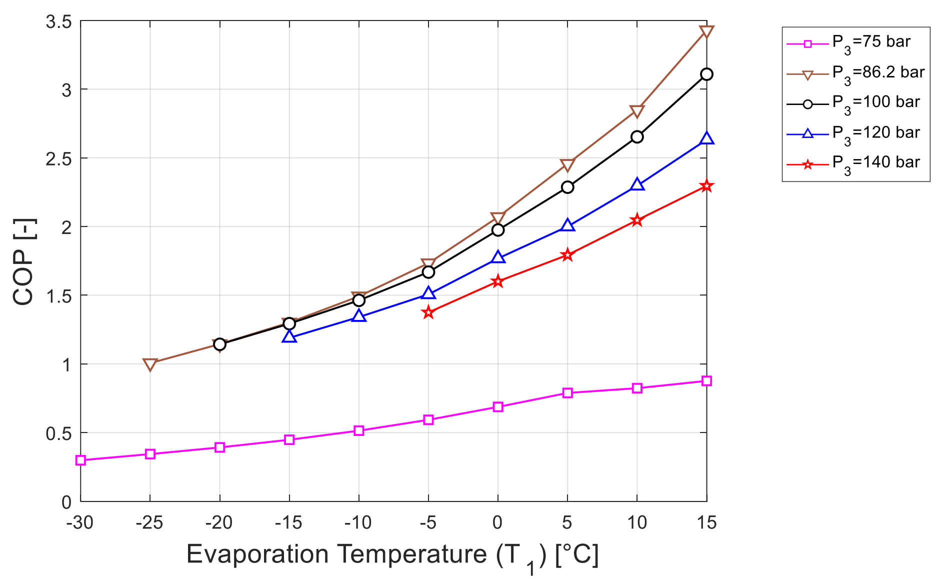

Figure 3-8. The effect of changing the evaporation temperature on the COP at different GC pressures and at 35 °C GC outlet temperature

The impact of the amount of the superheating taking place inside the evaporator, which adds to the cooling capacity at various GC pressures is plotted in Figure 3-9 for GC outlet temperatures of 35 °C and 45 °C, both at 15 °C evaporation temperature. At 35 °C, the superheating has a negligible effect at all GC pressure except at 75 bar. At 45 °C, the superheating has a considerable effect on the COP for 75 and 100 bar GC pressures. It can be concluded that at most GC pressures, the superheating has hardly an influence on the COP, especially if the GC pressure is much greater than the critical pressure. However, if the GC pressure is close to the critical pressure, COP can significantly increase with an increasing amount of superheating, and even more so if additionally, the GC outlet temperature is high.

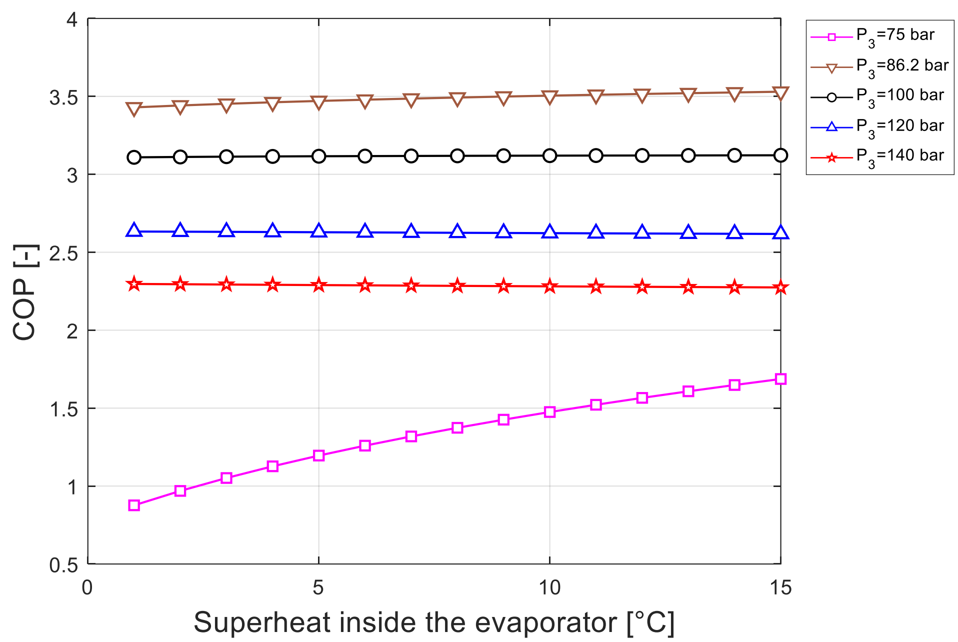

Figure 3-9. The influence of the superheating on the COP at 15 °C evaporation temperature; 35 °C GC outlet temperature

3.4 Optimization Correlation

Based on the above analysis, for our compressor and operating ranges, the GC outlet temperature is the most influential parameter on the optimum GC pressure. A second-order polynomial is developed based on the simulated points shown in Figure 3-11, which is calculated at a 15 °C evaporation temperature and 1K total superheat. The polynomial is plotted in thick green.

$$p_{GC,opt} = 8.197 + 1.717T_{GCo} + 0.01448{T_{GCo}}^2 \tag{3.12}$$

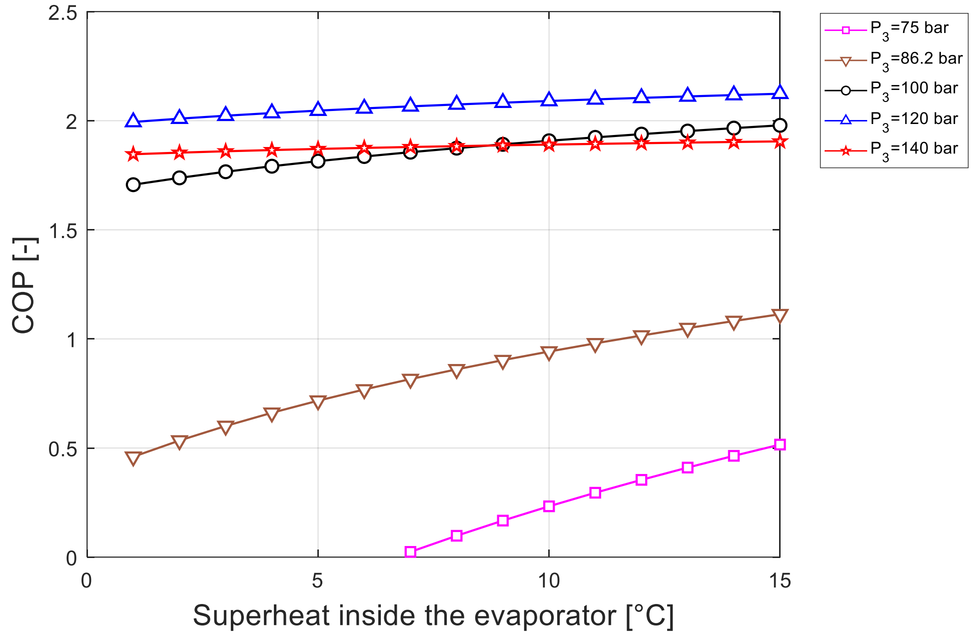

Figure 3-10. The influence of the superheating on the COP at 15 °C evaporation temperature; 45 °C GC outlet temperature

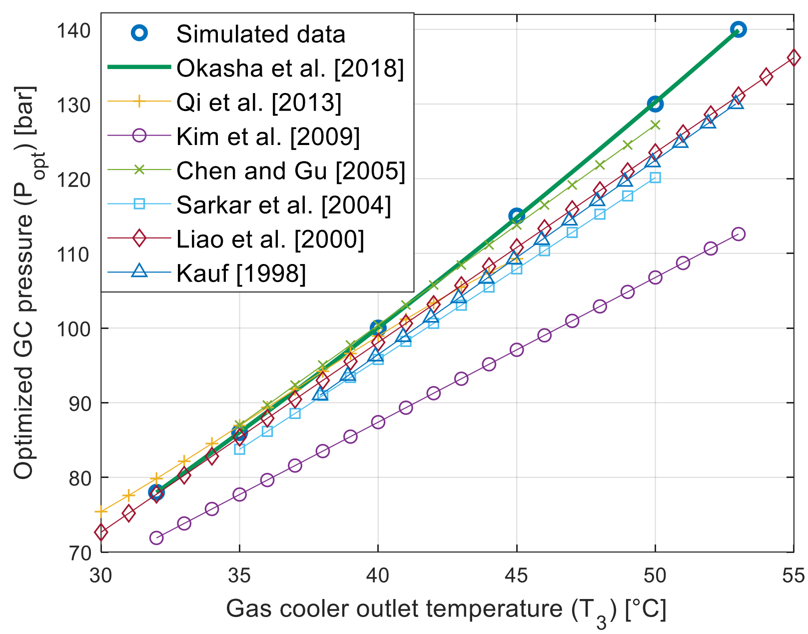

Figure 3-11: Developed correlation for optimized GC pressure shown in thick green curve compared to correlations available in the literature

This correlation is developed for the range of operating conditions of 32 °C < T_{GCo} < 53 °C and 75 bar <$p_{GC,opt}$< 140 bar. Figure 3-11 shows the developed correlation in comparison with the common ones in the literature displayed with their respective valid range.

In this chapter, the CO_2 transcritical cycle was modeled and analyzed. For the selected compressor, the isentropic and volumetric efficiency correlations are developed from simulated data points at three different evaporation temperatures. The efficiency correlations are compared to correlations from the literature. The isentropic efficiency varies considerably between different compressors; hence, selecting the appropriate correlations for simulating the cycle behavior is important. The effect of the GC outlet pressure and temperature, the evaporation temperature, and the useful superheat taking place inside the evaporator on the COP are investigated and discussed. The GC outlet temperature is the most influential parameter on the optimum GC pressure. The evaporation temperature has a negligible effect on the optimum GC pressure. An optimized offline control correlation is developed and compared to common ones in the literature. The correlation relates the optimized GC pressure to the GC outlet temperature, which can be used to maximize the transcritical cycle COP for relevant range of operating conditions.

Chapter 4: Multi-Objective Optimization

Maximizing COP is equivalent to minimizing the work consumed by the compressor for a certain amount of cooling capacity as shown in [43], which translates into minimizing fuel/energy consumption. However, this does not mean that the system is working at its highest cooling/heating capacity that may be desired for example in a transient start-up operation to cool down or heat up a space as quickly as possible to a certain condition or for a continuous load that is higher than at the maximum COP. In this work, the trade-off between maximizing COP and the cooling capacity ($\dot{Q}_c$) is analyzed and the results are equally valid for the heating capacity. The best solutions for both objectives of maximizing COP and $\dot{Q}_c$ are presented by a Pareto Front for given operating conditions. The solutions that construct the Pareto Front are equally good and cannot be dominated by other solutions. Each solution of the Pareto Front has a unique GC pressure and superheat that can be used as reference values for the system controller. Here, the Non-Dominated Sorting Genetic Algorithm II (NSGA-II) [48] is used to generate the Pareto Front with the best non-dominated solutions between the COP and $\dot{Q}_c$ for any set of operating conditions, based on a transcritical CO_2 thermodynamic model presented in Chapter 3. An optimization parameter k that ranges from 0 to 1 is introduced to easily select maximum COP, maximum $\dot{Q}_c$, or trade-off solutions in between. The methodology can be applied for transcritical cycles in cooling and heating applications, including a simple cycle, or modified cycles like with an IHX, an expander, an ejector, or multi-stage compressor cycles, and for different working fluids. It is here discussed for the example of using CO_2 (R744) in a simple cycle.

By referring to Figure 3-1, the simulation and analysis assumes (1) the cycle operates at steady-state, (2) CO_2 is a pure fluid neglecting the effect of a lubricant on the properties, (3) the compression process is adiabatic but non-isentropic, (4) the only heat exchange occurs in the heat exchangers, hence, the superheat is useful, (5) no pressure drop occurs in the heat exchangers and CO_2 lines, hence $p_1 = p_4$ and $p_2 = p_3 = p_{GC}$ and (6) The compressor volumetric and isentropic efficiencies are not affected by compressor speed. The compressor typically has a high-side pressure limit, which is set here at 140 bar.

Figure 4-1 shows the p-h diagram for CO_2 with a simple transcritical cycle operating as an example at GC outlet temperature of 32 °C, GC pressure of 85 bar, and evaporation temperature of 15 °C.

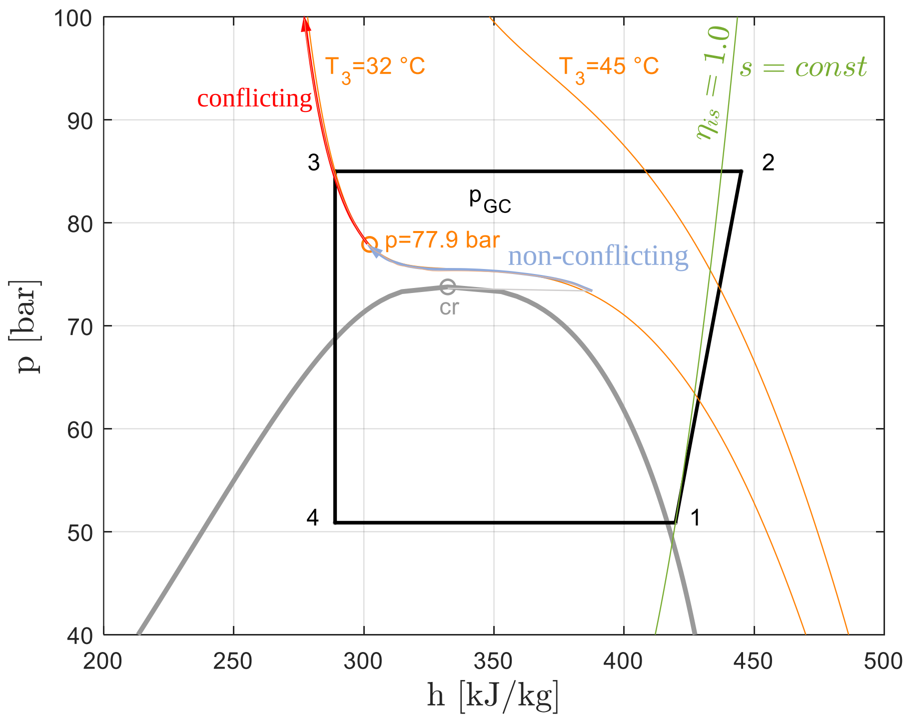

Figure 4-1. p-h diagram for CO_2 with simple transcritical cycle at T_3=32 °C, p_{GC}=85 bar, and T_1=15 °C

The constant temperature line for 32 °C and 45 °C and a line with constant entropy $s=s_1$ are shown in orange and green respectively. It can be inferred that $\dot{Q}_c$ increases with the increase of p_{GC} at constant T_1 and T_3. Due to the more pronounced S-shape of the isotherms near the critical point, the increase of $\dot{Q}_c$ near the critical point is higher than far away from the critical point. With the increase of p_{GC}, the compression power also increases but in an almost linear fashion. There is a point where the relative increase in $\dot{Q}_c$ becomes less than the relative increase in the compression power. At this point, COP reaches its maximum. It can be found by equating the derivative of the COP with respect to p_{GC} to zero [14]

$$\frac{\partial COP}{\partial p_{GC}} = \frac{-\left(\frac{\partial h_3}{\partial p_{GC}}\right)_{T_3}(h_2 - h_1) - \left(\frac{\partial h_2}{\partial p_{GC}}\right)(h_1 - h_3)}{(h_2 - h_1)^2} = 0 \tag{4.1}$$

where h_2 is a function of h_{2is} and η_{is} (Eqn. (3.6)), and η_{is} can also depend on p_{GC}. The maximum COP condition is then

$$-\frac{\left(\frac{\partial h_3}{\partial p_{GC}}\right)_{T_3}}{(h_1 - h_3)} = \frac{\left(\frac{\partial h_2}{\partial p_{GC}}\right)}{(h_2 - h_1)} \tag{4.2}$$

showing that at this point along the T_3 isotherm with increasing p_{GC}, the decrease of h_3 relative to the mass-specific cooling capacity equals the increase of h_2 relative to the mass-specific compression work. For the cycle in Figure 3-1, this point is indicated on the $T_3 = 32$ °C isotherm at $p_{GC} = 77.9$ bar. At GC pressures below this point, higher COP and larger $\dot{Q}_c$ are non-conflicting objectives. Both objectives are conflicting at GC pressures above this point, where with increasing p_{GC} the COP decreases while $\dot{Q}_c$ increases further. Figure 4-2 shows how COP develops with varying p_{GC} at $T_3 = 32$ °C, $T_1 = 15$ °C, $\omega = 1800$ rpm, and $T_{sh} = 1$ K for three compressors efficiency correlations ([49], [50], [51]) and constant efficiencies of 0.7. The optimum pressure for the maximum COP varies only insignificantly by 0.7% around the mean across the presented efficiencies and operating conditions.

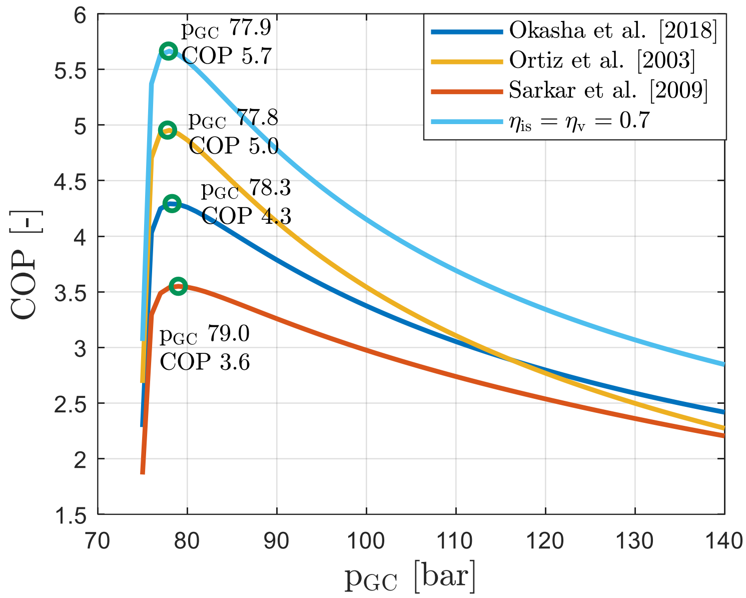

Figure 4-2. Effect of varying p_{GC} at T_3=32 °C, T_1=15 °C, ω=1800 RPM, T_{sh}=1 K, and with four different compressor efficiency correlations on COP

The maximum $\dot{Q}_c$ can be found at

$$\frac{\partial \dot{Q}_c}{\partial p_{GC}} = \frac{\partial \dot{m}}{\partial p_{GC}}(h_1 - h_3) + \dot{m}\left(\frac{\partial h_3}{\partial p_{GC}}\right)_{T_3} = 0 \tag{4.3}$$

and if the compressor volumetric efficiency is constant, i.e., the mass flow rate is constant with changing p_{GC}, Eqn. (4.3) simplifies to

$$\left(\frac{\partial h_3}{\partial p_{GC}}\right)_{T_3} = 0 \tag{4.4}$$

This condition occurs for CO_2 at much higher pressures in the range of about 400…500 bar. Hence, the maximum $\dot{Q}_c$ appears at the maximum p_{GC} allowed in the system, which is here at 140 bar. Figure 4-3 is generated using the same volumetric efficiencies used in Figure 4-2. If the volumetric efficiency decreases with increasing compressor pressure ratio p_{GC}/p_1, the mass flow rate reduces (Eqn. (3.7)). With the mass flow rate reducing with higher compressor pressure ratios, $\dot{Q}_c$ can increase or decrease with increasing p_{GC}, depending on whether the increase of the enthalpy difference across the evaporator or the mass flow reduction is dominant. This effect is observed in Figure 4-3 where the maximum $\dot{Q}_c$ (purple circle) occur at pressures of 97.3, 106.9, 122 bar for the efficiency correlations from [51], [49], and [50] respectively, and at the maximum allowed pressure in the system of 140 bar for constant volumetric efficiency, corresponding with Eqn. (4.4). Except the 140 bar, these pressure values mark the point, where the mass flow rate reduction due to the increase of pressure ratio starts to dominate over the increase of the enthalpy difference across the evaporator. In the pressure range from the maximum COP (green circle in Figure 4-2) to the maximum $\dot{Q}_c$ (purple circle in Figure 4-3) for each efficiency correlation, these two objectives are conflicting, whereas in the range from the critical pressure to the p_{GC} with maximum COP (left of the green circle in Figure 4-2) these two objectives are non-conflicting, as also indicated in Figure 4-1.

Considering the above analysis, it can be of interest to exploit the feature of transcritical cycles that by adjusting the GC pressure: maximum COP, maximum $\dot{Q}_c$, any trade-off point between these both, or lower $\dot{Q}_c$ below the point of maximum COP can be obtained. While maximum COP can be of interest for minimal energy consumption, maximum $\dot{Q}_c$ may be of interest especially for transient operation (e.g. for quickly achieving thermal comfort at start-up or change of set-point). A trade-off point between maximum COP and maximum $\dot{Q}_c$ can be selected by a controller as a compromise between energy efficiency and thermal comfort. Working with reduced $\dot{Q}_c$ at GC pressures below the point of maximum COP can be employed at low load to avoid on-off cycling of the compressor.

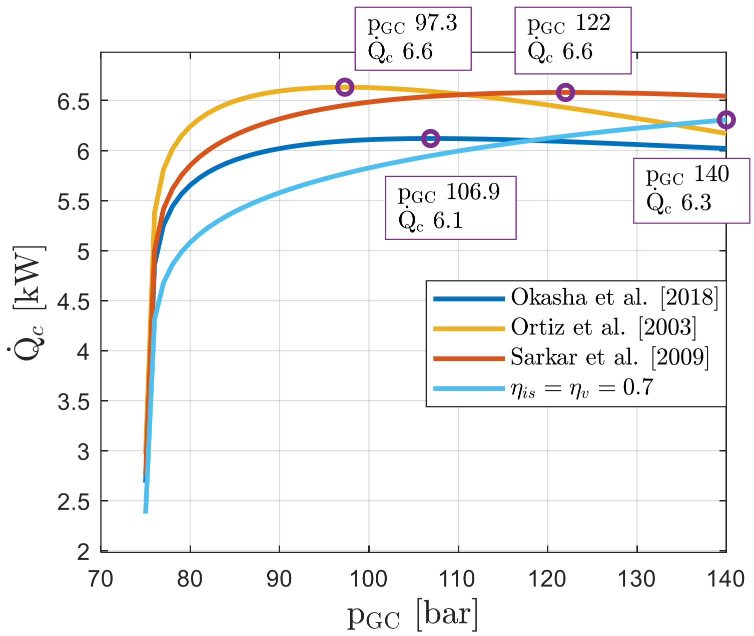

Figure 4-3. Effect of varying p_{GC} at T_3=32 °C, T_1=15 °C, ω=1800 RPM, and T_{sh}=1 K, and with four different compressor efficiency correlations on $\dot{Q}_c$

Exploiting the features of transcritical cycles, it can be beneficial to transition by purpose from a subcritical cycle to a transcritical cycle by allowing T_3 to increase, especially if T_3 is already close below the critical temperature. As an example, benefits in terms of percentage increase of COP and $\dot{Q}_c$ respectively are shown in Figure 4-4 and Figure 4-5 for a cycle operating with $T_1 = 15$ °C, and $T_{sh} = 1$ K, and constant compressor efficiencies of 0.7.

Figure 4-4 and Figure 4-5 indicate an increase of COP by more than 7% and simultaneously an increase of $\dot{Q}_c$ by more than 16% when transitioning from a subcritical cycle with $T_3 = T_{3sub} = T_{cr} - 0.1$ K to a transcritical cycle with $T_3 = T_{3sup} = T_{cr} + 0.1$ K and optimum GC pressure for maximum COP (75.7 bar), i.e. by allowing T_3 to increase by only 0.2 K while increasing p_{GC} by ~2.1 bar. Keeping then $T_3 = T_{3sup} = T_{cr} + 0.1$ K and further increasing the GC pressure to the optimum for maximum $\dot{Q}_c$, $\dot{Q}_c$ can be further increased while then reducing COP again due to the conflicting nature of these two objectives in this range. The COP and $\dot{Q}_c$ gains of transitioning from a subcritical cycle to a transcritical cycle diminish as further away T_3 is from the critical temperature as Figure 4-4 and Figure 4-5 show for the presented conditions. The next section describes the problem formulation for the bi-objective optimization in the range from maximum COP to maximum $\dot{Q}_c$.

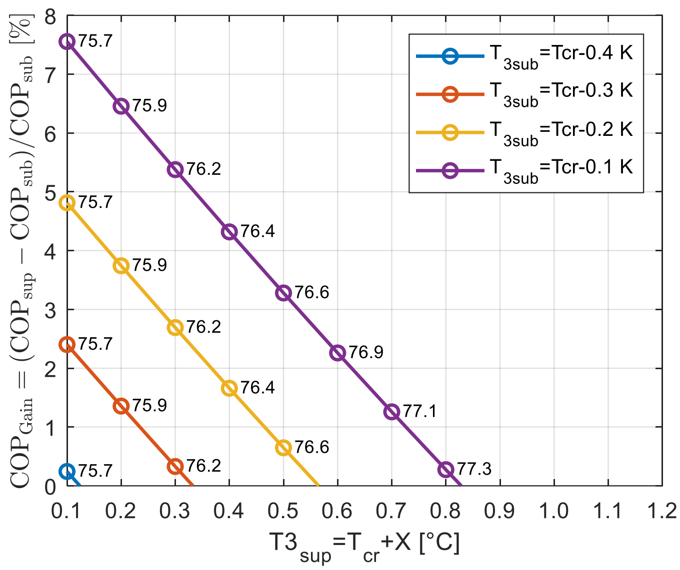

Figure 4-4. The COP gain for transitioning from a subcritical cycle with T_3 close to T_{cr} to a transcritical cycle, keeping T_1=15 °C, ω=1800 RPM, T_{sh}=1 K, and η_{is} = η_v = 0.7. Optimum pressures are in bar

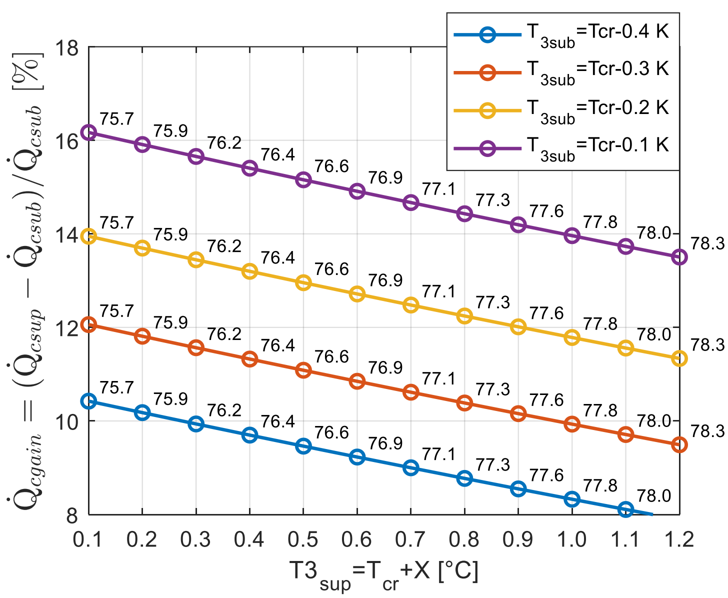

Figure 4-5. The $\dot{Q}_c$ gain for transitioning from a subcritical cycle with T_3 close to T_{cr} to a transcritical cycle, keeping T_1=15 °C, ω=1800 RPM, T_{sh}=1 K, and η_{is} = η_v = 0.7. Optimum pressures are in bar

4.1 Bi-objective Optimization

4.1.1 Problem Formulation

A bi-objective trade-off Pareto Front between COP and $\dot{Q}_c$ for the transcritical vapor compression cycle and here for CO_2 as a refrigerant is generated and exploited for the control objective based on the preference whether maximum COP (minimum energy consumption), maximum $\dot{Q}_c$ (achieving maximum cooling), or working at a trade-off point between the two is desired. The optimization problem considers at any point satisfying the two conflicting objectives:

$$\text{Maximize COP}$$

$$\text{Maximize } \dot{Q}_c$$

The optimization variables considered are T_3, p_{GC}, T_1, T_{sh}, and ω. T_3 is dependent on e.g. the ambient temperature and p_{GC} is independent of the GC outlet temperature. The useful superheat can be monitored and controlled for systems without compressor suction line accumulator that is to prevent otherwise liquid refrigerant from entering the compressor at low evaporator loads. The variable bounds considered for the optimization problem are:

$$32\ °C < T_3 < 45\ °C \tag{4.5}$$
$$75\ \text{bar} < p_{GC} < 140\ \text{bar} \tag{4.6}$$
$$-25\ °C < T_1 < 15\ °C \tag{4.7}$$
$$1\ K < T_{sh} < 10\ K \tag{4.8}$$
$$1000\ \text{rpm} < \omega < 1800\ \text{rpm} \tag{4.9}$$

For relevant solutions, the problem formulation is subject to the constraints

$$\dot{Q}_c > 0, \dot{W}_{comp} > 0 \tag{4.10}$$

Since compressor efficiencies vary for different compressors [49]; and to keep this analysis independent of a particular compressor, the isentropic and volumetric efficiency are both assumed to be constant ($\eta_{is} = \eta_v = 0.7.$)

4.1.2 Evolutionary Multi-objective Optimization Algorithm

Classical direct and gradient based methods may converge to a suboptimal solution instead of an optimal solution if the initial condition changes. In addition, classical methods need to run a single-objective optimizer many times to obtain a Pareto Front. Moreover, good distribution (or diversity) of the Pareto Front solutions is not guaranteed. The Non-dominated Sorting Genetic Algorithm II (NSGA-II) [48] used here is an evolutionally algorithm that overcomes the limitations of classical methods. Figure 4-6 shows a schematic outline of how the NSGA-II works. The algorithm starts with a random parent population $\mathrm{P_t}$ with size N and creates an offspring population $\mathrm{O_t}$ having the same size as the parent population. These two populations are lumped together to form $\mathrm{R_t}$ with population size 2N. The objective functions (i.e. COP & $\dot{\mathrm{Q}}_c$) are calculated for the combined population $\mathrm{R_t}$. A non-dominated sorting (a hierarchical partial ordering operation) is then performed on $\mathrm{R_t}$ to classify it into several fronts ($\mathrm{F_1}$, $\mathrm{F_2}$, $\mathrm{F_3}$, ...). The solutions are sorted in an ascending level of non-domination. The next generation population $\mathrm{P_{t+1}}$ is formed by copying fronts from the top of the hierarchical list. To maintain the fixed population size of $\mathrm{P_t}$, the copying operation is continued until no more complete fronts can be accepted. Then, the final front that could not be accepted completely is operated with a diversity preserving operator to select the required number of points, i.e., preserve them and reject the rest of the final front population. NSGA-II employs a computationally fast crowding distance operator for this purpose. The above method works iteratively in generations to (i) emphasize non-dominated solutions in a population, (ii) emphasize diverse solutions in a population, and (iii) emphasize previously found good solutions for both COP & $\dot{\mathrm{Q}}_c$ objectives. Along with NSGA-II's offspring population creation, the selection criteria help a randomly created population to progress towards the Pareto-optimal front with generations. The number of population and generation have been selected after some test runs as 200 for each.

4.2 Best Trade-off Solutions

4.2.1 Obtained Pareto Front

Figure 4-7 shows the best non-dominated optimum solutions in blue that is the finally obtained Pareto Front (here referred to as Pareto Front). A parameter k is introduced that ranges from zero to 1. Zero represents the maximum COP solution and 1 the maximum $\dot{Q}_c$ solution, whilst for example $k = 0.4$ represents the 40th percentile of the sorted non-dominated solutions that start with the maximum COP, hence being closer to the maximum COP than to the maximum $\dot{Q}_c$ solution. Each solution of the Pareto Front has a corresponding variable space solution, i.e., a corresponding GC outlet temperature, GC pressure, evaporation temperature, useful superheat, and compressor speed. All the Pareto Front solutions are found at the minimum T_3, the maximum T_1, and the maximum ω. The maximum COP occurs at $p_{GC} = 77.5$ bar and $T_{sh} = 10.0$ K, while the maximum $\dot{Q}_c$ occurs at $p_{GC} = 140$ bar and $T_{sh} = 1.0$ K. Table 4-1 shows the variable and objective values for five selected solutions: the maximum COP ($k = 0$), the maximum $\dot{Q}_c$ ($k = 1$), and three trade-off solutions ($k = 0.25, 0.5$, and 0.75). The five solutions are marked in Figure 4-7. Figure 4-8 shows the heat pump cycles corresponding to the five marked solutions in a p-h diagram.

Table 4-1. Pareto Front variable and objective values for five selected solutions: maximum COP, maximum $\dot{Q}_c$, and three trade-off solutions

k	Objectives		Variables				
	COP [-]	$\dot{Q}_c$ [kW]	T_3 [°C]	p_{GC} [bar]	T_1 [°C]	T_{sh} [K]	ω [rpm]
0	5.8	4.8	32	77.5	15	10.0	1800
0.25	5.3	5.3	32	83.4	15	10.0	1800
0.5	4.5	5.7	32	93.8	15	1.0	1800
0.75	3.7	6.0	32	108.6	15	1.0	1800
1.0	2.8	6.3	32	140.0	15	1.0	1800

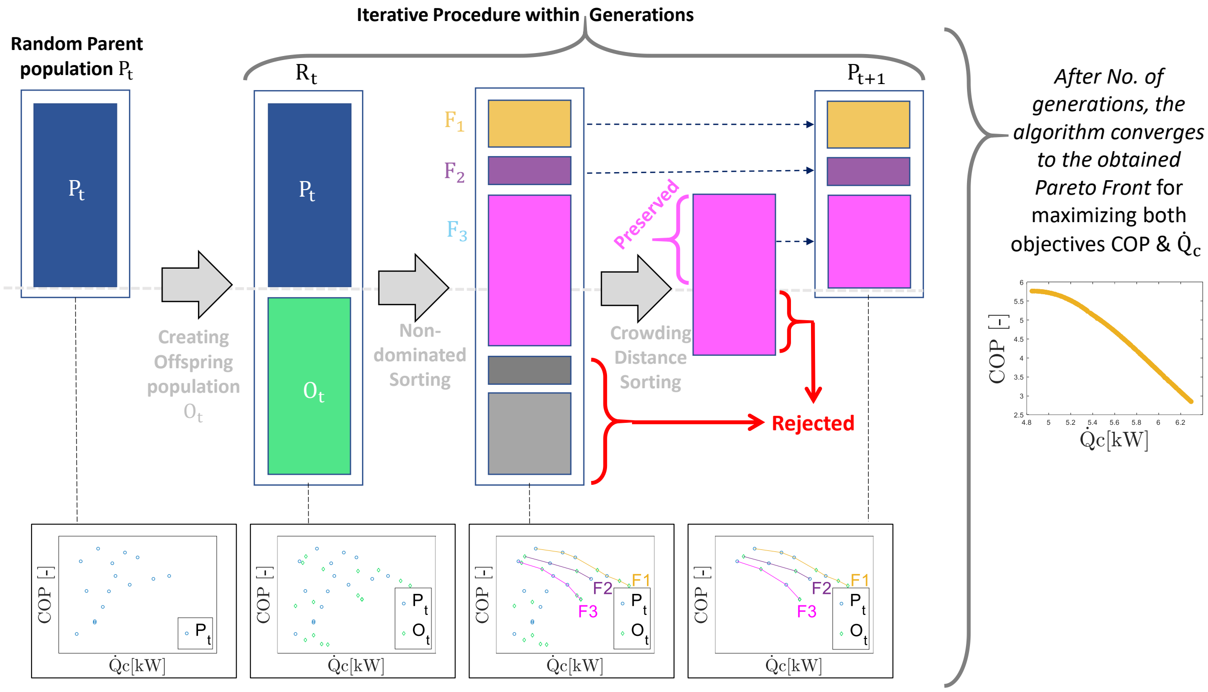

Figure 4-6. Schematic of NSGA-II maximizing both objectives COP and $\dot{Q}_c$

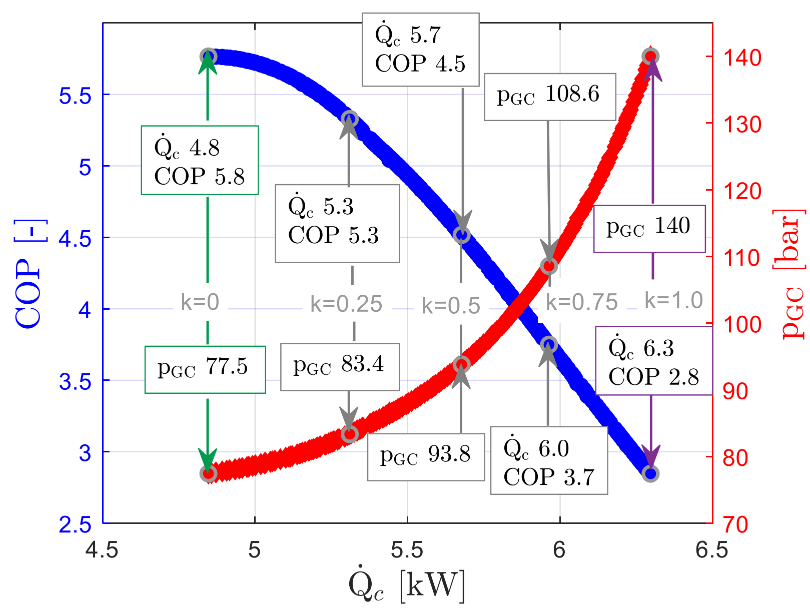

Figure 4-7. Pareto Front for maximizing both COP and $\dot{Q}_c$ with corresponding GC pressures. Solutions labeled with k=0 and k=1 are the maximum COP and $\dot{Q}_c$ solutions respectively. Solutions with k=0.25, 0.25, and 0.75 are labeled as example trade-off solutions.

In Figure 4-8, the green cycle with $p_{GC} = 77.5$ bar presents the cycle that produces the maximum COP of 5.8. The purple cycle with p_{GC} = 140 bar presents the cycle that produces maximum $\dot{Q}_c$ of 6.3 kW. The three gray cycles in between present cycles for the three examples of best trade-offs between maximum COP and $\dot{Q}_c$, where both COP and $\dot{Q}_c$ are less than their maximum achieved with the green and the purple cycles respectively. For increasing GC outlet temperatures, the green circles connected by the green dotted line show the trend of state 3 for cycles operating at maximum COP, and the purple circles connected by the purple line show the trend of state 3 for cycles operating at maximum $\dot{Q}_c$. Because the volumetric compressor efficiency is constant, the maximum $\dot{Q}_c$ occurs at the maximum allowed GC pressure (Eqn. (4.4).)

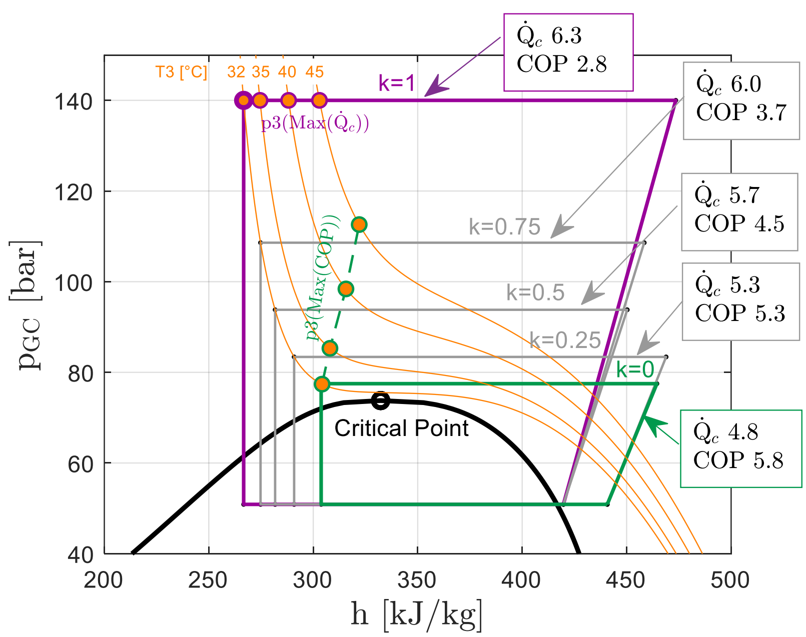

Figure 4-8. p-h diagram indicating the cycles for the five solutions labeled on the Pareto Front in Figure 4-7. The green cycle produces the maximum COP, the purple cycle the maximum $\dot{Q}_c$, and the grey cycles represent the three example trade-off solutions.

4.2.2 Gain to Loss Ratio for moving from one solution to another

All the Pareto Front solutions between the maximum COP and the maximum $\dot{Q}_c$ solutions represent optimized trade-off solutions. A gain to loss ratio can be defined as the ratio of the gain on the objective that is to increase (COP or $\dot{Q}_c$) over the loss on the other objective ($\dot{Q}_c$ or COP) when moving from one solution to another by adjusting the GC pressure. Hence, it can be written as

$$\begin{aligned} \mathrm{G/L} &= \frac{\text{Gain in } \dot{Q}_c}{\text{Loss in COP}}, \text{ when moving to the right to increase } \dot{Q}_c \\ \mathrm{G/L} &= \frac{\text{Gain in COP}}{\text{Loss in } \dot{Q}_c}, \text{ when moving to the left to increase COP} \end{aligned} \tag{4.11}$$

Figure 4-9 shows the normalized Pareto Front for maximizing both COP and $\dot{Q}_c$ used for the G/L calculations. Table 4-2 contains the G/L ratio calculations for both moving from left to right and right to left between k values of 0, 0.25, 0.5, 0.75, and 1. The distances d_1 through d_8 are the differences in normalized COP and $\dot{Q}_c$ between these solutions in the Pareto Front as shown in Figure 4-9. For example, if the system is operating at maximum COP with k=0, there may be a motivation to move to right to e.g. $k = 0.25$ to increase $\dot{Q}_c$ considerably (more than double as much in its range then COP would reduce in its range) while reducing COP acceptably. Differently, if the system is operating at a pressure corresponding to $k = 0.25$, i.e., $p_{GC} = 83.4$ bar, the motivation may be less to move to a neighboring point for the betterment of either objectives. Therefore, the G/L can be used as a determining factor for moving from one solution to another depending on the desired system performance. The G/L ratio can be calculated on a normalized basis as above, if the evaluation emphasizes on utilization of available range between the two objectives, or on an absolute basis if the ratio of percent increase over percent decrease is of relevance. For the latter, Eqn. (4.11) can be formulated as

$$\begin{aligned} \mathrm{G/L} &= \frac{[\dot{Q}_c(k_{i+1}) - \dot{Q}_c(k_i))]/\dot{Q}_c(k_i)}{[\mathrm{COP}(k_i) - \mathrm{COP}(k_{i+1})]/\mathrm{COP}(k_i)}, \text{ when moving to the right to increase } \dot{Q}_c \\ \mathrm{G/L} &= \frac{[\mathrm{COP}(k_{i-1}) - \mathrm{COP}(k_i)]/\mathrm{COP}(k_i)}{[\dot{Q}_c(k_i) - \dot{Q}_c(k_{i-1})]/\dot{Q}_c(k_i)}, \text{ when moving to the left to increase COP} \end{aligned} \tag{4.12}$$

evaluating at the current point of operation with k_i. Alternatively, gain and loss could be evaluated regarding e.g., the maximum value (respective objective), keeping the basis constant. Results of Eqn. (4.12) for same step size $\Delta k = k_{i+1} - k_i$ like in Table 4-2 with $k_i = [0, 0.25, 0.5, 0.75, 1]$ are shown in Table 4-3, where e.g., moving to the right from k_1=0 to k_2=0.25, $\dot{Q}_c$ increases by 10.4% from 4.8 kW to 5.3 kW and COP reduces by 8.6% from 5.8 to 5.3, resulting in G/L=1.21, which expresses that $\dot{Q}_c$ increases 21% more than COP reduces.

Table 4-2. Gain to loss ratios for five solutions obtained from the normalized Pareto Front

G/L	k_1=0	k_2=0.25	k_3=0.5	k_4=0.75	k_5=1
Moving to the right	$\frac{d_2}{d_1} = 2.13$	$\frac{d_4}{d_3} = 0.91$	$\frac{d_6}{d_5} = 0.75$	$\frac{d_8}{d_7} = 0.74$	-
Moving to the left	-	$\frac{d_1}{d_2} = 0.47$	$\frac{d_3}{d_4} = 1.10$	$\frac{d_5}{d_6} = 1.33$	$\frac{d_7}{d_8} = 1.35$

Table 4-3. Gain to loss ratios for five solutions using absolute values from the Pareto Front (Eqn. (4.12))

G/L	k_1=0	k_2=0.25	k_3=0.5	k_4=0.75	k_5=1
Moving to the right	1.21	0.50	0.30	0.21	-
Moving to the left	-	1.00	2.53	4.32	6.75

While a relative coarse step size like that presented in Table 4-2, Table 4-3, Figure 4-9 and Figure 4-10 may already be practical, also any smaller reasonable Δk can be chosen instead, and G/L can also be evaluated e.g. on an absolute basis by

$$G/L = \frac{\left(\frac{d\dot{Q}_c}{dp_{GC}}\right)/\dot{Q}_c}{-\left(\frac{dCOP}{dp_{GC}}\right)/COP}\text{, when moving to the right to increase } \dot{Q}_c$$

$$G/L = \frac{-\left(\frac{dCOP}{dp_{GC}}\right)/COP}{\left(\frac{d\dot{Q}_c}{dp_{GC}}\right)/\dot{Q}_c}\text{, when moving to the left to increase COP} \quad (4.13)$$

Therefore, the trade-off for steady-state or transient can be further modulated by an additional objective function correlating thermal comfort and energy consumption, where the gain to loss ratio can be a determining factor for moving the operating point.

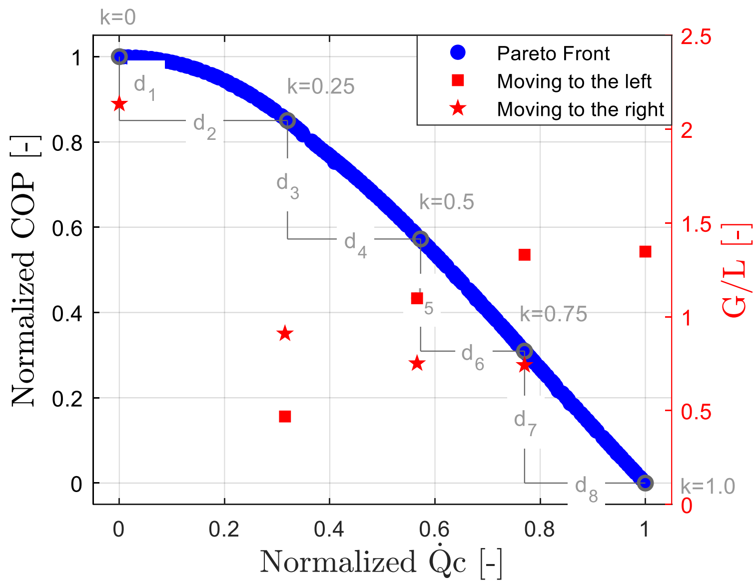

Figure 4-9. Normalized Pareto Front for maximizing both COP, $\dot{Q}_c$ and G/L for moving to right and left with Δk =0.25

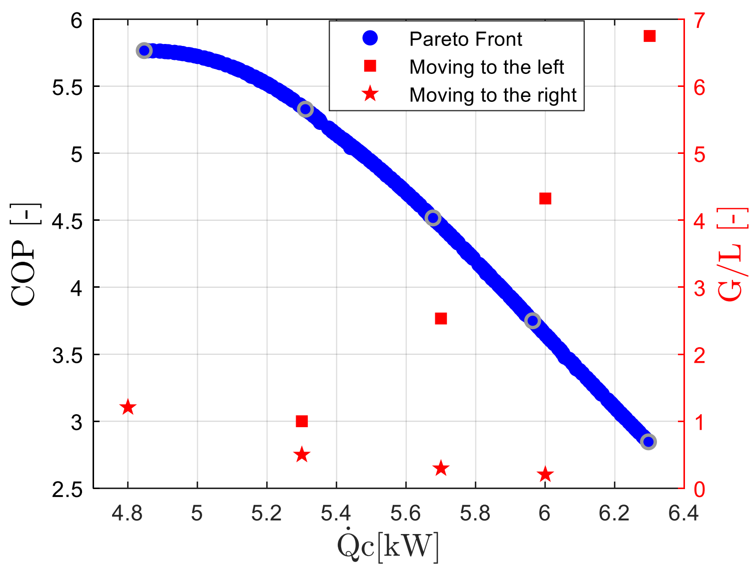

Figure 4-10. Pareto Front for maximizing both COP, $\dot{Q}_c$ and G/L based on absolute values for moving to right and left with Δk =0.25

4.3 Optimization Variables Effect on the Pareto Front

While Table 4-1, Figure 4-7, Figure 4-9, and Figure 4-10 represent the Pareto Front obtained for the entire optimization variable space bound by Equations (4.5) through (4.9), any or all the optimization variables $T_1, T_3, T_{sh},$ and ω can for practical reasons assume values different than in Table 4-1, altering the Pareto Front. The effect of each on the Pareto Front is discussed in this section. The effect of the compressor performance expressed in compressor efficiency correlations on the Pareto Front is analyzed additionally.

4.3.1 Effect of GC Outlet Temperature Change

Figure 4-11 shows the effect of changing GC outlet temperature T_3 on the Pareto Front at $T_1 = 15$ °C, $T_{sh} = 1$ K, $\omega = 1800$ rpm, and on COP and $\dot{Q}_c$ at k values of 0, 0.25, 0.5, 0.75, and 1. Figure 4-12 shows the cycles for $k = 0.5$ with their corresponding GC pressure and each T_3 in a p-h diagram, and also indicates the GC pressure range for the Pareto Front on the isotherm by coloring it with same color as the respective Pareto Front in Figure 4-11. The trend of the Pareto Fronts reflects that $\dot{Q}_c$ increases with decreasing T_3, because the GC outlet enthalpy decreases, enlarging the enthalpy difference across the evaporator. If p_{GC} is set to reflect constant k value, the enthalpy difference across the compressor decreases, and COP increases. Figure 4-11 shows the percentage increase in COP and $\dot{Q}_c$ if T_3 decreases from 45 °C to 40, 35, and 32 °C at $k = 0$ and 1. For example, at $k = 0$, i.e. at the maximum COP solutions, if T_3 decreases from 45 °C to 35 °C, COP and $\dot{Q}_c$ increases by 83% and 14% respectively.

Each Pareto Front spans a different range of GC pressures for each GC outlet temperature as reflected in both figures. The higher the GC outlet temperature, the smaller is the Pareto Front range of optimum solutions. This is due to the increase of the pressure corresponding to the $k = 0$ maximum COP solution (Eqn. (4.2)), while the $k = 1$ maximum $\dot{Q}_c$ solution (Eqn. (4.4)) remains at the maximum allowable system pressure of 140 bar. For example, the Pareto Front minimum pressures are 77.9, 85.3, 98.4, and 112.6 bar for T_3 =32, 35, 40, and 45 °C respectively as indicated in Figure 4-11. For $T_3 = 54$ °C, the Pareto Front collapses into one point presenting the maximum COP and the maximum $\dot{Q}_c$ solution at the maximum system pressure of 140 bar (Eqn. (4.6)). If the system allows a GC pressure higher than 140 bar, then there will be a Pareto Front at 54 °C.

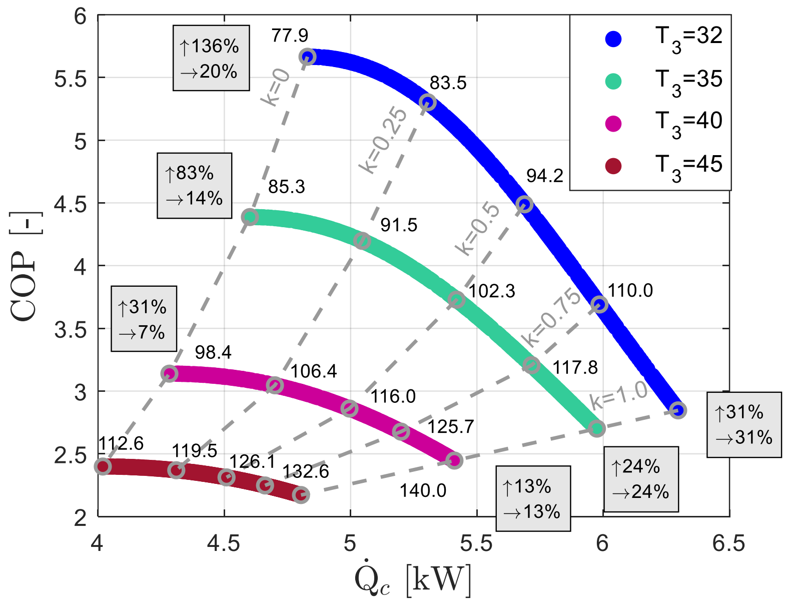

Figure 4-11. Pareto Fronts maximizing both COP and $\dot{Q}_c$ at T_1=15 °C, T_{sh}=1 K, and ω=1800 RPM, for different T_3. The grey lines connect the solutions corresponding to k=0, 0.25, 0.5, 0.75, and 1

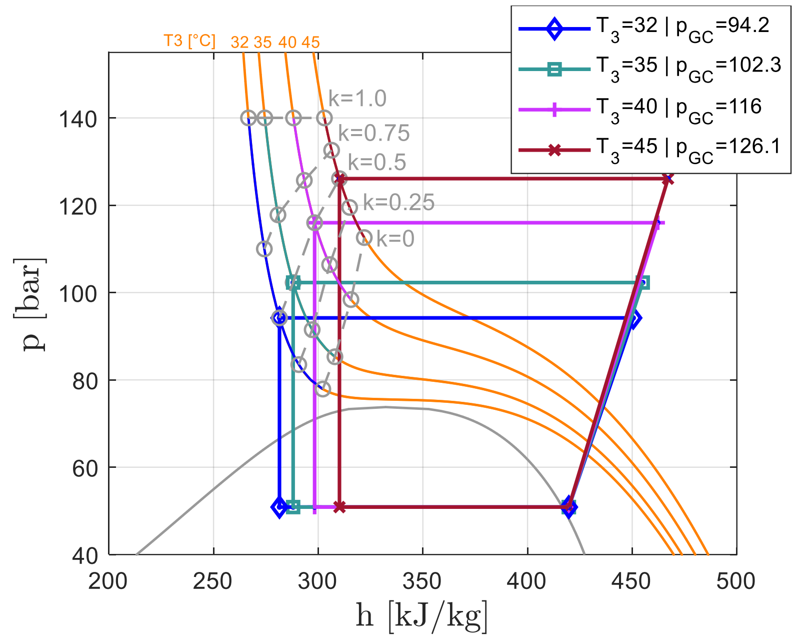

Figure 4-12. p-h diagram with cycles for four different T_3 and T_1=15 °C, T_{sh}=1 K, ω=1800 RPM, k=0.5 from Figure 4-11 . The circle markers on each isotherm represent the corresponding Pareto Front in Figure 4-11

4.3.2 Effect of Evaporation Temperature Change

Figure 4-13 shows the effect of varying evaporator temperature T_1 at $T_3 = 32$ ℃, $T_{sh} = 1$ K, and $\omega = 1800$ rpm. Figure 4-14 shows the cycles for k=0.5 and each T_1 from Figure 4-13 in a p-h diagram. With increasing T_1, the changing Pareto Fronts show both COP and $\dot{Q}_c$ increase for constant k. $\dot{Q}_c$ increases because of increased mass flow with higher vapor density at higher evaporation pressure, overriding the reduced enthalpy difference across the evaporator with increased evaporation temperature due to the shape of the saturated vapor line of the vapor dome. While COP is independent of mass flow rate, it still increases because the relative reduction of enthalpy difference across the compressor is more than across the evaporator. This can be shown by equating the derivative of the COP with respect to T_1 to zero and rearranging to

$$\frac{\frac{\partial(h_1 - h_3)}{\partial T_1}}{(h_1 - h_3)} = \frac{\frac{\partial(h_2 - h_1)}{\partial T_1}}{(h_2 - h_1)} \tag{4.14}$$

It is furthermore noted that for CO_2, the compressor inlet enthalpy increases monotonically with T_1 for all $T_1 < -24.6$ °C, so that the enthalpy difference across the evaporator even increases while it decreases across the compressor, always increasing COP with increasing T_1 in that range. Figure 4-13 also shows the percentage increase in COP and $\dot{Q}_c$ if T_1 increases from -25 to -15, -5, 5, and 15 °C at k=0 and 1. For example, at k=0, i.e. at the maximum COP solutions, if T_1 increases from -25 °C to 5 °C, COP and $\dot{Q}_c$ increases by 151% and 131% respectively. As the evaporation temperature gets lower, the Pareto Front shrinks due to the reduction in both COP and $\dot{Q}_c$ ranges. This shrinking in the Pareto Front continues to just before the evaporation temperature reaches the triple point at -56.6 °C.

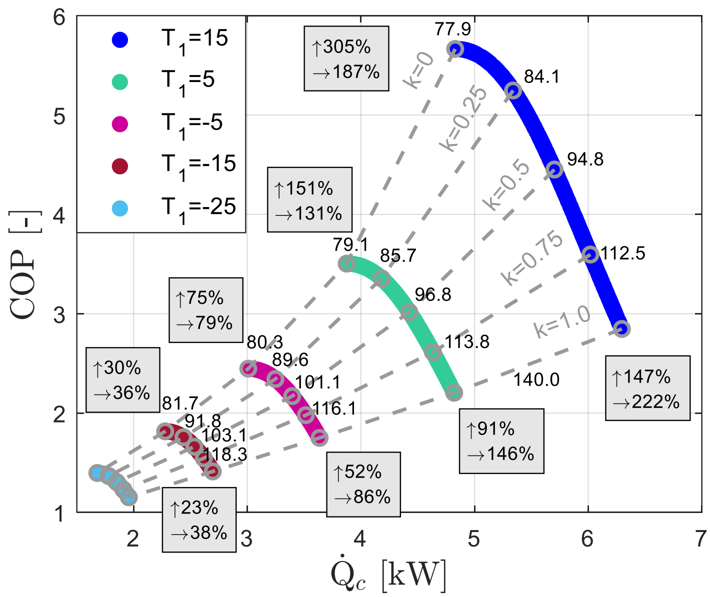

Figure 4-13. Pareto Fronts maximizing both COP and $\dot{Q}_c$ at T_3=32 °C, T_{sh}=1 K, and ω=1800 RPM, for different T_1. The grey lines connect the solutions corresponding to k=0, 0.25, 0.5, 0.75, and 1

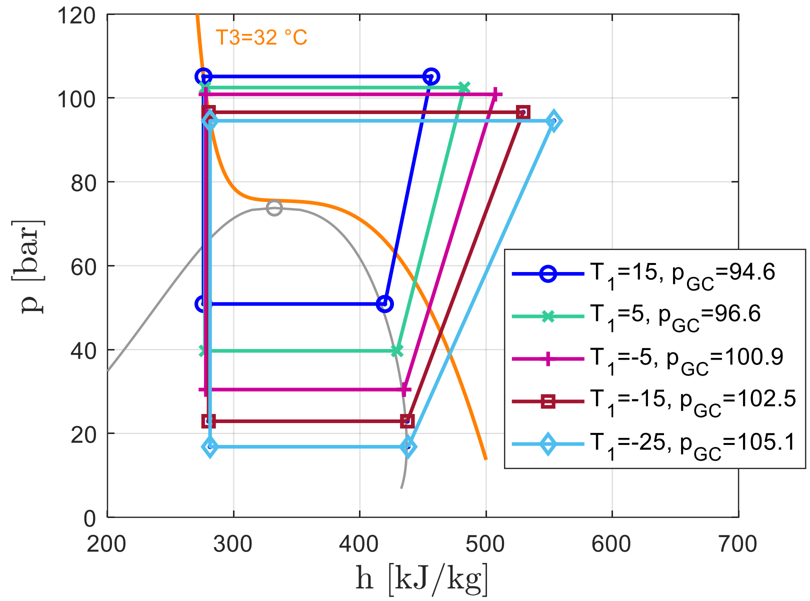

Figure 4-14. p-h diagram with cycles for five different T_1 at T_3=32 °C, T_{sh}=1 K, ω=1800 RPM, and k=0.5 from Figure 4-13

4.3.3 Effect of Useful Superheat

For constant enthalpy at the evaporator inlet, increasing useful superheat T_{sh} increases the enthalpy at the evaporator outlet and hence the enthalpy difference across the evaporator, which acts to increase $\dot{Q}_c$ (Eqn. (3.9)) and COP (Eqn. (3.11)). With increasing T_{sh} also the compressor inlet temperature increases causing competing effects of increased enthalpy difference across the compressor reducing COP, and of lower density at the compressor inlet reducing mass flow rate (Eqn. (3.7)) and hence $\dot{Q}_c$.

Figure 4-15 and Figure 4-16 show the effect of varying T_{sh} for two different cases at $T_3 = 32$ °C and $T_3 = 45$ °C, respectively both at $T_1 = 15$ °C and $\omega = 1800$ rpm, demonstrating that the competing effects can dominate, e.g. for the $k = 1$ maximum $\dot{Q}_c$ solutions (highest p_{GC}) in Figure 4-15, whereas this is not the case in Figure 4-16 and e.g. not for the k=0 maximum COP solutions (lowest p_{GC}) in Figure 4-15. For the increase of T_{sh} from 1 K to 10 K in Figure 4-15, at k=0, COP and $\dot{Q}_c$ increase by 1.8% and 0.4% respectively, while at k=1 both COP and $\dot{Q}_c$ decrease by 1.3%

and 2.0% respectively and in Figure 4-16, both COP and $\dot{Q}_c$ increase at k=0 by 5.5% and 1.0%, and at k=1 by 2.4% and 1.6% respectively. While the changes in COP and $\dot{Q}_c$ resulting from changing T_{sh} can be deemed relative small, their direction depends on the particular operating conditions, with inversions observed at T_3 closer to the critical temperature and high GC pressures, i.e. solutions for larger k (higher $\dot{Q}_c$).

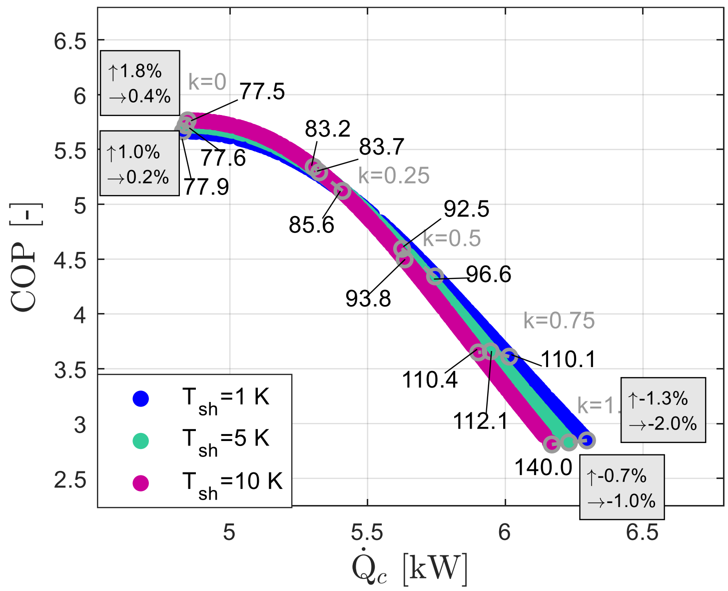

Figure 4-15. Pareto Fronts for maximizing COP and $\dot{Q}_c$ at T_3=32 °C, T_1=15 °C, and ω=1800 RPM, for different T_{sh}. The grey lines connect the solutions corresponding to k=0, 0.25, 0.5, 0.75, and 1

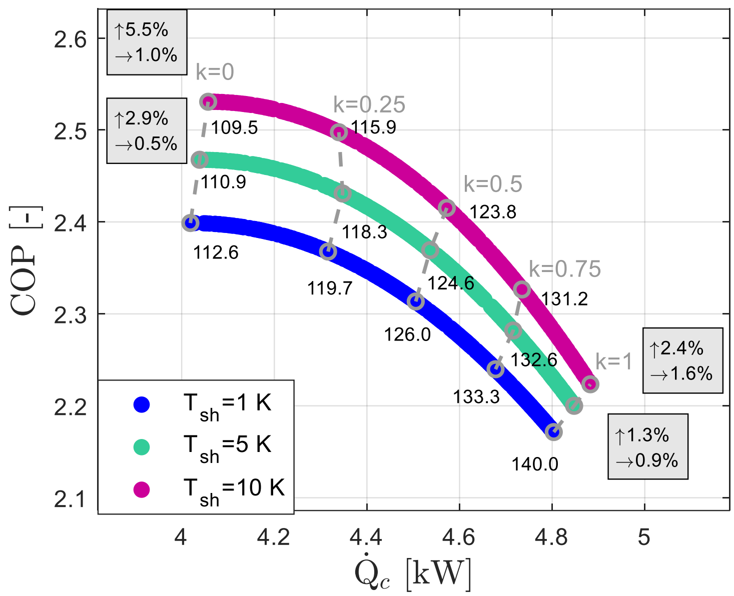

Figure 4-16. Pareto Fronts for maximizing COP and $\dot{Q}_c$ at T_3=45 °C, T_1=15 °C, and ω=1800 RPM, for different T_{sh}. The grey lines connect the solutions corresponding to k=0, 0.25, 0.5, 0.75, and 1

4.3.4 Effect of Compressor Speed

The effect of varying the compressor speed on the Pareto Front is shown in Figure 4-17 for $T_1 = 15$ °C, $T_3 = 32$ °C, and $T_{sh} = 1$ K. As expected, with increasing compressor speed, $\dot{Q}_c$ increases proportionally due to the increase of mass flow rate delivered by the compressor (Eqn. (3.7)) and Eqn. (3.9)). For example, at the k=0 maximum COP solutions, if ω increases from 1000 rpm to 1800 rpm, $\dot{Q}_c$ increases by 80%. The COP remains unaffected with speed change if the compressor volumetric and isentropic efficiency remain the same. In practice, the compressor efficiencies may change with speed.

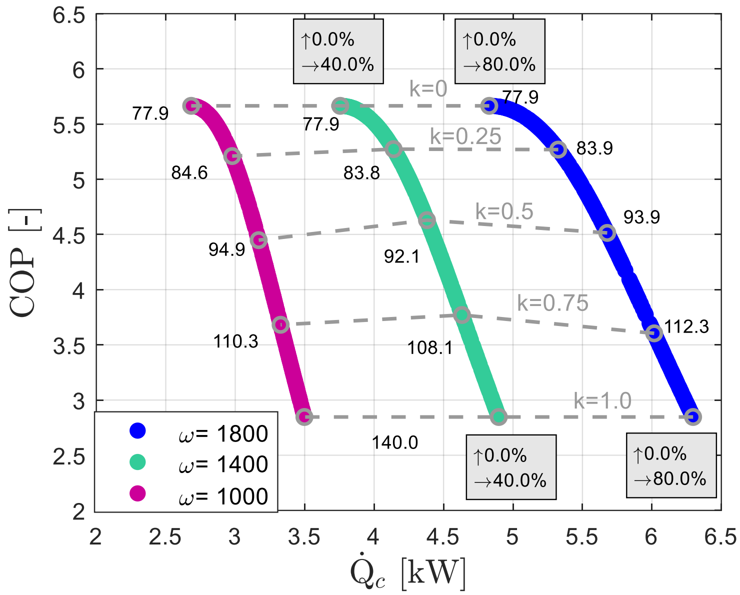

Figure 4-17. Pareto Fronts for maximizing both COP and $\dot{Q}_c$ at T_3=32 °C, T_1=15 °C, and T_{sh}=1 K, for different ω. The grey lines connect the solutions corresponding to k=0, 0.25, 0.5, 0.75, and 1

4.3.5 Effect of Compressor Performance

Figure 4-18 shows for $T_3 = 32$ °C, $T_1 = 15$ °C, $T_{sh} = 1$ K, and $\omega = 1800$ rpm the Pareto Fronts for constant isentropic and volumetric compressor efficiency ($\eta_{is} = \eta_v = 0.7$) and variable efficiencies correlated for four semi-hermitic compressors from the literature ([23], [49], [50], and [51]). The compressor isentropic and volumetric efficiency correlations have a significant effect on the Pareto Front as shown. The isentropic efficiency affects the compressor outlet enthalpy, which in turn changes the enthalpy difference across the compressor affecting COP. The volumetric efficiency affects the mass flow rate, which changes $\dot{Q}_c$ and in turn also COP.

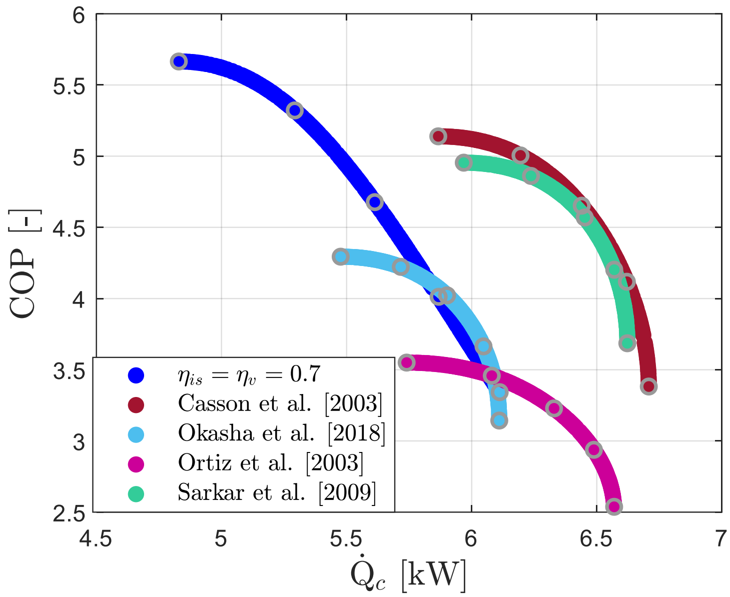

Figure 4-18. Pareto Fronts for maximizing both COP and $\dot{Q}_c$ at T_3=32 °C, T_1=15 °C, T_{sh}=1 K, and ω=1800 RPM, for different compressors efficiencies

4.4 Operation Contour Maps and Cycle Control Strategy

A set of Pareto Fronts can be generated offline covering all the possible operating ranges of T_3 and T_1. Each Pareto Front is generated by fixing each of these both variables to cover all possible operating condition combinations. Resulting from this, Figure 4-19 shows for the entire operation space of T_1 and T_3 at $\omega = 1800$ rpm for three selected values of the optimization parameter (k= 0 maximum COP solution, k=0.5 trade-off solution, and k=1 maximum $\dot{Q}_c$ solution) the contour maps of the reference GC pressure for the controller, and the resulting $\dot{Q}_c$, and COP. The GC pressure contour is omitted for k=1 as for such case the optimum pressure is always the maximum allowed GC pressure of 140 bar.

A sample system control block diagram is shown in Figure 4-20. Based on the input of measured T_3 and T_1, and corresponding with a predefined preference, i.e., a k value (for maximum COP, maximum $\dot{Q}_c$, or a trade-off solution), the optimizer retrieves the Pareto Front, and feeds the corresponding reference p_{GC} and T_{sh} for achieving the desired system behavior. The controller compares the reference signals to the actual measured ones, calculates the error, and acts accordingly based on the implemented control approach. The control approach can include that to avoid compressor on-off cycling at low load, the GC pressure is reduced below the one for maximum COP (k=0) to operate at reduced $\dot{Q}_c$ at a point where $\dot{Q}_c$ and COP are non-conflicting. As shown in Figure 4-20, an optional online optimizer can be integrated in the loop e.g. before the controller, resulting in conjunction with the offline optimizer in a hybrid solution. Such a hybrid solution can reduce the time to approach the desired operating point compared to online only methods. Compared to offline only methods, this can additionally enhance COP and $\dot{Q}_c$ based on the actual system characteristics, while it is also able to adapt to changing system characteristics.

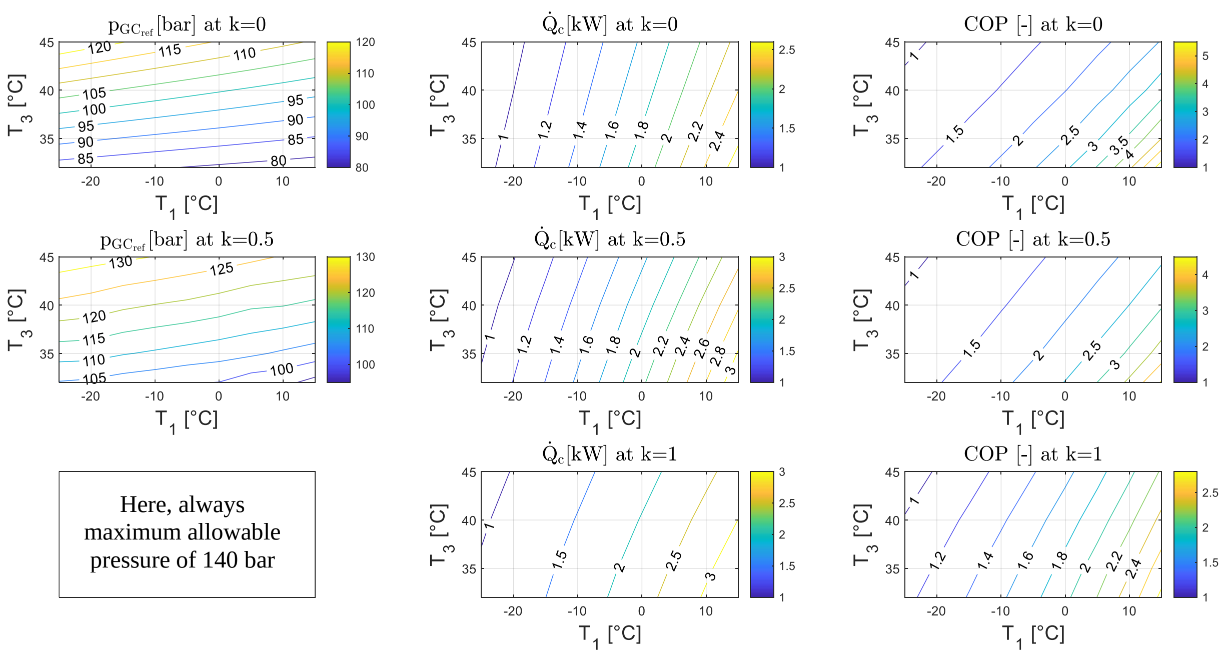

Figure 4-19. Operation Maps that show the contour lines of the GC pressures for T_1:-25 °C to 15 °C, T_3: 32 °C to 45 °C, and k=0 maximum COP (first row), k=0.5 trade-off (middle row), and k=1 maximum $\dot{Q}_c$ (last row)

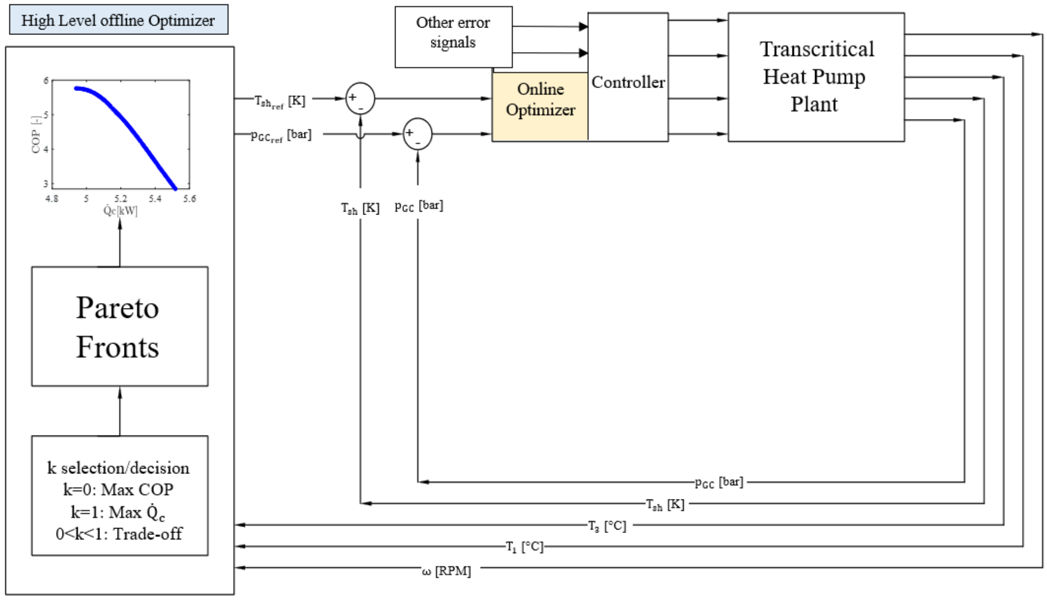

Figure 4-20. Transcritical cycle control block diagram for operating at the maximum COP, $\dot{Q}_c$, or a desired best trade-off both represented by Pareto Fronts

This chapter investigated the transcritical CO_2 vapor compression heat pump system from the perspective of maximizing both the COP and the cooling or heating capacity utilizing Pareto Fronts here generated with the NSGA-II algorithm, where each solution on a Pareto Front is designated by an optimization parameter k and corresponds to a particular gas cooler pressure and superheat. A gain to loss ratio for the Pareto Front solutions is presented that can be used as a criteria for moving from one solution to another. The effect of each optimization variable on the Pareto Front is shown separately. The gas cooler outlet temperature, the evaporation temperature, the compressor speed, and the compressor performance have significant effect on the Pareto Fronts compared to the superheat. A control methodology is introduced where the reference GC pressure and superheat corresponding to the maximum COP, cooling capacity, or a best trade-off solution between both as desired is retrieved from pre-generated Pareto Fronts that cover the expected operating condition ranges. The proposed methodology can be used for simple or modified cycle configurations, for cooling and heating application, for off-line, online, and hybrid solutions.

Chapter 5: Experimental Apparatus

This chapter presents the details of selecting the different components of the CO_2 transcritical experimental test-rig and presents the schematics, sizing equations, technical specifications, layouts, 3D CAD design of both the CO_2, and the HTF loops. In addition, we present the experimental test-rig build details.

5.1 CO_2 Loops

5.1.1 Schematics

The cycle schematics have been developed to allow investigations of cooling, heating, and dehumidification modes. The HTF loops are not shown in these schematics for simplicity and will be presented separately in the HTF loops section.

The cooling mode is shown in Figure 5-1 where low pressure and temperature vapor CO_2 enters the compressor and leaves as high pressure and temperature. The refrigerant enters the oil separator so that the oil is returned to the compressor through the oil charge plug. Refrigerant is then directed by a 3-way valve to pass along the OHX coils that act as a GC or condenser depending whether the heat rejection is above or below the critical point respectively. The refrigerant leaves the OHX and is directed by another 3-way valve to expand through the cooling expansion device before entering the evaporator coils. The accumulator then receives any liquid refrigerant to ensure that the compressor suction is getting vapor refrigerant only and minimal oil content.

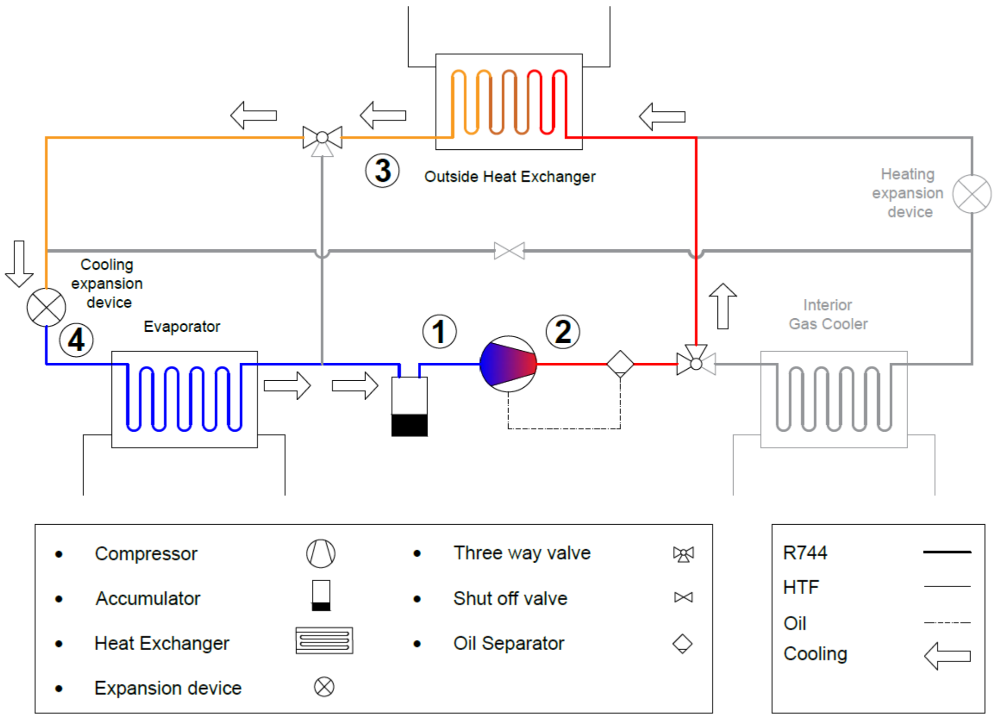

Figure 5-1. Cooling mode schematic

Figure 5-2 presents the schematic of the heating mode where the vapor CO_2, after passing by the compressor and oil separator, is directed by a 3-way valve to pass along the interior GC HEX coils, noting that this HEX will act as a condenser if the heat rejection occurs below the critical point. The refrigerant then expands through the heating expansion device before exchanging heat with the HTF through the OHX coils that acts as an evaporator. The liquid refrigerant is separated from the vapor refrigerant in the accumulator before the vapor flows again into the compressor.

The dehumidification series mode shown in Figure 5-3 resembles the heating mode up to the point where the refrigerant leaves the OHX, then a 3-way valve directs the flow to expand through the cooling expansion device; after which, CO_2 evaporates and the vapor refrigerant flow through the compressor. In this mode the refrigerant is sent to circulate through the three heat exchangers. Also, in this mode the refrigerant evaporates in a series fashion through the OHX and evaporator coils. In an automotive air conditioning system, and as reported in [52], the air will be cooled and dehumidified by the evaporator to the degree required for demisting the windshield before being reheated by the interior GC and blown into the cabin.

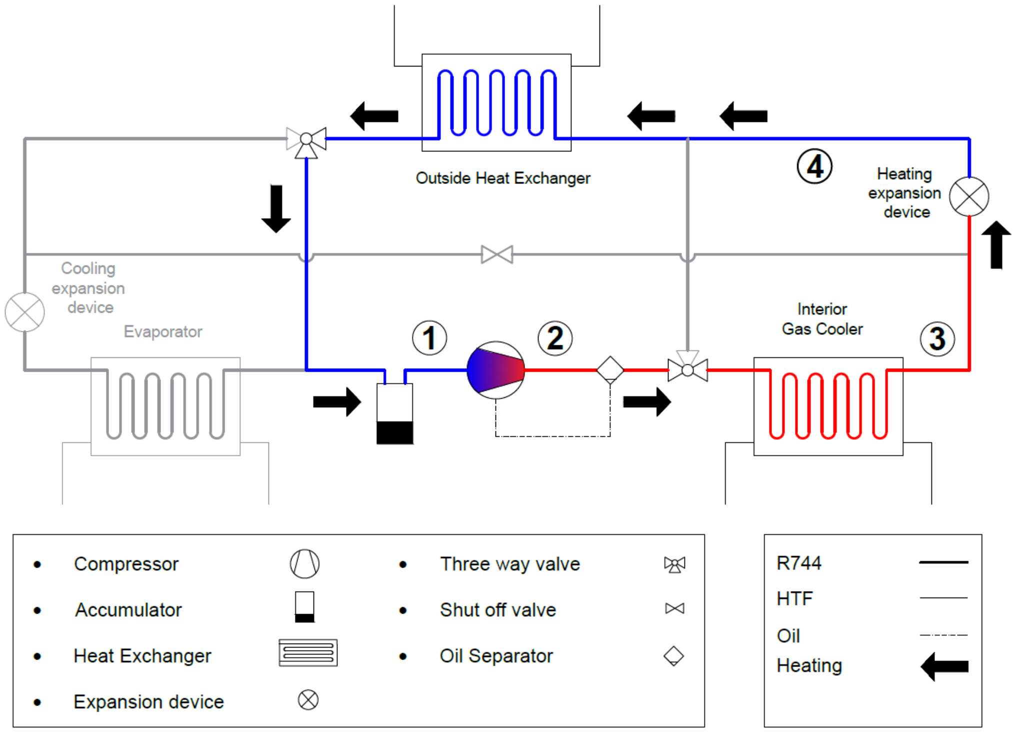

Figure 5-2. Heating mode schematic

Figure 5-4 shows the dehumidification parallel mode, which resembles the heating mode up to the exit of the interior GC. In this mode, the shut-off valve located in the center of the schematics is fully open, while in all other previous mode, this valve was fully closed. CO_2 is divided according to the percentage opening of the cooling and heating expansion devices. One portion expands through the heating expansion device before circulating through the OHX and being directed by a 3-way valve to the accumulator. The other portion passes through the shut-off valve before expanding through the cooling expansion device and evaporating. The two portions combine again at the intersection connection before the accumulator, and the refrigerant is sent to the compressor. A schematic that presents all the modes is shown in Figure 5-5.

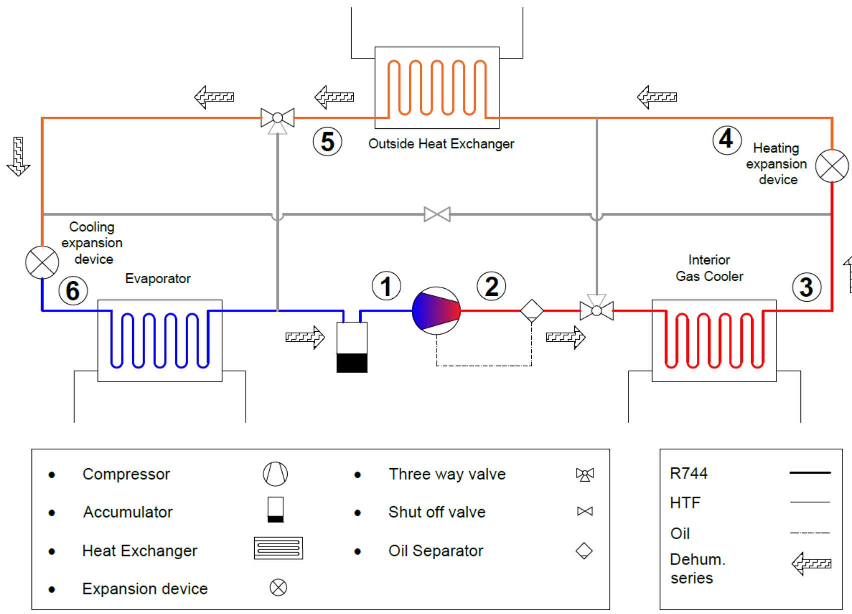

Figure 5-3. Series dehumidification mode schematic

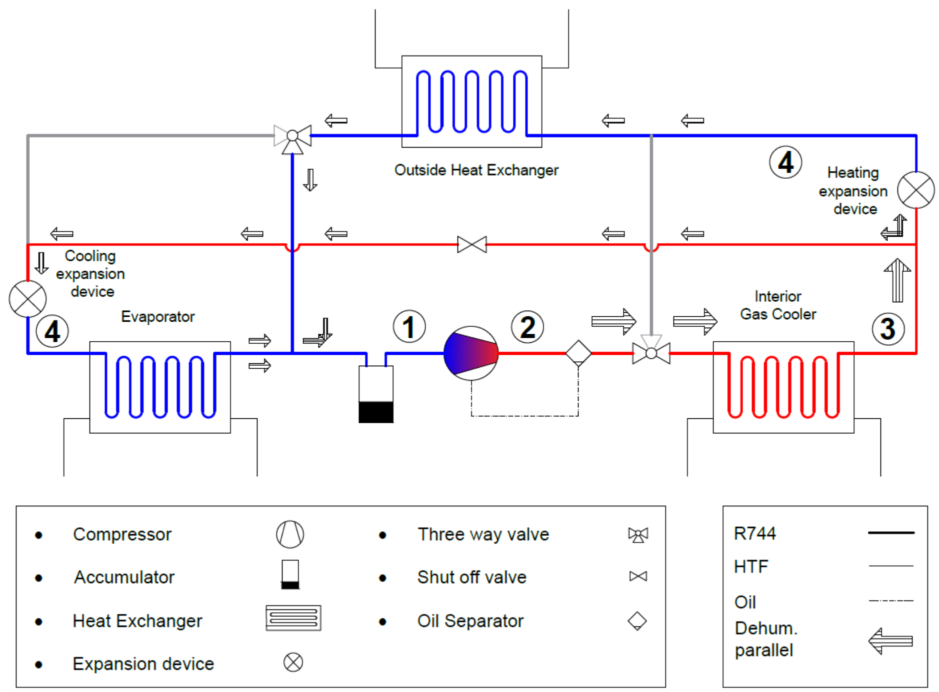

Figure 5-4. Parallel dehumidification mode schematic

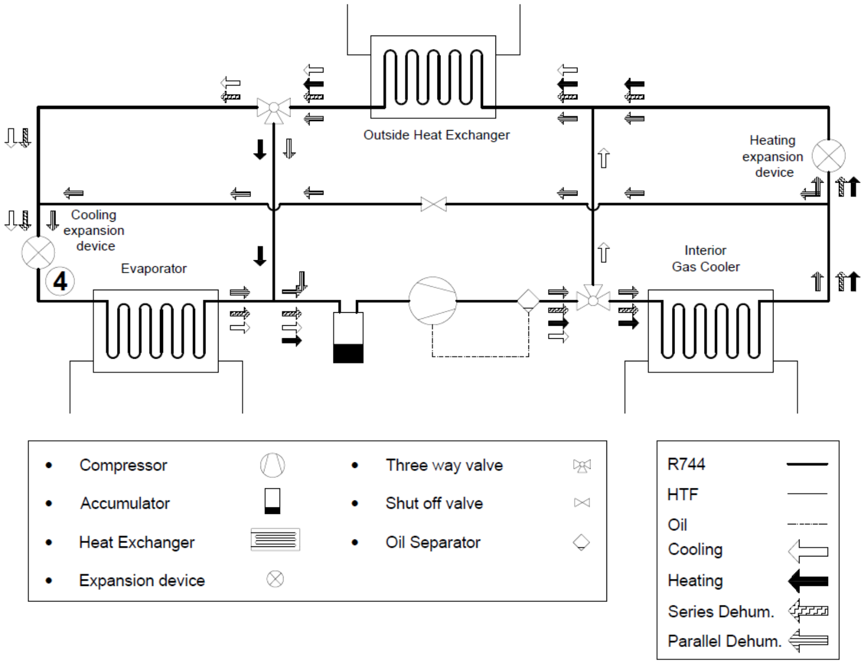

Figure 5-5. Cooling, heating, dehumidification series mode, and dehumidification parallel mode

5.1.2 Compressor

A compressor is required that shall provide enough cooling and heating capacities for a midsize vehicle. For such a vehicle, the range of required cooling and heating capacities are from 3 to 5 kW and 5 to 8 kW respectively. Another requirement for the heating mode is the capability to support ambient temperatures down to -30 °C. Thus, a compressor that supports evaporation temperature down to -30 or even lower is required.

Several manufacturers entered the market of CO_2 compressors with the most common types being semi-hermetic and rotary compressors. A survey has been carried out to find and compare different types of CO_2 semi-hermetic compressors. The compressor selected for this study is a Dorin CD200 - CD180H, 3 phase, 230V, and 60 Hz. The compressor's rated input power is 1.34 kW. Additional specifications are shown in Table 5-1. Based on simulating different data points in Dorin software, the compressor can provide maximum cooling and heating capacities of 5.5 and 8 kW respectively.

Most of the other available compressors provide capacities more than this; thus, they were oversized for our application.

Table 5-1. Compressor specifications

Specification	Value
Bore	22 mm
Stroke	17 mm
Swept volume (V_d)	$12.9/10^6$ m^3
Displacement	1.35 m^3/h @ 60 Hz
Speed	1740 rpm @ 60 Hz
Max low-side pressure	100 bar
Max high-side pressure	150 bar

The Dorin CD200 category has a splashing disc lubrication mechanism. In this lubrication method, the crankcase, which acts as an oil sump, is filled with oil to a certain level. As the crank shaft rotates, the connecting rod and crankshaft dip into the oil sump causing the oil to be splashed on the rubbing surfaces.

The motor driving the compressor is an asynchronous 4-poles motor. A small, electric heater immersed in the crankcase oil is often used to maintain adequate oil temperatures. The rated speed at 60 Hz is 1740 rpm. According to email communications with Dorin Corporation, The CD200 compressors can run from 60 down to 30 Hz. However, between 40 and 30 Hz, a resonance may appear. For this reason, Dorin recommends checking the compressor behavior in the whole range of speeds and in the case of a resonance problem, it is recommending skipping these frequencies. They also recommend always keeping the voltage to frequency ratio constant even when the speed is reduced.

A Hitachi WJ200 variable frequency drive is attached to drive the compressor to control the frequency (and hence, the speed). The compressor schematic and photo are shown in Figure 5-6.

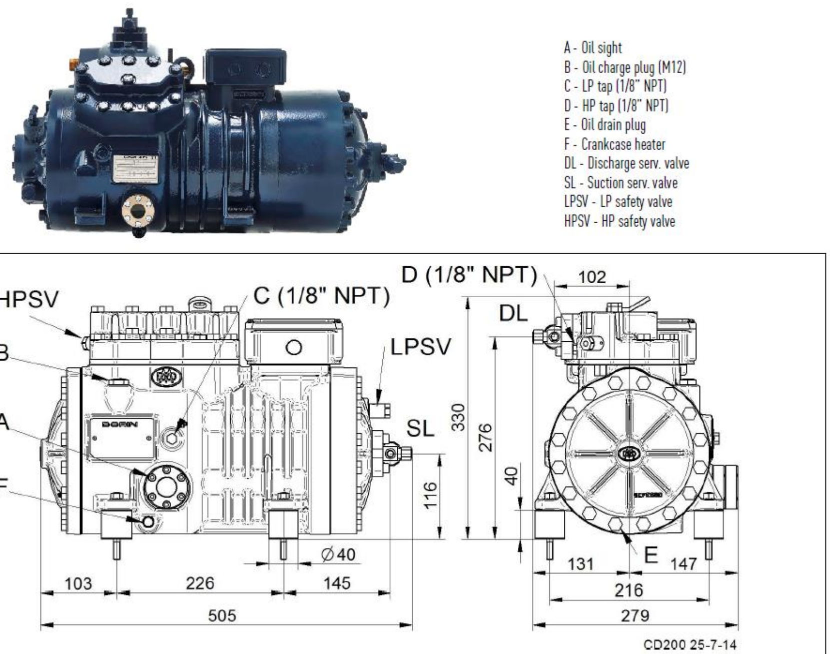

Figure 5-6. Dorin CO_2 CD180H compressor detailed drawing and photo (Credit: Dorin)

5.1.3 Oil Management

Since the compressor does not have an integrated oil separator; an oil management scheme is considered. The purpose of the oil separator is ensuring that the refrigerant circulating in the system is oil free. In such a system, the measurement of the temperature and pressure determines the enthalpy at each state point. If there is oil circulating in the system, it will affect the measurement accuracy. An oil separator from Temprite, Model 131 coalescent filter type, is installed at the compressor discharge that returns oil to the compressor charge plug. The oil separator photo and schematic are shown in Figure 5-7. The oil separator is rated up to 160 bar and is equipped with 3/8-inch female NPT connection for the three ports: the vapor inlet, vapor outlet, and oil outlet. The oil separator has also two 3/4-inch ports for the installation of two eye-sight glasses provided by PresSure Products Company (PPC), one at the bottom and the other one at the level of the oil vapor outlet port.

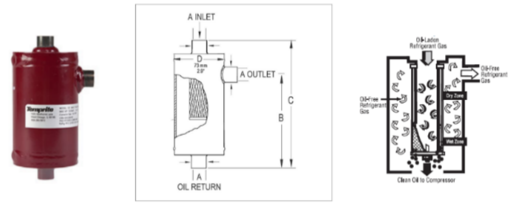

Figure 5-7. Oil separator photo and schematic (Credit: Temprite)

To control the oil return line, a sensor from HB Products Company is installed just below the oil outlet of the oil separator. The sensor shown in Figure 5-8 communicates with a solenoid valve at the return line to open/close if there is oil accumulated seen by the sensor or not. According to Dorin, the oil injected to the compressor charge plug shall be at a pressure that is between 5 bar and 10 bar higher than the crankcase pressure. The crank case pressure is the same as the low-side pressure. For that reason, a needle valve that can withstand high pressure is placed after the solenoid valve to reduce the oil pressure. The oil return line schematic is shown in Figure 5-9.

(a) (b) (c)

Figure 5-8. (a) HBOC (b) Installation on the compressor sight glass. (c) Solenoid valve V150 (Credit: HB Products Company)

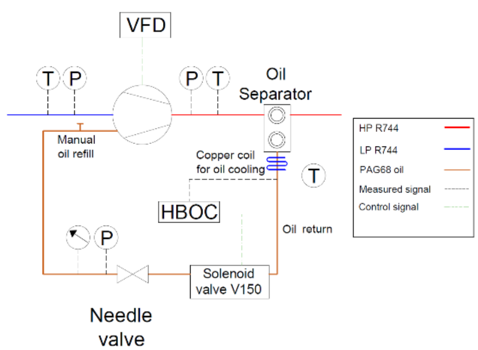

Figure 5-9. Schematic of the oil return line

5.1.4 Heat Exchangers

Three heat exchangers are needed for this study as the schematics showed: An outside heat exchanger that will act as an evaporator in the heating mode or as a GC/condenser in the cooling mode, a GC/condenser for the heating mode, an evaporator for the cooling mode. Brazed plate heat exchangers (BPHE) were a favored selection due to their compactness, low volume, and compatibility with CO_2. BPHE consists of cascaded corrugated stainless-steel plates that are brazed together using materials such as copper and nickel. The standard BPHE units are built from AISI316 steel with copper as a brazing material. Nickel is used as brazing material in applications where copper presents compatibility problems with process fluids. Each plate has a characteristic corrugation pattern that governs the degree of thermal efficiency and hydraulic behavior of the BPHE unit.

The operating conditions of each heat exchanger were given to Alfa Laval Company which included the maximum capacity, its associated refrigerant and HTF inlet and outlet temperatures, pressures, and flow rates. The recommended BPHE was AXP10-20H-F where "20" is the number of plates, "H" is the type of plate, and "F" means 316 stainless. The brazing material is copper. This unit has temperatures that range from -196 °C to 225 °C. The pressure rating and a schematic showing the dimensions of the AXP unit are shown in Figure 5-10.

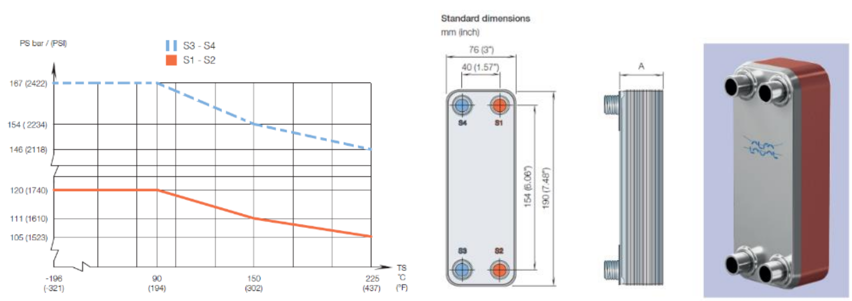

Figure 5-10. AXP10 Pressure ratings (Left) and AXP10 Photo and Schematic (right)

5.1.5 Suction Line Accumulator

As reported in [53], the standard rotational speeds of compressors are between 1,725 and 3,400 rpm. At these speeds, if any liquid enters the compressor chamber, it can cause instantaneous mechanical failures. A condition known as slugging occurs when a large amount of liquid refrigerant is entrained with the vapor refrigerant. Slugging is accompanied by pounding and knocking sounds and frequently causes instantaneous compressor damage. Even if the liquid refrigerant returns to the compressor in small quantities (but over a long period of time), this liquid refrigerant tends to dilute the oil, reducing its lubricity and generating a condition of rapid bearing wear. Suction line accumulators help protect compressors against either immediate or long-range damage caused by the return of liquid refrigerant to the compressor.

Accumulators are vessels that can be vertical or horizontal. Vertical accumulators use a U or J tube to draw gaseous refrigerant off the top of the vessel. Most accumulators have at the bottom of this tube, a small orifice to pick up a small amount of oil and liquid refrigerant and meters it back with the gaseous refrigerant. This small amount of liquid refrigerant will boil off in the suction line. The oil will be carried with the gaseous refrigerant back to the compressors.

Two considerations were important while sizing the accumulator. First, the accumulator shall be able to hold the system's liquid refrigerant. Normally, the accumulator liquid-holding capacity shall not be less than 50% of the system charge [54]. Second, the accumulator shall perform without adding excessive pressure drop into the system.

If the accumulator is sized too big to handle the system capacity (The system capacity is smaller than the accumulator minimum capacity.), the orifice will not meter back oil due to the reduced flow through the accumulator. The accumulator needs to be selected to ensure that the system capacity is above the minimum rating. If the accumulator is sized too small to handle the system capacity (The system capacity is larger than the accumulator maximum capacity.), this problem will cause the orifice to meter back more refrigerant (which may contain liquid refrigerant) due to the increased gas flow past the orifice.

An accumulator volume of 2.7 L was calculated based on the estimated system volume. A horizontal design was proposed and sent to Temprite for quoting and manufacturing. Figure 5-11 shows the current 3D design of a horizontal accumulator, which encompasses a sight glass and oil outlet that can be utilized for oil removal that may be accumulated in the accumulator. The accumulator is designed horizontally for compactness purposes of the test-rig. The accumulator is equipped with a heat exchanger to cool down the refrigerant coming out of the GC just prior to the expansion process.

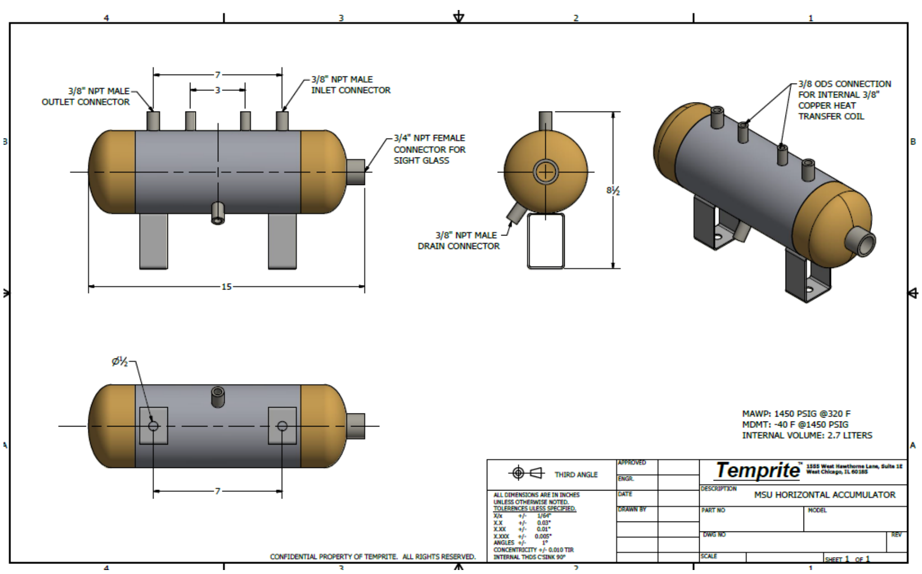

Figure 5-11. Horizontal accumulator design drew by Temprite

5.1.6 Expansion Device

A Swagelok SS-31RS4 manual metering valve is selected that has a maximum pressure of 193 bar at 454 °C and a temperature range of -53 °C to 454 °C. A schematic photo of the manual metering valve and its C_v graph is shown in Figure 5-12. Since the expansion device encompass two-phase flow, calculation of the C_v is involved. The calculation of C_v was carried out by using Eqn. (5.1), which is primarily used for liquid flow. Using this equation may introduce deviations as CO_2 is in a supercritical state at the valve inlet, but the equation is still valid for a good approximate value as pointed and used in [22] in their CO_2 transcritical experimental facility. The estimated C_v value for the maximum capacity case (and hence maximum mass flow rate case) was less than 0.04.

$$C_v = q\sqrt{\frac{SG}{\Delta P}} \text{ ,where q is in GPM} \tag{5.1}$$

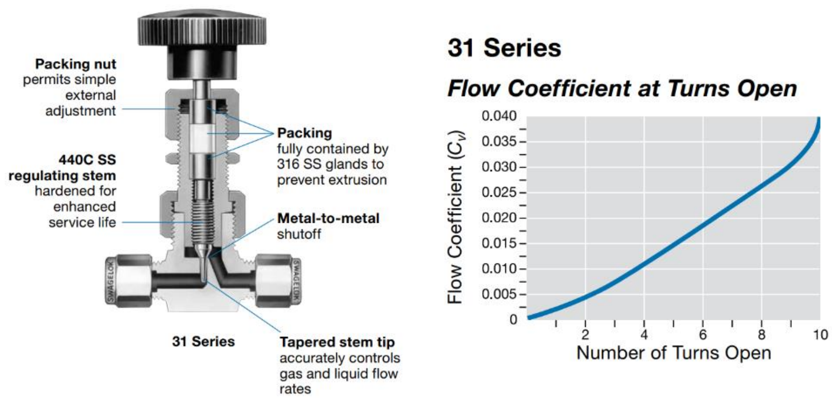

Figure 5-12. Schematic of SWAGELOK 31 series valve and it Cv graph

5.1.7 Pressure Drop

For the system to operate efficiently, pressure drop calculations are considered to find the optimum refrigerant tube size that would not produce considerable pressure drop and affect the cooling/heating capacities. The tube sizing is carried out for the suction, discharge, and liquid lines. After extracting the mass flow rate ($\dot{m}$) and the density (ρ) from test conditions simulations for the maximum capacity cases, a code was written in MATLAB to calculate the total pressure drop, which is the sum of tubing friction losses ΔP_F, fitting losses ΔP_L, elevation difference pressure drop/gain $\pm\Delta P_Z$, valves, and other elements pressure drops.

Friction losses are the losses of pressure that occur in the pipe or duct flow because of the fluid's viscosity near the surface of the pipe or duct. The Darcy Weisbach equation [55] relates the pressure loss due to friction along a given length of pipe to the average velocity of the fluid flow for an incompressible fluid as

$$\Delta P_F = f_D . \frac{\rho}{2} . \frac{v^2}{D_{inside}} . L \tag{5.2}$$

The flow speed is determined by

$$v = \frac{\dot{m}}{\rho A} \tag{5.3}$$

where A is the internal cross-sectional area. Reynold number is defined by

$$Re = \frac{\rho v D_{inside}}{\mu} \tag{5.4}$$

The Darcy friction factor f_D is usually calculated from the Moody friction factor chart [56]. The chart is made from the following equations [57]. For laminar flow with Re ≤ 2100, the Hagen-Poiseuille equation [57] gives

$$f_D = \frac{64}{Re} \tag{5.5}$$

For transitional flow where the friction factor varies with both Re and K, the Colebrook equation [58] is used

$$\frac{1}{\sqrt{f_D}} = -2log(\frac{\epsilon}{3.7D_{inside}} + \frac{2.51}{Re * \sqrt{f_D}}) \tag{5.6}$$

where the stainless-steel absolute roughness coefficient is ϵ=0.015 [59]. The Colebrook equation is also found to cover the fully developed flow regions for smooth and rough pipes as reported in [60]. We used this equation instead of the Moody chart as it can be handled easier using a computer. However, f_D is not implicitly expressed in the equation; therefore, it needs a numeric calculation. We used a function written in MATLAB that calculates f_D using the method of quadratic iteration [60], which is valid for Re ≥ 2300. The function takes Re and the relative roughness coefficient ($K = \epsilon / D_{inside}$) as inputs and generates f_D.

Several methods are available to calculate the fittings' pressure drop. For fittings such as 90-degree bends, the geometry of the fitting has a greater impact on the pressure loss than does an equivalently sized length of pipe. The best case for determining the loss in a fitting would be to use experimental data; however, this is often not available.

The equivalent length method is the oldest and most common one [61] [62], which treats the fitting as a straight pipe with a specific length that depends on the geometry of the fitting. This length is generally larger than the arc length of the bend. This method does not take into consideration the Reynolds number and the pipe diameter.

Crane's method [63] is a modification of the equivalent length method, which takes into consideration the higher degree of turbulence in valves and fittings than in a pipe with a given Reynolds number.

The loss coefficient method estimates the pressure drop in a fitting through a loss coefficient, K, determined by experiments. Loss coefficients values are tabulated, but these values are constant regardless of the pipe components geometry (diameter, elbow radius, type of pipe connection, etc.) and Reynolds number [64].

Belvin's method [65] depends on the velocity of the fluid and pipe diameter. The calculations are independent on the roughness of pipe and type of connection elbow.

The 2-K method [62], [66], and [67] is based on experimental data of valves, fittings, and elbows acquired for various Reynolds numbers. The K coefficient is a function of the Reynolds number, geometry of a given component, and the type of pipe connection for elbows. But it is not influenced by roughness. Clearly, the 2-K method is more accurate than the equivalent length method as it applies an additional constant to improve characterization of the fitting pressure drop with variation of the fluid Reynolds Number.

The 3-K method [67] is similar to the 2-K method but with a higher predicative value for the broad radius of Reynolds numbers and fittings dimensions [64]. The 3-K method is also dependent on elbow inner diameter and the value of Reynolds number.

In [64], the authors performed a simulation study comparison between the different methods listed above and the study reported that the 3-K method [67] is recommended for a calculation of the pressure drop of 90 degree elbows because it accounts directly for the effect of both Reynolds number and fitting size on the loss coefficient and reflects more accurately the scale effect of fitting size and connection type.

The 3-K method has been followed here to find the pressure drops for bends, union Tees, branching, sensor fittings, expansion areas, and contraction areas. The 3-K method depends on calculating the K factor according to the equation

$$K = \frac{K_1}{Re} + K_\infty(1 + \frac{K_d}{D_{outside}^{0.3}}) \tag{5.7}$$

where K_1, K_∞, and K_d are extracted from tables.

For a square reduction, if Re<2500

$$K = (1.2 + \frac{160}{Re})[(\frac{D_1}{D_2}^4) - 1] \tag{5.8}$$

where D_1 is the entrance diameter and D_2 is the exit diameter.

And for Re > 2500

$$K = (0.6 + 0.48f_D)(\frac{D_1}{D_2})^2[(\frac{D_1}{D_2}^4) - 1] \tag{5.9}$$

For a square expansion, if Re < 4000

$$K = 2[1 - (\frac{D_1}{D_2}^4)] \tag{5.10}$$

where D_1 is the entrance diameter and D_2 is the exit diameter.

And for Re > 4000

$$K = (1 + 0.8f_D)(1 - \frac{D_1}{D_2})^2)^2[(\frac{D_1}{D_2}^4) - 1] \tag{5.11}$$

The fitting losses can then be calculated by

$$\Delta P_L = \rho g K \frac{v^2}{2g} \tag{5.12}$$

As fluid flows through a piping system, where pipes rise and fall and change elevation, the pressure at a point in a pipe is also affected by the changes in elevation of the fluid that have occurred. The net change in elevation h_z is calculated, for instance for the suction line from the evaporator outlet to the compressor inlet. The pressure drop/gain is expressed as

$$\Delta P_z = \pm \rho g h_z \tag{5.13}$$

For valves, a valve has a C_v of 1 when a pressure of 1 psi causes a flow of 1 US gallon per minute of water at 60 °F (i.e. SG = 1) through the valve. Since the pressure drop through a valve is proportional to the square of the flow rate the relationship between C_v, flow rate and pressure drop can be expressed as

$$q = C_v sqrt \frac{\Delta P_{valve}}{SG} \tag{5.14}$$

Therefore, the valve pressure drop can be expressed as

$$\Delta P_{valve} = SG(\frac{q}{C_v})^2 \tag{5.15}$$

The flow sensor used in CO_2 loop is Micro Motion F-Series Coriolis flow meter. The pressure drop across the flow meter is obtained as a function of the flow rate from Emerson.

For the oil separator, our talks with Temprite revealed that the estimated pressure drop across the 131 model is around 1.5 psi. Apparently, this pressure drop increases if the filter gets contaminated. A constant pressure drop of 5 psi is assumed during these calculations. For the accumulator, the nominal pressure drop across accumulator may not exceed 0.3 bar, as reported online. Hence, for this study, that was the assumption.

A MATLAB code has been developed to calculate the total pressure drop in the suction, discharge, and liquid lines of the cooling mode considering tube sizes of 1/4, 3/8 and 1/2-inch. After calculating the pressure drop, the equivalent temperature drop in Fahrenheit is calculated by assuming constant enthalpy. For such refrigeration systems, the pressure drop should not produce more than 2 °F in the suction line and 1 °F in each of the discharge and liquid line [68]. Figure 5-13, Figure 5-14 , and Figure 5-15 show the pressure drop in bar, temperature drop in Fahrenheit, and the flow velocity in m/s for the different tube OD diameters, for the suction, liquid, and discharge lines respectively.

As shown in the graphs, for 3/8-inch OD, the temperature change due to the pressure drop is less than 2 °F in the suction line and less than 1 °F in both discharge and liquid lines. The flow velocity for this case is acceptable (not very small and not very high flow velocity). Based on this analysis, all the tubes have been selected with a 3/8-inch OD and a wall thickness of 0.049 inch.

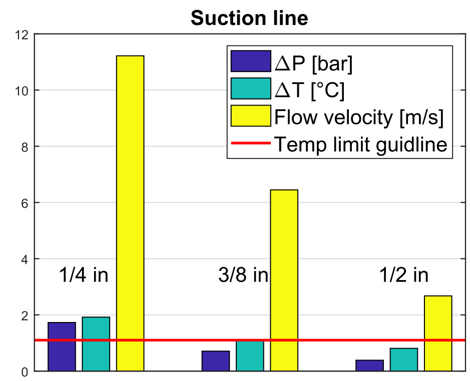

Figure 5-13. Suction line Pressure drop, equivalent temperature change, and the flow velocity for different tube OD

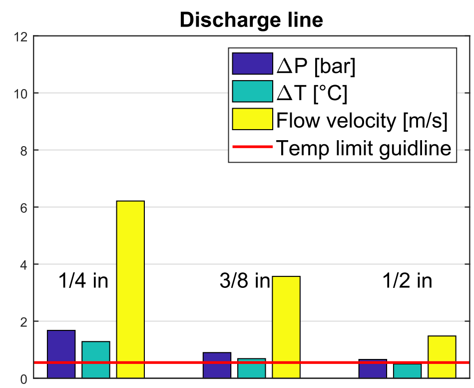

Figure 5-14. Discharge line Pressure drop, equivalent temperature change, and the flow velocity for different tube OD

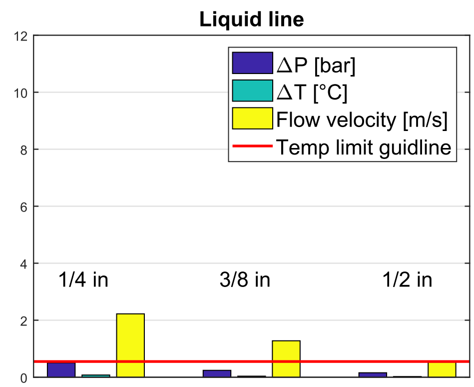

Figure 5-15. Liquid line Pressure drop, equivalent temperature change, and the flow velocity for different tube OD

5.1.8 *Valves, Tubing, and Fittings*

Different types of valves are needed in the CO_2 loops for isolation, filling, discharging, and routing the flow. The selection of valves mainly depends on the application, temperature range, pressure range, and the valve flow coefficient, which varies with the valve size, hence, also the valve end connection size. The reported leak rate of the valves is also checked to make sure that no considerable leakage will take place in the system.

Most of the available valves in the market do not cover the whole temperature range of the CO_2 in the loop from -40 °C to 160 °C. The low end is -40 °C because the compressor supports evaporation temperatures down to -30 °C; hence, 10 °C is considered a good extra margin. The high-end 160 °C is estimated from running various simulated data points and observing the highest compressor discharge temperature, which was around 150 °C; and 10 °C is also considered as a safety factor. The maximum high-side and low-side pressure is 140 and 100 bar respectively, which is rated from the compressor data sheet. Since the CO_2 loop supports cooling, heating, and dehumidification modes, the location that is identified as the high temperature and pressure for one mode may also be identified as the low temperature and pressure in another mode. Hence, for each of the four modes, valves are identified and selected according to the location into which they will be placed in the loop, i.e., that can support working in all modes.

For locations that will be exposed to high temperature, the 3-way valve SS-83XPS6 with PEEK seats is selected because it covers a temperature range from -17 °C to 232 °C. The valve has a C_v value of 0.75. For locations that will be exposed to low temperature, the 2-way and 3-way valves SS-43GS6 and SS-43GXS6 respectively, which cover from -53 °C to 148 °C, are selected. The 2-way valve has a C_v value of 1.5, while the 3-way valve has a C_v value of 0.9. Only one location in the loop that will see both high and low temperature depending on which mode is operating, which is the location just before the OHEX. This location has two 2-way valves to control whether the flow enters the HEX from the top or bottom. If the HEX acts as evaporator, refrigerant will enter from the bottom. If the HEX acts as condenser, refrigerant will enter from the top. These two valves are chosen as a needle valve SS-6NBS6 that has a temperature range -53 °C to 648 °C. The needle valve has a C_v value of 0.86. Although, a needle valve is usually used as a regulating valve, it can also be used as a shut-off valve as confirmed by Swagelok. The maximum pressure rating of all valves varies with the temperature as reported in the tables in the datasheets. All the valves chosen to have been checked to have pressure rating suitable for the valve location.

All the above valves as reported by Swagelok have a maximum allowable leak rate of 0.1 std cm^3/min under tests with nitrogen at 69 bar. This leak rate, 0.1 std cm^3/min, represents 4 ppm (or 0.0004%) of our maximum expected CO_2 flow rate (150 kg/h corresponds to 24000 std cm^3/min, at 100 kg/m^3 CO_2 vapor density). If we consider a 1 m/s flow speed in a 3/8" line with 0.049" wall thickness, we get 1/10 of this with ≈ 0.00004 m^3/s for 1 m/s, putting the leakage at ≈ 40 ppm ≈ 0.004%. Furthermore, we may consider that the leak testing is done at only 69 bar, so we could double the result (considering that our maximum pressure is 140 bar) putting it at ≈ 0.01%. However, 1 m/s may not be the lowest relevant flow condition. If we assume operating in the range of 10% to 100% capacity, this puts the leak to 0.1% at 100% capacity. 0.1% leakage is still a relative low number. So, this seems to be acceptable for practical operational tests and investigations as this leakage is within the system and not connected to the ambient. When these valves used in places that will be exposed to the ambient such as the charging valve, the valve outlet is capped to ensure ambient outlet end leak tight.

All the tubing used are Swagelok, 316/316L SSL Seamless, 3/8-inch OD and 0.049-inch wall thickness. The tubing and fittings are rated up to 4800 psi (330 bar). The temperature rating reported in the data sheet is from -28 °F to 37 °F. The fittings are 316 SSL which is rated to the same temperature and pressure rating of the tubing. After several talks with Swagelok technical team, they confirmed that there are customers who used these tubing and fittings in much more extended temperature range application; hence, they confirmed that these tubing and fittings will work for our application range from -40 °C to 200 °C.

5.2 HTF loops

The purpose of the heat transfer loops is to provide the needed cooling and heating capacities for each HEX. The CO_2 cycle design needs to reflect conditions where the CO_2 refrigerant temperature is at -30 °C, which is the compressor's lowest evaporation temperature. At this operating condition, CO_2 will be able to pick up heat from -30 °C temperature or less from the environment. Providing HTF with a temperature of -30 °C or lower will enable us to reflect the environmental conditions of an automotive in the winter. For that reason, a chiller with sufficient capacity of -30 °C is required to be able to reach that goal.

5.2.1 Steady-state Capacities

As depicted from the compressor simulations, the maximum and minimum cooling capacity is 5.5 kW and 0.5 kW respectively, while the maximum and minimum heating capacity is 8.0 kW and 1.5 kW respectively. The capacities can be translated to express the maximum capacity of each HEX in each mode as follows: the maximum evaporator capacity is 5.5 kW, the maximum outside HEX capacity is 8.0 kW, and the maximum interior GC capacity is 8.0 kW.

For the cooling mode steady-state operation, since the maximum evaporator capacity is 5.5 kW, it can be assumed that the maximum heater capacity for the evaporator in the cooling mode is 6.0 kW to account for neglected heat losses. For the OHEX that will act as a condenser/GC mode with a maximum capacity of 8.0 kW, we can assume that the maximum needed chilling capacity for the

OHEX in the cooling mode is 10.0 kW (assuming 2 kW of external heater control for desired temperature set-point, fine tuning.) Figure 5-16 shows the cooling mode schematics with the first law of thermodynamics applied on the system.

Similarly, for the heating mode steady-state operation, since the maximum OHEX capacity (that will act as an evaporator) is 5.5 kW, it can be assumed that the maximum heater capacity for the OHEX in the heating mode is 6.0 kW. For the interior GC that has a maximum capacity of 8.0 kW, we can assume that the maximum needed chilling capacity for the OHEX in the heating mode is 10.0 kW. Figure 5-17 shows the heating mode schematics with the First Law of Thermodynamics applied on the system.

Hence, for steady-state operation a single chiller of 10 kW capacity or more is required that will cool either the interior GC or the OHEX and two heaters each of 6.0 kW capacity.

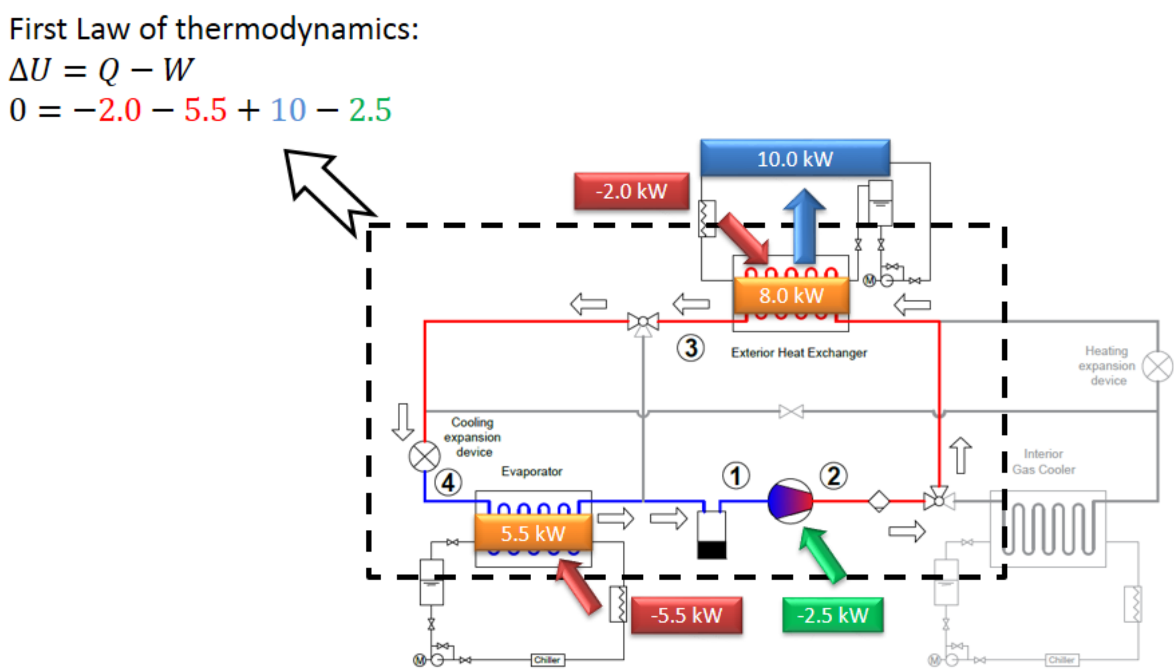

Figure 5-16. The First Law of Thermodynamics applied to the cooling mode to estimate the needed chilling and heating capacities

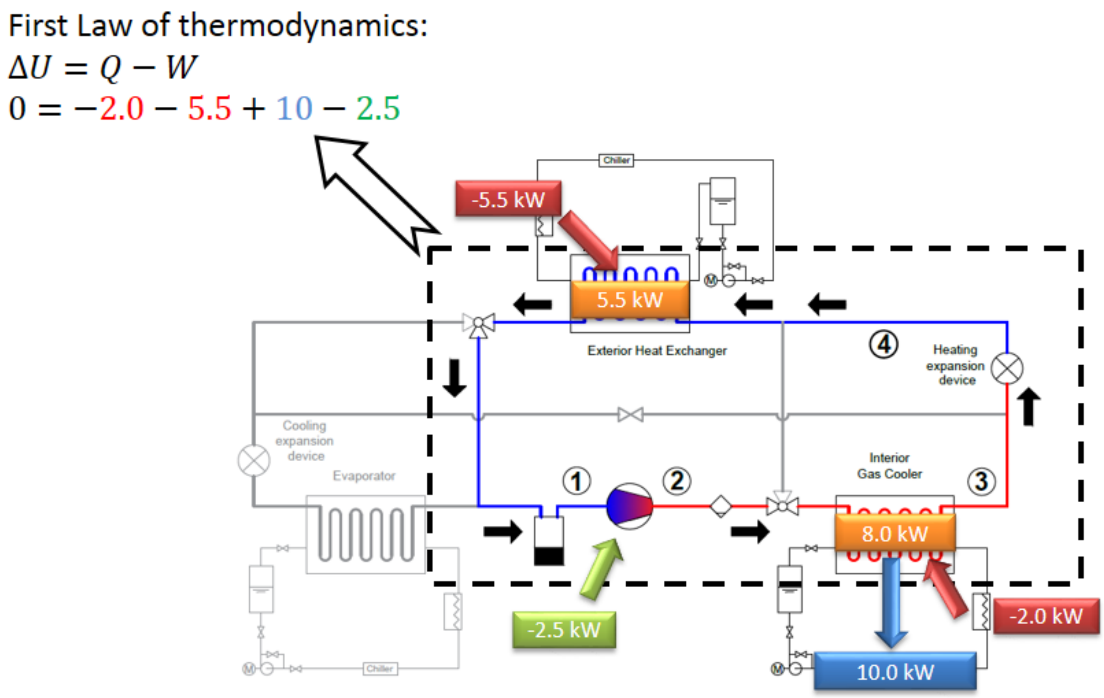

Figure 5-17. The First Law of thermodynamics applied to the heating mode to estimate the needed chilling and heating capacities

5.2.2 Tanks Sizing

Before looking at the transient testing needed capacities, an estimate of the tank size for each HTF cooling loop is obtained first. Chiller manufacturers recommend that 3-6 gallons is needed per ton of nominal cooling. This range extends to 6-10 gallons per ton for enough temperature control [69]. For the work considered here, we assume 8 gallons per ton of refrigeration. The actual system volume shall be subtracted from the required system volume. But since the HTF piping has a small diameter (around 1 inch as will be shown later) and consequently small volume compared to the tank's size, the piping volume can be neglected. The calculation is based on the maximum capacity for each HEX, which is stated one more time here: 5.5 kW for the evaporator, 8.0 kW for the OHEX, and 8.0 kW for the interior GC. Thus, the volume calculations for each HEX line/loop can be written as

$$V_{Evap-Tank} = 6kW * 0.28(\frac{ton}{kW}) * 8(\frac{gal}{ton}) = 13.4gal \Rightarrow V_{Evap-Tank} \simeq 15gal \quad (5.16)$$

$$V_{InteriorGC-Tank} = 9kW * 0.28(\frac{ton}{kW}) * 8(\frac{gal}{ton}) = 20.2gal \Rightarrow V_{InteriorGC-Tank} \simeq 20gal \quad (5.17)$$

$$V_{OutsideHEX-Tank} = 9kW * 0.28(\frac{ton}{kW}) * 8(\frac{gal}{ton}) = 20.2gal \Rightarrow V_{OutsideHEX-Tank} \simeq 20gal \quad (5.18)$$

For the sake of unification, all tank sizes will be considered the same size, thus

$$V_{Evap-Tank} = V_{InteriorGC-Tank} = V_{OutsideHEX-Tank} \simeq 20\ gallon \quad (5.19)$$

5.2.3 Transient Capacities

The objective of the transient testing is to prepare each HEX HTF inlet temperature to reflect various environmental conditions. The HTF is set so that the behavior and operation of the refrigerant cycle can be studied and investigated because it would reflect the operation of the heat pump cycle in hot and cold environmental conditions. Hence, this will allow the testing of the CO_2 cycle at different transient operating conditions. The evaporator and interior GC HTF inlet temperatures reflect the vehicle compartment temperature in summer and winter respectively, while the OHEX reflect the environment temperature. As the testing conditions revealed, for the cooling mode, the evaporator and the OHEX are both set from 25 °C to 45 °C. While for the heating mode, the OHEX is set from -30 °C to 10 °C, while the interior GC is set from -30 °C to 25 °C, considering that the vehicle compartment might be warmer than the environment. Thus, for all cases, the evaporator set range is from 25 °C to 45 °C, the interior GC will be set from -30 °C to 25 °C, while the OHEX will be set from -30 °C to 45 °C. Since the experiment is conducted in a lab environment, the HTF temperature is steered from the lab temperature to the desired set point. We assume that a hot day (in the summer) temperature in the lab is 35 °C, while a cold day (in the winter) in the lab is 15 °C. It is important to calculate the needed time to prepare the HTF from its initial temperature to any temperature that lies in each HEX set range. Calculating the time assures that heaters' and chillers' capacities obtained from the steady-state calculations are enough for the transient preparation. If the time obtained is found to be relatively long, that implies that the heater/chiller capacity need to be increased to accommodate the transient test preparation. The time is calculated from

$$Time = \frac{\rho V c_p \Delta T}{Q_{Heater/Chiller}} \tag{5.20}$$

where V is the tank volume and ΔT is the temperature difference between the HTF initial temperature (ideally the temperature of the lab environment) and the HTF required set point. ρ and c_p are calculated at the average temperature of the initial and set-point temperatures.

Heater capacities are checked for the test-rig operation either in the cooling or the heating mode. Table 5-2 shows the computed heater on-time for the evaporator and the OHEX for the cooling mode, if the HTF temperature is steered from 15 °C initial temperature to 45 °C set point. As shown, less than half an hour is required to reach the maximum desired temperature in a cold lab day, using the heater capacities obtained in the steady-state analysis. Thus, the heaters capacities are suitable for the transient testing as well. For the heating mode, the same procedure is followed as for the cooling mode. Since in the steady-state analysis, no heater was needed for the interior GC, the heater capacity of the interior GC will be assumed 6 kW as other selected heater capacities. The heater on-time needed from 15 °C to 25 °C with a heater capacity of 6 kW is only 8 min.

The chillers' capacities developed at the stead-state are also verified for test-rig operation in either the cooling or the heating mode for the transient operation. For the cooling mode, the minimum required temperature for transient testing is 25 °C for both the evaporator and the OHEX. If we assume a hot day in the summer where the lab temperature is 35 °C, a chiller is needed with a reasonable capacity to steer the HTF from 35 °C to 25 °C. From the steady-state analysis, the OHEX chiller capacity is shown to be 10 kW. If a chiller with this capacity is obtained, the maximum capacity is usually nominal at 20 °C, which means a close value to 10 kW at 25 °C. For the evaporator, the steady-state analysis did not need a chiller; hence, a chiller with appropriate capacity can be selected for the transient preparation. We assume a 1 kW chiller for the evaporator. In Table 5-3, the estimated time of cooling the HTF from 35 °C to 25 °C is shown. It can be concluded that a chiller capacity of 10 kW is more than enough for the OHEX, and a chiller capacity of 1 kW is suitable for the evaporator.

Table 5-2. Estimated HTF heater on-time for different heat exchangers in a cold day lab environment for preparation of the cooling mode

Heat Exchanger	$T_{initial}$ (°C)	T_{sp} (°C)	Heater Cap. (kW)	Time (min)
Evaporator	15	45	6	23
OHEX	15	45	6	23
Interior GC	15	25	6	8

Table 5-3. Estimated HTF Chiller on-time for different HEXs in a hot day lab environment for preparation of the heating mode

Heat Exchanger	$T_{initial}$ (°C)	T_{sp} (°C)	Heater Cap. (kW)	Time (min)
Evaporator	35	25	3.7 @ 20 °C	12
OHEX	32	-29	3.7 @ -29 °C	80
Interior GC	35	-29	3.7 @-29 °C	80

For the heating mode, the minimum required temperature for transient testing is -30 °C for both the OHEX and the interior GC. Thus, a chiller is needed with a reasonable capacity to steer the HTF from 35 °C to -30 °C. From the steady-state analysis, the interior GC chiller capacity is shown to be 10 kW. For the OHEX, the steady-state analysis of the cooling mode needed a chiller with capacity of 10 kW. However, if a chiller with a nominal capacity of 10 kW is obtained, the capacity at the lowest set point is usually less than this. A chiller is selected that has a capacity of 3.7 kW at -29 °C as will be discussed in the next subsection. To steer either the OHEX or the interior GC from 35 °C to -29 °C. This needs 80 minutes as shown in Table 5-3. If the pump chiller can drive two HEX lines at the same time, this time is doubled to become 160 minutes (less than three hours) to cool two HEXs with the same chiller. This increase to 4 hours if the chiller will cool three HEXs at the same time. This amount of time is not very long and, hence, considered acceptable. Thus, one chiller can be used to prepare the three heat exchangers if the pump can drive them.

Based on the above analysis, the required heater and chiller nominal capacities to support both steady-state and transient test conditions are as follows: Each heat exchanger needs a heater of 6 kW capacity. The three HEXs each needs a chiller of 10 kW nominal capacity and a capacity of around 3.5 kW at -29 °C to ensure that the time needed to prepare the HEXs is not very long.

5.2.4 Chillers and pumps Selection

Different chillers that can support the steady-state requirement can also support the transient conditions but with different chilling time. Choosing a chiller does not depend solely on the nominal capacity but also on the lowest set point temperature and how much capacity is at this set point. The chiller prices increase with lower set point and with increased capacity at the lowest set point. A survey has been carried out to compare different chillers available in the market in terms of these parameters. The chiller selected a high capacity, the Mokon ALT-2, with a capacity of up to 12,391 BTU/hr (≈3.63 kW) at -20 °F (≈ -29 °C), and 44,976 BTU/hr (≈13.2 kW) at 20 °F (≈ -6.5 °C), tested with 50/50% water/ethylene glycol ratio. The chiller has an air-cooled condensing unit. The chiller is equipped with 2 HP pump where its characteristic curve is shown in Figure 19 by the green thick line. The chiller has 9 kW heater. The chiller operating temperature range is from -20 °F (≈ -29 °C) to 20 °F (≈ 93 °C). The chiller photo is shown in Figure 5-18.

Figure 5-18. A photo of ALT-2 Mokon chiller

To assure that the chiller pump is suitable for our system flow and pressure drop, a MATLAB script code is written to calculate the system pressure drop at different flow rates. The 3-K method has also been followed here for pressure drop calculation for different fittings. The ethylene water glycol mixture thermodynamic properties are calculated based on experimental empirical data provided by Dow Chemical Company. A static head of 2 m is assumed because the HEXs are in a height above the pumps. By looking at Figure 19, the red curve represents the system curve for 1-inch tubing and single loop of the HTF, in other words, a loop that includes one HEX only. The blue curve represents the 1-inch tubing but for two parallel lines, assuming the chiller will cool two HEXs. The black solid line shows the HEX flow limit as provided by Alfa Laval. This constraint is possible since the HEX will have a relatively high pressure drop beyond this flow limit. The dashed magenta line represents the flow limit for two parallel loops, which is double the flow rate limit for one HEX. Looking at this graph, we can conclude the selected pump is suitable for our application. It seems clear that the operating points can move further to the left side if we incorporate valves to increase flow restriction and, hence, increase the pressure drop and reduce the flow rate. Two pumps similar to the Mokon chiller pump are selected for the two other HEX loops.

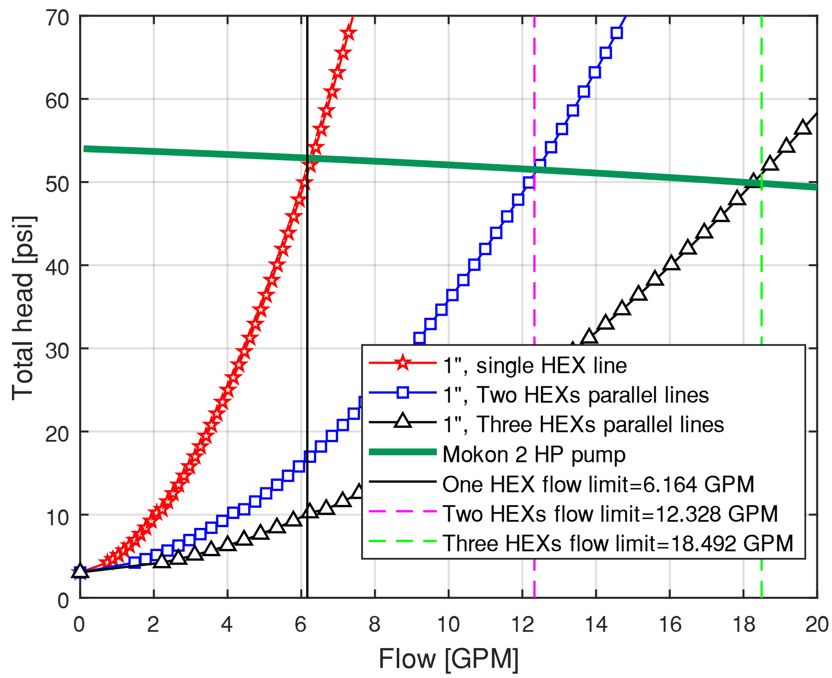

Figure 19. The pump curve vs one, two, and three heat exchanger system Curves

5.2.5 Schematics

The HTF cycle schematic is shown in Figure 5-20. Before each HEX, an immersion electric heater is used to fine tune the temperature setting. Shut-off valves are placed at different locations to allow the flow to be directed and enable each chiller to cool one, two, or the three heat exchangers. A flow meter is placed in each HTF line to estimate the cooling/heating capacity. Temperature sensors are inserted at different locations to assist in controlling the HTF temperature.

5.3 Instrumentation

A RTD, 1000 Ω, 4-wire, 1/8-inch probe diameter, Omega brand is used to measure the absolute temperature at different locations of the CO_2 and HTF loops. It has an accuracy of ±(0.15 + 0.002* T) where T ranges from T=-30 °C to 300 °C. RTD principle is based upon metals that produce a change in electrical resistivity with a change in temperature. The nominal resistance, which is 1000 Ω is defined at 0. The NI module used for the RTD measurement, which will be highlighted in a data acquisition subsection, has an excitation current (I) of 0.1 mA. The self-heating power I2R generated in the RTD is found to be 10 mW, where R is the RTD nominal resistance 1000 Ω. This self-heating power is less than an RTD with 100 Ω nominal resistance by a factor of 10. The 4-wire is the most accurate configuration compared to the 2-wire and the 3-wire ones. In the 2-wire, the lead wire resistance cannot be compensated for or canceled; thus, their resistances are included in the RTD measurement, which affects the RTD accuracy. The 3-wire configuration compensates for the lead wires, under the assumption that all the three lead wires have the exact same resistance. This enhances the accuracy but leaves an amount of the error in the reading. In the 4-wire configuration, a current source powers the circuit through two wires and the other two wires are used to read the RTD resistance value. Hence, the reading is proportional only to the RTD.

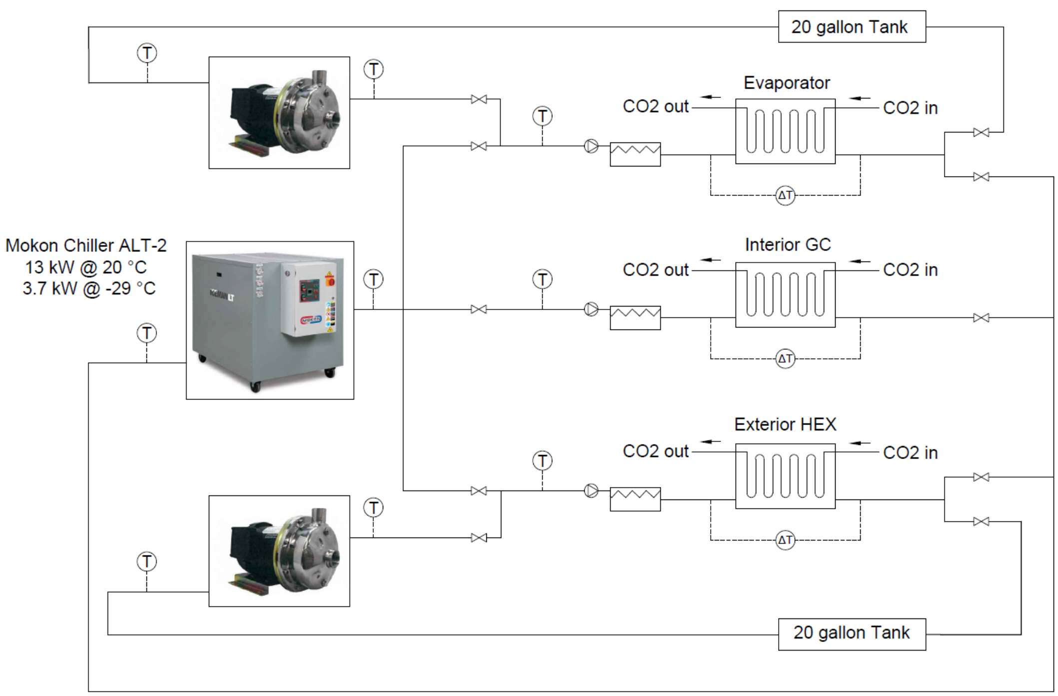

Figure 5-20. HTF Schematics

An absolute pressure measurement is conducted at the various points in the CO_2 loop by Omega MM series pressure sensor. It has a pressure range up to 175 bar. The output is 4-20 mA, and its accuracy is ±0.05% FS.

The CO_2 mass flow rate is measured by Emerson F025 Coriolis flow meter. It has a mass flow accuracy of ±0.5% of rate for gases and ±0.2% of rate for liquids. The flow meter has a pressure rating up to 160 bar and a temperature range from -100 °C to 204 °C. The Coriolis flow meter contains an energized vibrating tube. When the fluid passes through this tube the mass flow momentum results in a change in the tube vibration. Therefore, the tube will twist causing a phase shift. This phase shift is measured and can be correlated to the mass flow rate. An Emerson flow transmitter 1700 series is used, which carries the electronics needed in a remote mount fashion. The flow meter unit interfaces with the transmitter through a 9-wire cable.

The HTF mass flow rate is measured by a Rosemount magnetic flow meter 8700 series, which has a 0.25% of rate accuracy. It has a PTFE lining, which extends the flow meter temperature range from -29 °C to 177 °C. It has a maximum pressure rating that depends on the fluid operating temperature. The maximum pressure is 215 psi at 177 °C and 285 psi for temperatures from -29 °C to -38 °C. Both F series and Rosemount flow sensors have the capability to generate frequency signals that are proportional to the measured mass flow rate.

National Instruments' data acquisition devices along with LABVIEW software are used for acquiring the measurement signals to a PC and for generating control signals. A Compact DAQ 9179 USB chassis with 14 slots was chosen, which supports analog I/O, digital I/O, and counter/timer measurements. Each slot can accommodate a data acquisition module that can be voltage, current, or a module dedicated for specific type of measurements such as thermocouple or RTD. For acquiring CO_2 loops RTD signals, 3 units of NI 9226 module dedicated for RTD measurement, with a nominal resistance of 1000 Ω was chosen, each with 8 channels. The module has an accuracy of ± 0.15 °C, for a temperature range from -200 °C to 150 °C. For pressure signals, a current module NI 9208, which supports ±20 mA current measurement with 16 channels, was selected. To measure the flow meter signals, a counter module NI 9361 was chosen. The module has 8 channels where each channel can be configured to read single pulse train. The variable frequency drive used to control the compressor speed is used to measure the absorbed power of the compressor; hence, no dedicated watt-meter sensor is needed. Figure 5-21 shows photos for the different instrumentation used and discussed above.

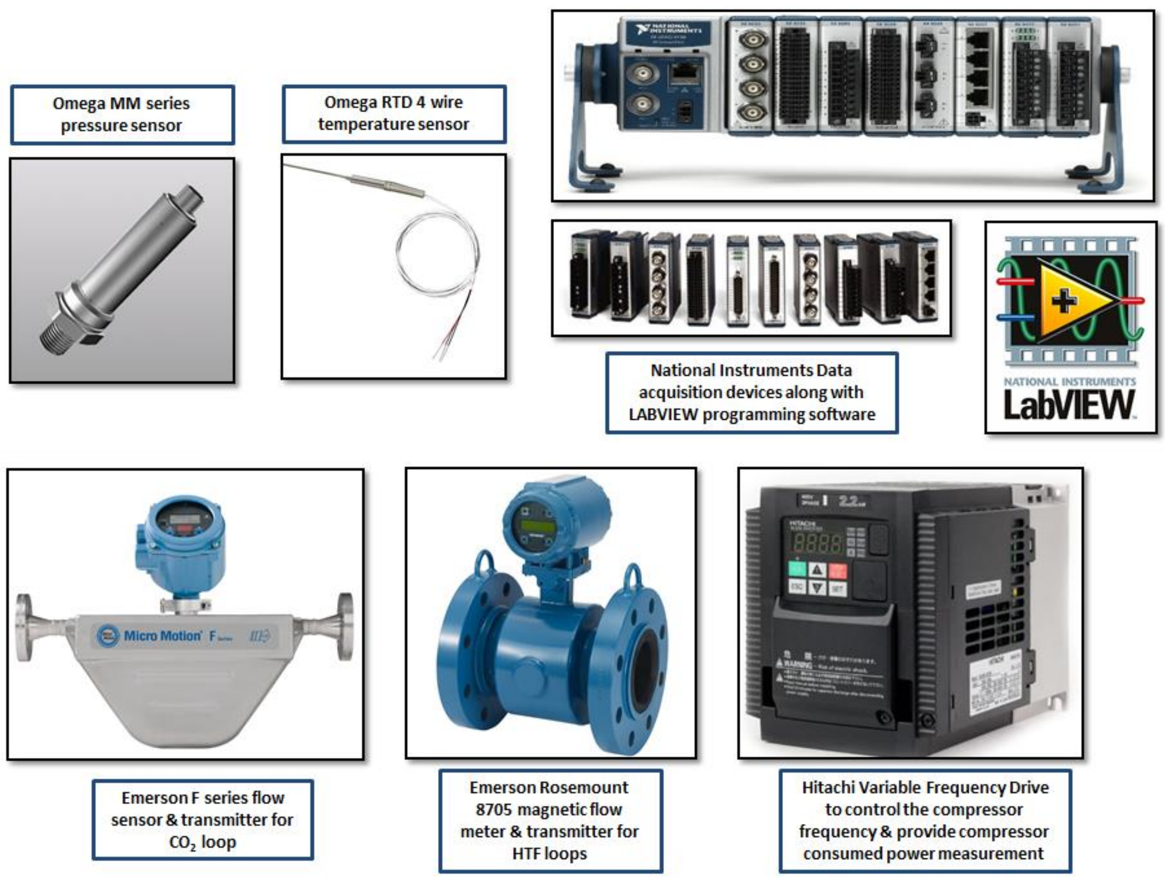

Figure 5-21. Various Instrumentation used in the CO_2 transcritical heat pump test rig facility

5.4 Test-Rig Layout & 3D CAD Modeling

Figure 5-22 shows the test rig detailed schematic layout showing the location of pressure, temperature, and flow sensors in the CO_2 loop. The schematic also shows the pressure relief valves and their respective cracking pressures.

The 3D CAD design is shown in Figure 5-23. Several considerations were made in constructing the 3D CAD. First, it enables testing with either the manual or electronic expansion valve if need to be attached in parallel. Second, it has the capability of flow reversion for the OHEX to allow effective operation. The OHEX acts as an evaporator or condenser GC, depending on the cycle mode. As advised by Alfa Laval, for an evaporator mode, the fluid shall enter from bottom and leaves from the top to ensure that no liquid leaves the evaporator. While in the condenser mode, the fluid shall enter from the top and leaves from the bottom so that any condensed liquid leaves the HEX. The test-rig is also designed such that all components drain to the accumulator during the off cycle. A portable frame with wheels is also considered so that the test-rig fits through a standard door for transportation.

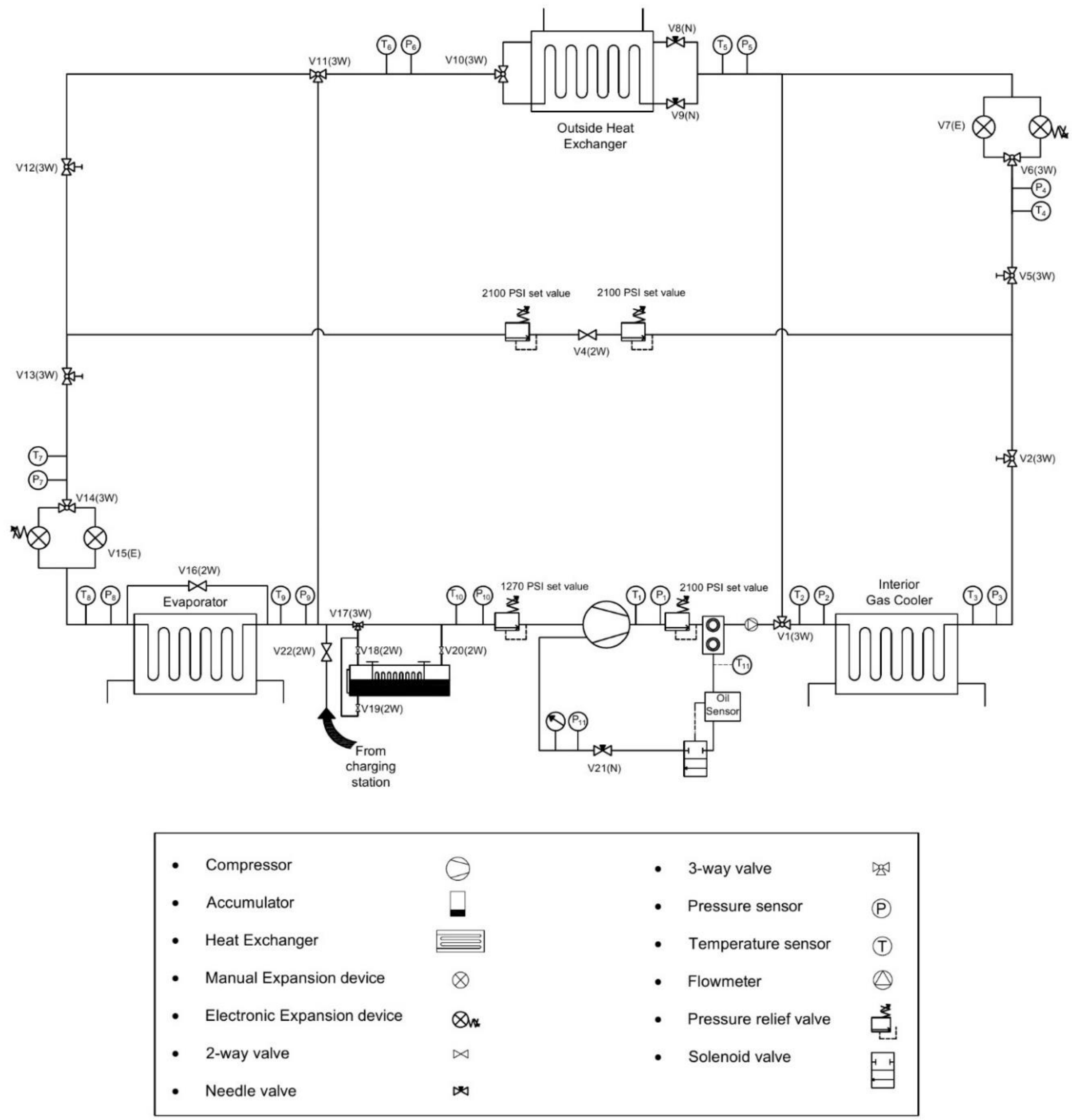

Figure 5-22. Test-rig layout that shows the location of different sensors

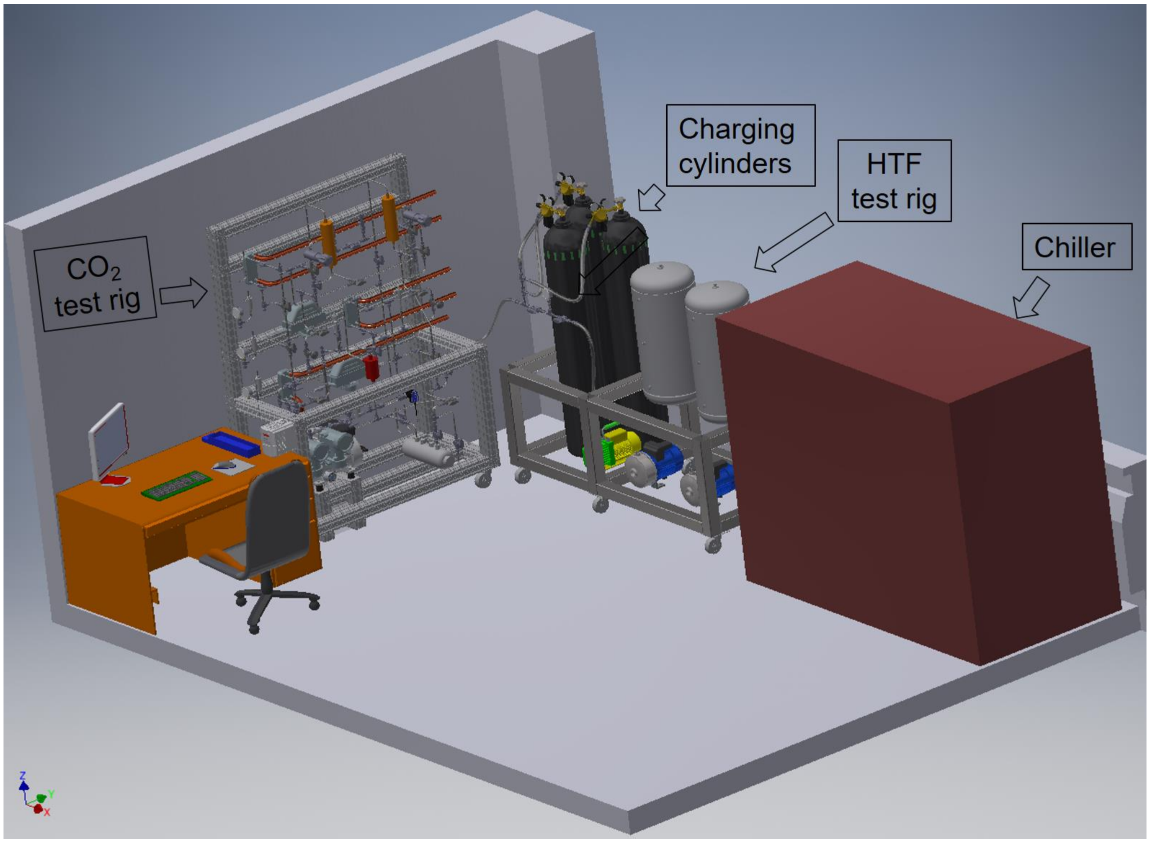

Figure 5-23. 3D CAD of the test-rig within the Turbomachinery Lab space at MSU

After the build completion, the CO_2 test rig was tested by 300 PSI Nitrogen gas to detect the points of leaks. After identifying and fixing all leaks, the test rig was left pressurized overnight under 500 PSI pressure, and no leak was detected. The HTF test rig was also tested by 50 PSI air pressure to identify and fix all sources of leaks.

The CO_2 test rig was then vacuumed to 290 Micron. When the vacuum pump was shut off, the system was able to hold a vacuum level of 590 Micron for 25 minutes.

To charge the system with CO_2, this was done in two steps: first by charging gas CO_2 until the system pressure reaches 100 PSI, then if more charging mass is needed, a liquid CO_2 is pumped into the system. The liquid and gas cylinders used from Airgas were CD I200S (CARBON DIOXIDE INSTRUMENT GR 4.0 SIZE 200 CGA 320 SYPHON), and CD I200 (CARBON DIOXIDE INSTRUMENT GR 4.0 SIZE 200 CGA 320) respectively. A Concoa pressure regulator is used for the CO_2 gas cylinder. No regulator was needed for the liquid cylinder, but a connector/adapter setup that is shown in Figure 5-24.

Figure 5-24. CO_2 Liquid cylinder connector/adapter setup

As a rule of thumb, a refrigerant charge of 2-4 pound per ton of cooling is needed. For our system, since the maximum cooling capacity is 5.5 kW ~ 1.56 Ton refrigeration, the range of charge needed is 3.12-6.24 pounds, that is 1.4-2.8 kg. We charged the system with 1.5 kg.

Our estimation of the system volume tubing is not more than 1.0 L, plus 2.7 L for the Accumulator, plus 6.1 L for low-pressure side of the compressor, and 0.25 L of high-pressure side of the compressor gives ~10 L. Experimentally, this was verified by charging the system with Nitrogen and applying the ideal gas law. The system volume estimation was 7-10 L, where the volume variability is due to the variability in pressure sensor readings.

The compressor is equipped with relief valves at the inlet and output port. Additionally, four Parker pressure relief valves are installed at different locations with their respective cracking pressure shown in Figure 5-22.

A clear polycarbonate glass is installed all around the CO_2 test rig to provide protection for the personal involved in the operation. Extension bars are fabricated and connected to the valve bodies to operate them through the glass during the system operation. After the leak test, the CO_2 test rig is insulated.

5.5 System Build & Photos

The experimental platform consists of two separate but connected test rigs: one for CO_2 and one for the HTF connected by flexible tubes that carry the heat transfer fluid. The next series of photos shows the progress of building both test rigs with photographs of the several components used.

Figure 5-25. CO_2 test rig frame on the start of the build at the Turbomachinery Lab showing the F-series flow sensor and few tubing connected to the flow sensor

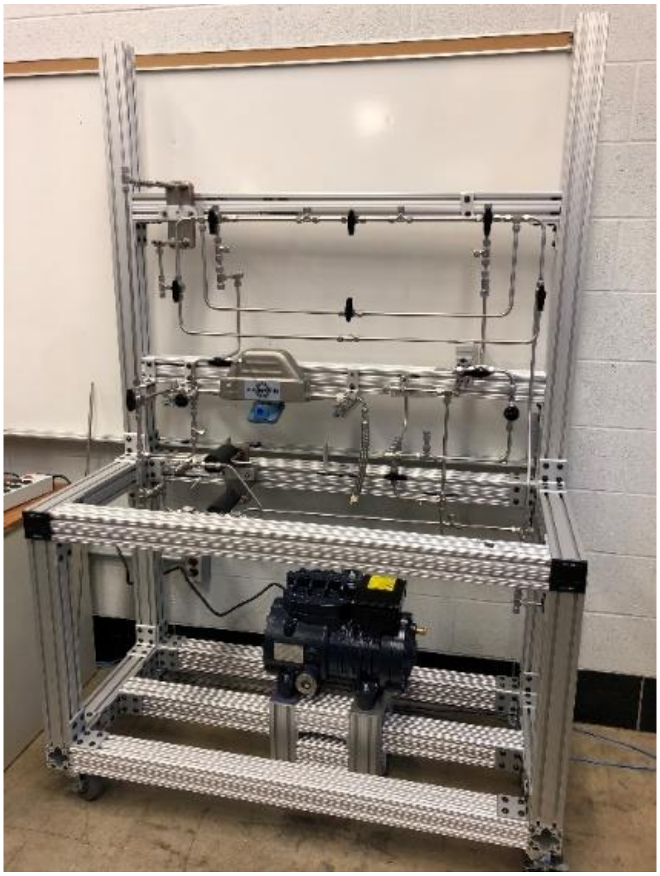

Figure 5-26. The Dorin CD200-CD180H Compressor mounted on its frame within the test rig

Figure 5-27. The Temprite oil separator and its relative size with respect to a keyboard. The tubing is connected to the oil return line. The two black caps are covering the sight glasses.

Figure 5-28. A photo schematic showing the addition of the suction line, discharge line, and the lines around the accumulator. The photo also shows the integration of four pressure relief valves.

Figure 5-29. A photograph shows the integration of pressure gauges connected to different points in the system. The pressure gauges are only for quick monitoring of the system pressure. The system is equipped with pressure sensors to provide thermodynamic property calculations during the system run on LabVIEW and for postprocessing on MATLAB.

Figure 5-30. A photo showing the accumulator that has been manufactured by Temprite and its relative size with respect to a keyboard

Figure 5-31. A photo showing the accumulator and a 3D-printed enclosure (left), the accumulator assembled in the enclosure (middle), and the accumulator integrated with the test rig (right)

Figure 5-32. Photos show the initial build of the HTF test rig. The mounting of the two tanks to the HTF frame (left), the soldering of the HTF copper tubes at the MSU machine shop (middle), and the integration of the copper tubes to the test rig (right).

Figure 5-33. Photo shows the Mokon Chiller at the Turbomachinery lab

Figure 5-34. A Photo shows the HTF test rig after connecting most of the copper tubing and the three Rosemount Magnetic flowmeters

Figure 5-35. A Photo shows the CO_2 test rig after fixing a clear polycarbonate glass sheet from the test rig back side

Figure 5-36. Photos showing the progress of connecting the three cylinders; Nitrogen, liquid CO_2, and Gas CO_2 (left) to the system through a wall mounted charging panel (right)

Figure 5-37. Photo shows the CO_2 test rig after the tubing integration completion and fully enclosed by clear polycarbonate glass

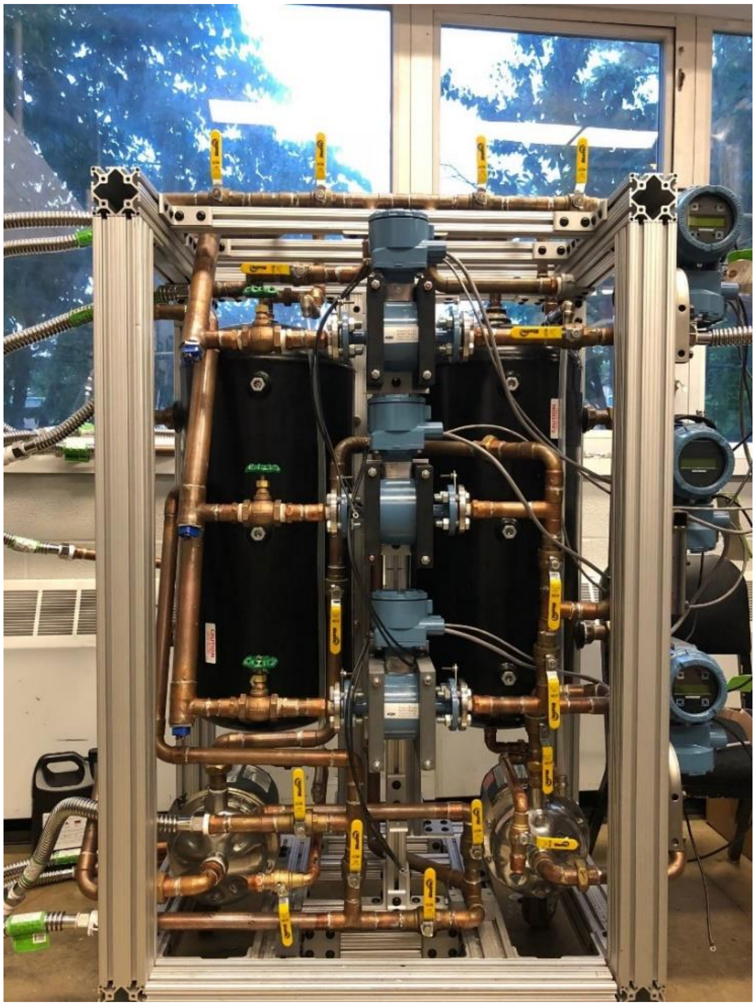

Figure 5-38. Photo shows the HTF test rig after copper pipes integration completion and connecting the Rosemont transmitters to the flowmeter

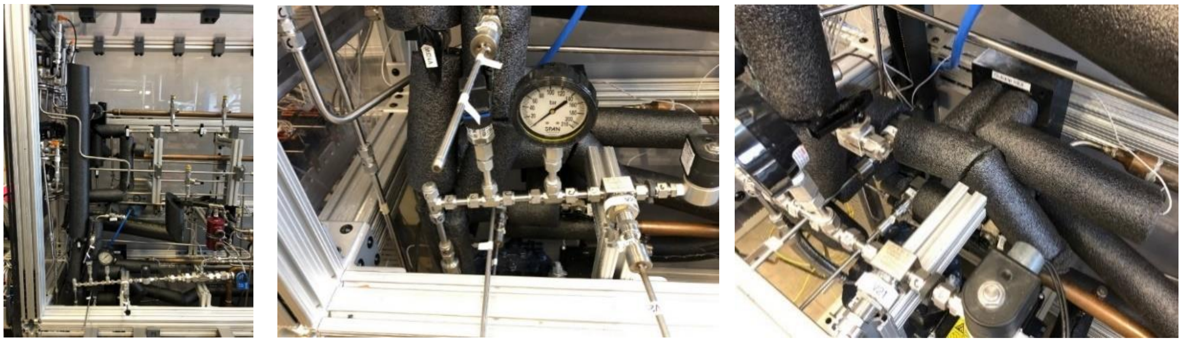

Figure 5-39. Photos shows the progress of insulating different parts of the CO_2 test rig tubing

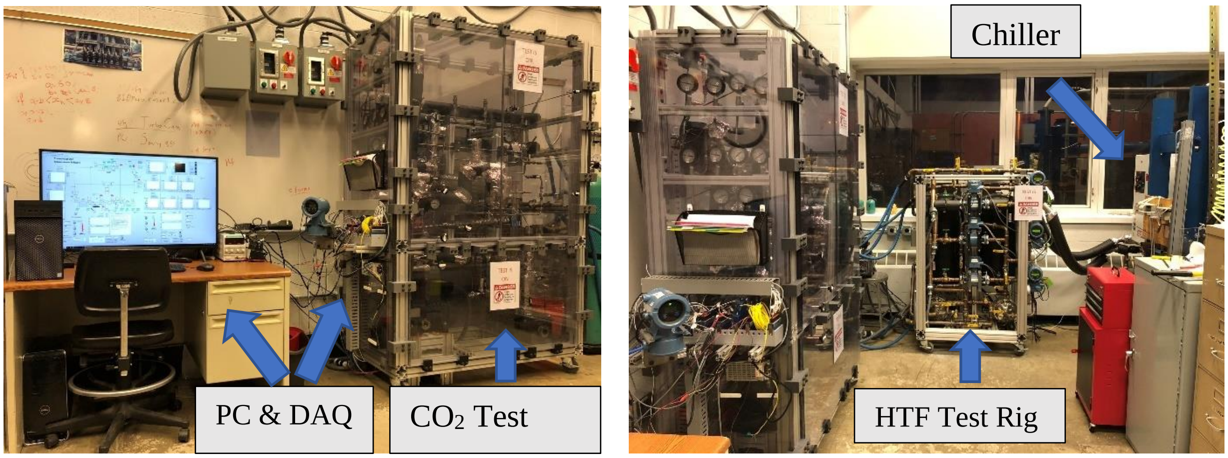

Figure 5-40. Complete photos of the experimental test rig. The left photo shows the CO_2 test rig with the data acquisition and PC. The right photo shows the HTF test rig connected to both the chiller and the CO_2 test rig from the right and the left respectively.

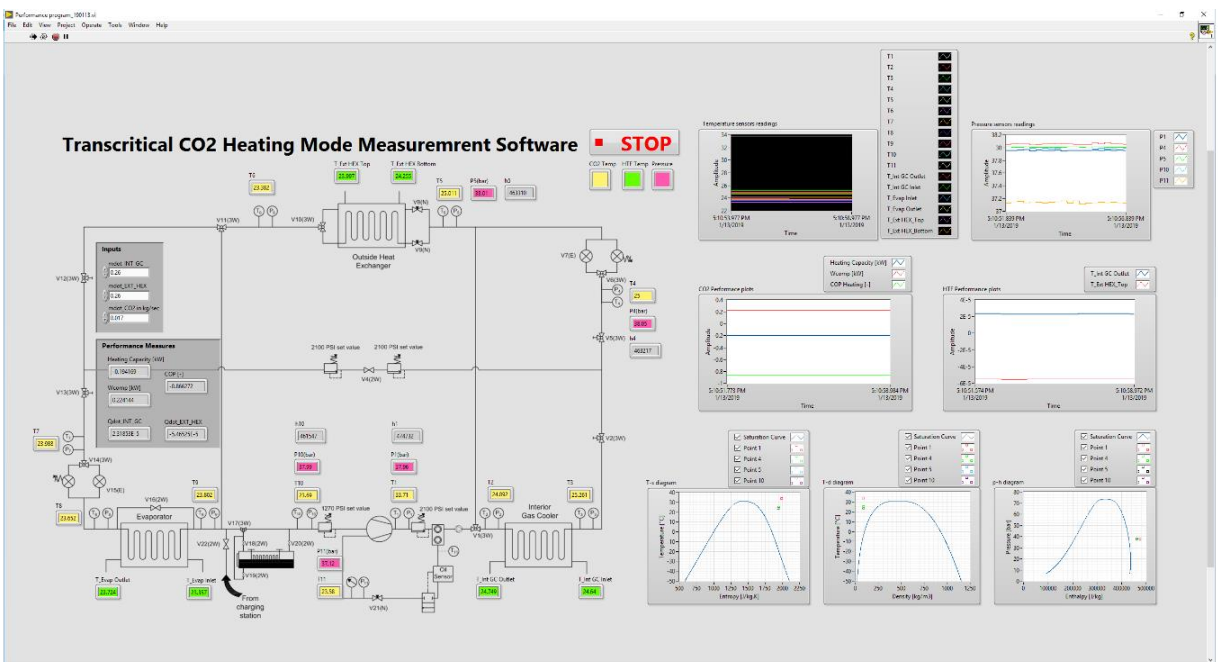

Figure 5-41. A Screenshot showing the developed LabVIEW Test Program that monitor the system temperatures, pressure, and flow in real time and plots the p-h, T-s, and T-d diagrams

Chapter 6: Experimental Testing and Results

The test matrix in Table 6-1 was developed to experimentally investigate the performance of the cooling and heating cycles. Each row represents a set of four or five steady state measurements. All the measurements are conducted at a constant HTF evaporator mass flow rate of 0.22 kg/s and a constant HTF gas cooler mass flow rate of 0.07 kg/sec. The HTF loops inlet temperatures of both the evaporator and the gas cooler are shown in the table first and second columns. All measurements are taken at a constant compressor speed of 1740 rpm. For each measurement, when steady state is reached, the data is recorded for five minutes and the mean value of each measured variable is computed to represent the test point steady state measurement.

Table 6-1. Test Matrix showing the operating conditions for each test point

$T_{HTF_{Evpin}}$ [°C]	$T_{HTF_{GCin}}$ [°C]	Test point	p_{GC} [bar]	Max energy balance variability: y [%]
5	20	M1, M2, M3, M4	78.1, 79.1 81.2, 82.3	0.16, 0.20, 0.15, 0.20
10	25	M5, M6, M7, M8	78.6, 81.5, 83.2, 85.8	0.24, 0.19, 0.17, 0.10
	30	M9, M10, M11, M12	87.8, 89.9, 91.4, 93.2	0.07, 0.07, 0.09, 0.16
15	30	M13, M14, M15, M16	87.7, 89.7, 91.7, 93.6	0.16, 0.18, 0.12, 0.08
	35	M17, M18, M19, M20	89.3, 91.7 93.5, 95.0	0.22, 0.22, 0.19, 0.09
20	35	M21, M22, M23, M24, M25	89.9, 91.3, 92.6, 95.0, 95.5	0.40, 0.36, 0.36, 0.26, 0.26

6.1 Test Method and Validation

The HTF was run first, and after reaching the desired operating temperatures and flow rates, the CO_2 loop was run. The steady state criteria was used for each test point to determine that steady state was obtained. It is based on checking the energy balance (y) across the CO_2 gas cooler, the evaporator, the compressor power, and the oil separator as shown in Eqn. (6.1). The oil separator is included in the equation due to the heat loss in the transient period that gradually decreases as the system approaches the steady state. The equation is normalized with respect to the HTF gas cooler capacity. The moving average is calculated for the variable y. The variable y is shown for the measurements in the last column of Table 6-1. In all the measurements, the moving average of the variable y is bounded within ±0.4%.

$$y\,(\%) = \frac{\dot{Q}_{h} + \dot{Q}_{OS} - \dot{Q}_{c} - \dot{W}_{comp}}{\dot{Q}_{h}} \tag{6.1}$$

Figure 6-1 shows the transient response of the system for the heat exchanger capacities and the compressor power, while Figure 6-2 shows the moving average of the energy balance variable for the same measurement case. In this measurement case, the steady state measurement is calculated from the last five minutes in the 30 minutes measurement duration.

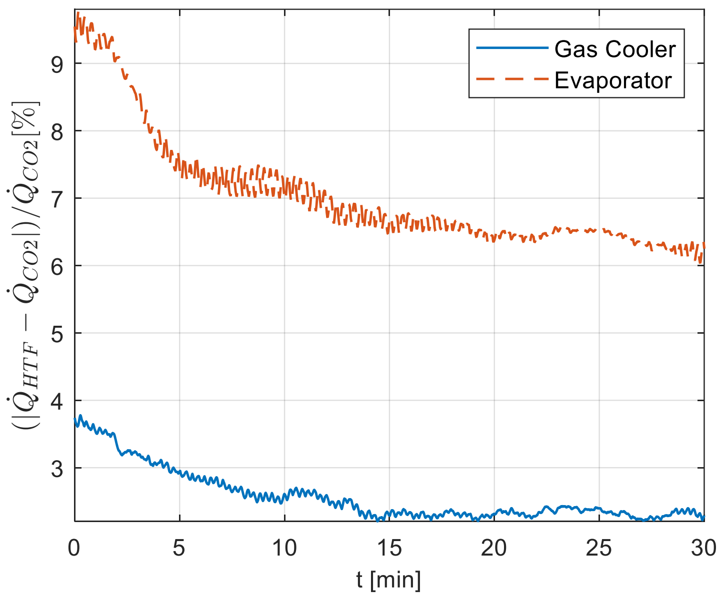

Figure 6-1. The energy balance across the heat exchangers capacities M1 measurement case

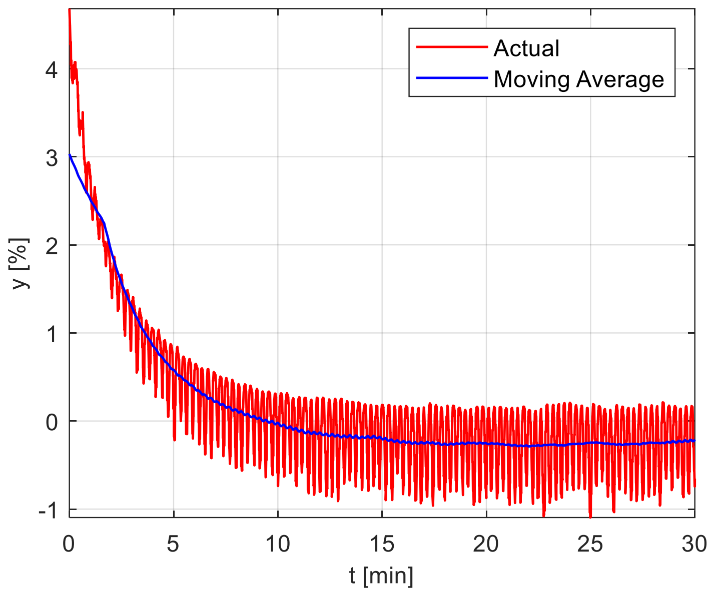

Figure 6-2. The energy balance actual and moving average signals for M1 measurement case

6.2 Uncertainty and Repeatability

The uncertainty in COP is computed according to [70]. The uncertainty in the calculated enthalpy using NIST REFPROP is computed according to [71]. For the temperature and pressure range here, the uncertainty in the enthalpy calculation is less than or equal to ±1.5%. The uncertainty in the calculated cooling and heating COP is within below 6.5%. To assess the system measurement repeatability, the test point M5 was repeated five times on different dates as shown in Table 6-2. The table shows the input conditions and several computed quantities. The mean and standard deviation values are shown in Table 6-2 and show the variability ranging between ~0.2% and 1.8%.

The refrigerant mass flow rate signal for M1 is shown in Figure 6-3. As mentioned in Section 2, the placement of the flow meter downstream the compressor and after the oil separator helps suppressing the compressor pulsations. This is demonstrated with the flow signal not containing any pulsation. Any oscillations left in the signal is attributed to the fluctuation in the measured temperature due to the fluctuation in the HTF supplied by the chiller, therefore, this consequently affects the pressure and hence the flow rate.

Table 6-2. Repeatability test results for Measurement M5

Date	**Oct 21, 2019**	**Oct 29, 2019**	**Nov 11, 2019**	**Dec 3, 2019**	**Dec 16, 2019**	**Mean**	**Standard Deviation [%]**
Test point	M5_R1	M5_R2	M5_R3	M5_R4	M5_R5		
$\mathbf{T_{HTF_{GCin}}}$ (°C)	30.3	30.2	30.3	30.2	30.2	30.24	0.18
$\mathbf{T_{HTF_{EVPin}}}$ (°C)	15.3	15.2	15.1	15.1	15.1	15.16	0.59
$\dot{\mathbf{m}}_{\mathbf{r}}$ (kg/s)	0.0171	0.0163	0.0169	0.0167	0.0167	0.0167	1.78
$\dot{\mathbf{m}}_{\mathbf{GC}}$ (kg/s)	0.0704	0.0706	0.0701	0.0694	0.0704	0.0702	0.67
$\dot{\mathbf{m}}_{\mathbf{Evp}}$ (kg/s)	0.225	0.225	0.224	0.225	0.224	0.2246	0.24
$\mathbf{p_{GC}}$ (bar)	93.6	95	93.2	93.4	93.8	93.8	0.75
$\dot{\mathbf{Q}}_{\mathbf{H}}$ (kW)	4.34	4.25	4.26	4.24	4.24	4.27	0.99
$\dot{\mathbf{Q}}_{\mathbf{C}}$ (kW)	2.76	2.7	2.74	2.71	2.73	2.73	0.88
$\dot{\mathbf{W}}_{\mathbf{comp}}$ (kW)	1.8	1.78	1.75	1.76	1.75	1.77	1.23
$\mathbf{COP_C}$ (-)	1.53	1.51	1.56	1.54	1.56	1.54	1.38
$\mathbf{COP_h}$ (-)	2.41	2.38	2.43	2.41	2.43	2.41	0.85

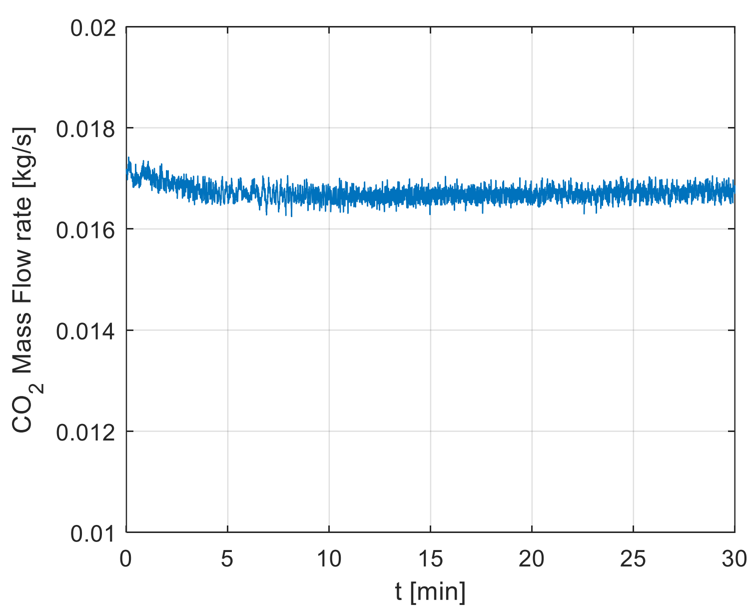

Figure 6-3. The CO_2 mass flow rate signal for M1 measurement case

6.3 Results and Discussion

Figure 6-4 shows the cooling COP plot against the GC pressure all at different HTF GC and evaporator inlet temperatures. The test points M1 through M25 are shown in the test matrix in Table 6-1. As shown in Figure 6-4, the increase of the GC inlet temperature from 25 °C to 30 °C while the evaporator inlet temperature was set to 10 °C reduces the optimum COP from 1.87 to 1.50. Additionally, the change of the GC inlet temperature from 30 °C to 35 °C while the evaporator inlet temperature was set to 15 °C reduces the optimum COP from 1.50 to 1.29. These COP changes are relatively higher compared to the effect of the increase of the evaporator inlet temperature. The increase of the evaporator inlet temperature from 10 °C to 15 °C, while the GC inlet temperature was set to 30 °C, increases the optimum COP from 1.50 to 1.56. Similarly, the increase of the evaporator inlet temperature from 15 °C to 20 °C, while the GC inlet temperature was set to 35 °C increases the optimum COP from 1.29 to 1.33.

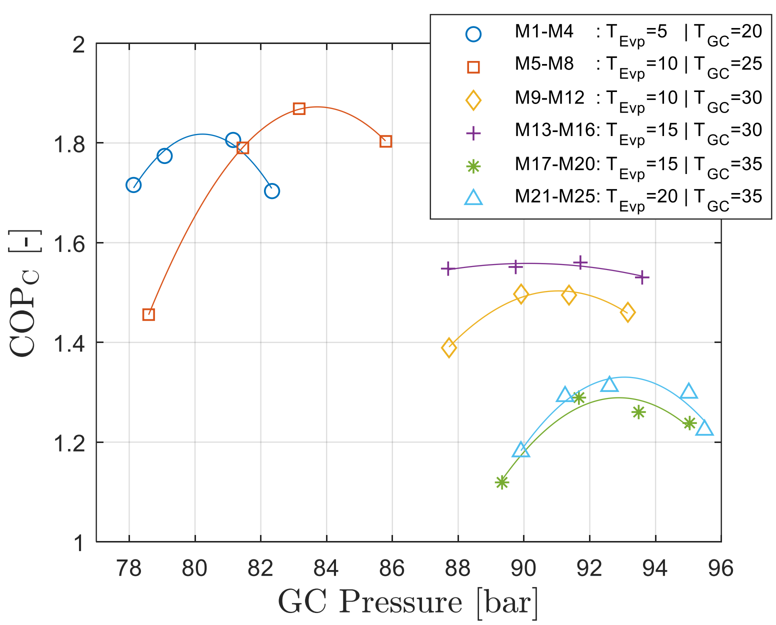

Figure 6-4. The Cooling COP measurements at different HTF inlet temperatures

A similar trend is shown in Figure 6-5 for the heating COP. These results correlate with results reported in the literature that the optimum COP occurs at the minimum GC CO_2/secondary inlet temperature and the maximum evaporator CO_2/secondary inlet temperature. In all the 25 measurement cases, the minimum and the maximum difference between cooling and heating COP is 0.86 and 0.92 respectively.

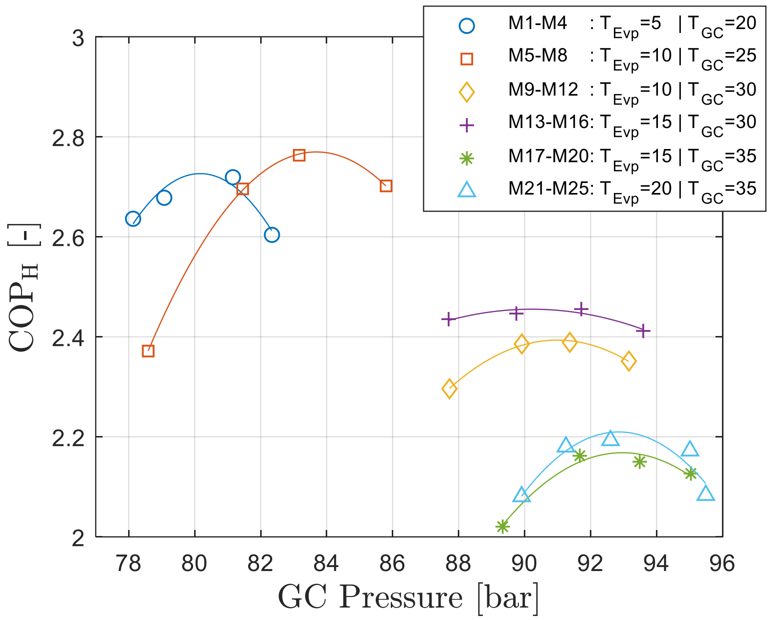

Figure 6-5. The Heating COP measurements at different HTF inlet temperatures

The change of the CO_2 mass flow rate is shown in Figure 6-6 for the test cases in Table 6-1. For each measurement set, the increase in the GC pressure decreases the mass flow rate in almost linear fashion. This is mainly due to the compressor volumetric efficiency decrease as demonstrated for several CO_2 compressors [49]. Moreover, the increase in the HTF evaporator inlet temperature, which results in an increase in the evaporation pressure, results in an increase in the CO_2 mass flow rate as shown in [40] and [26].

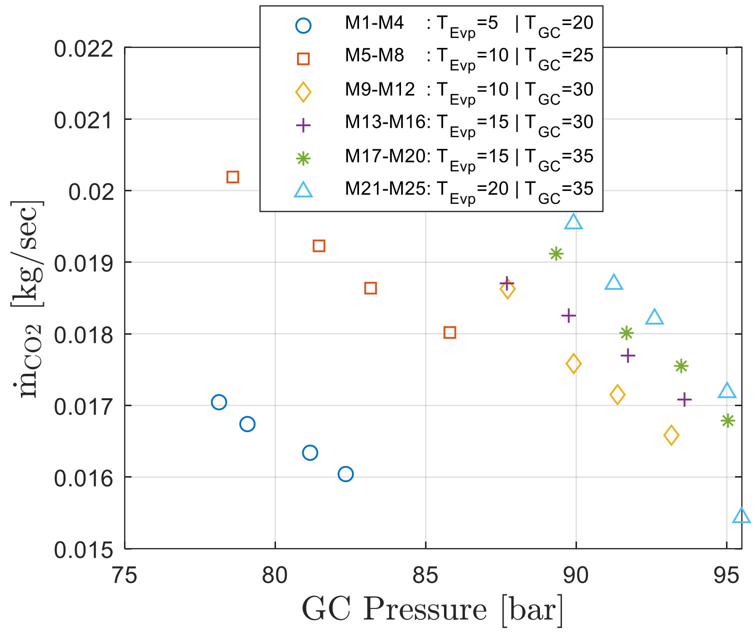

Figure 6-6. The CO_2 mass flow rate for different HTF GC and evaporator inlet temperatures at different pressures

Figure 6-7 shows the useful superheat for each test point in Table 6-1 at the corresponding GC pressure. The useful superheat is the one taking place inside the evaporator. For each set of test points, the effect of changing the GC pressure for the ranges shown results in no more than 1 K superheat. The increase in the HTF GC inlet temperature from 25 °C to 30 °C and from 30 °C to 35 °C, while the HTF evaporator inlet temperature was kept constant at 10 °C and 15 °C respectively results in negligible change in the useful superheat. On the other hand, the increase in the HTF evaporator inlet temperature increases the useful superheat significantly as shown for the increase from 5 °C through 20 °C.

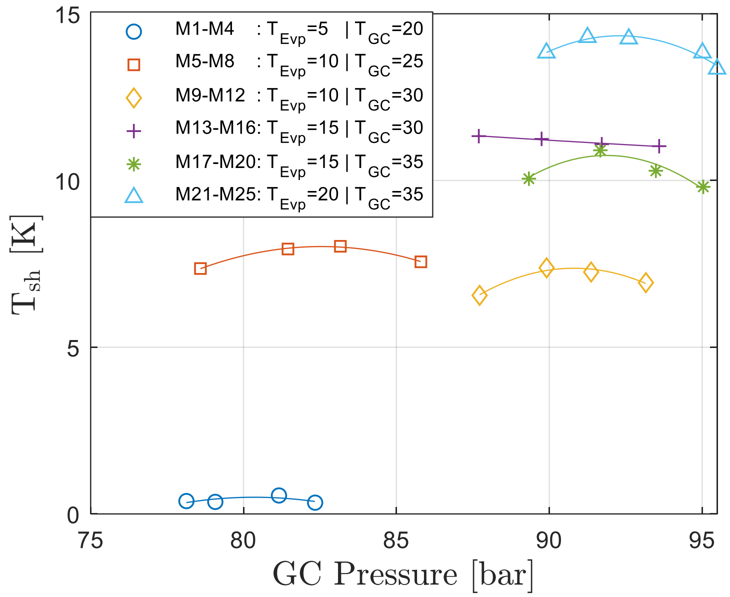

Figure 6-7. The superheat taking place inside the evaporator for different HTF GC and evaporator inlet temperatures at different pressures

Chapter 7: Conclusions and Future work

7.1 Conclusions

- The COP can increase by more than 7% if the cycle makes a transition from the subcritical to the transcritical.
- $\dot{Q}_c$ and COP are non-conflicting in the range from critical pressure to p_{GC} of maximum COP, and conflicting above this point till the isotherm becomes vertical.
- Maximum COP gas cooler pressure does not change significantly across different compressors, but the maximum $\dot{Q}_c$ gas cooler pressure is dependent on the compressor performance due to the difference in the volumetric efficiency.
- Pareto Fronts are developed that represent the tradeoff between COP and $\dot{Q}_c$ in the range of conflicting objectives.
- The Gain/Loss ratio can be used as a transitioning criteria from one solution to another on the Pareto Front.
- At T_3=54 °C, the Pareto Front becomes only one point, representing the maximum COP and the maximum $\dot{Q}_c$ solution.
- COP and $\dot{Q}_c$ increase or decrease with increasing useful superheat depending on the operating conditions due to the competing effects of the mass flow rate and the enthalpy difference across the compressor and the evaporator
- The compressor isentropic and volumetric efficiency correlations have considerable effects on the Pareto Front.
- COP and $\dot{Q}_c$ contour maps can aid in predicting the COP, $\dot{Q}_c$ and p_{GC} in the transition from one point to another across the Pareto Fronts.

- An offline optimization approach is developed that could enable the system to work close to its maximum COP, maximum $\dot{Q}_c$, a tradeoff solution, or at a point where $\dot{Q}_c$ and COP are non-conflicting for lower $\dot{Q}_c$ avoiding ON-OFF cycling, and switch as desired.
- A hybrid offline/online optimization and control approach is proposed that can reduce the time to approach the desired optimum compared to online methods only. Compared to Offline methods only, it can additionally enhance COP and $\dot{Q}_c$ based on the actual system behavior/characteristics, while it is also able to adapt to changing system behavior.
- The experimental test results showed:
    - The placement of the flow meter downstream the compressor and after the oil separator helps suppressing the compressor pulsations.
    - The HTF GC inlet temperature has a significant effect on the COP compared to the HTF evaporator inlet temperature.
    - With the increase of the GC pressure, the mass flow rate decreases approximately in a linear fashion.

7.2 Future Work

Several Pathways can be explored based on this thesis research work:

- First, including other objectives in the optimization problem. For example, for a modified cycle with an internal heat exchanger (IHX), the length of the IHX can a be variable subject to optimization and the pressure drop, size, or cost could be a third objective
- Several mathematical models are available in the literature for the heat pump system components. The heat exchangers' dynamics dominate the system behavior as the compressor and the expansion device have very fast dynamics; and, hence, they are modeled as static, semi-empirical relationships. For the purpose of implementing new

control algorithms on the experimental test-rig, developing a mathematical model for the test rig and validating the model against experimental data could simplify the control design process by simulating the controller before experimental testing and validation.

APPENDIX

Table A-1. Bill of material for the CO_2 transcritical heat pump system built at the MSU Turbo Machinery Lab

Category	Component(s)	Manufacturer (Distributor)	Model and/or Part number	Qty
Compressor	Compressor unit & motor	Dorin (Blissfield)	CD200 - CD180H	1
	Variable Frequency Drive	Hitachi (Williams Distributing)	WJ200-022LF	3
Oil Separation	Oil Separator	Temprite	Model 131: Hermetic	1
	Oil sensor	HB Products (Temprite)	HBOC	1
	Oil solenoid valve	HB Products (Temprite)	V150	1
Heat exchangers	Heat Exchanger	Alfa Laval	AXP10-20H-F	3
Expansion Device	Manual	Swagelok (H.E. Lennon)	SS-31RS4	2
	Electronic (EXV)	Carel (United Refrigeration Inc)	E2V14CS000	2
	EXV Driver	Carel (United Refrigeration Inc)	EVD0000E50	1
Accumulator	Accumulator	In house design manufactured by Temprite		1
HTF loops	Chiller	Mokon	ALT-2	1
	Pump	Scott (Kerr Pump)	MP231 304 SS FTD 1.25x1 NPT, EPDM/CB/SIL SEAL 5.75" IMP DIA 2HP 3500RPM	2
Temperature Measurement	Resistance Temperature Detector (RTD)	Omega	PR-11-3-1000-1/8-6-E-120	20
Pressure measurement	Absolute pressure transducers	Omega	MMA2.5KC1B2C5T4A6CE	10

Table A-1 (cont'd). Bill of material for the CO_2 transcritical heat pump system built at the MSU Turbo Machinery Lab

Flow Measurement	F series Coriolis Flow meter for CO_2	Emerson	F025PB77CRAAEZZZZ	**1**
	F series Coriolis Flow meter transmitter for CO_2		1700C11ABAEZZZ	1
	Rosemount Magnetic Flow meter for HTF		8705TSA005C1M0N5	3
	Rosemount Magnetic Flow meter transmitter for HTF		8732EMR1A1N5M4	3
Data Acquisition	Data Acquisition Chassis	National Instrument	Compact DAQ (cDAQ-9179). Part number 783597-01	1
	Flow Sensor module		NI 9375	1
	Pressure sensors module		NI 9208 Spring,16-Ch current	1
	RTD module		NI 9226 Spring, 8-Ch RTD, PT1000, 24-bit	3
Pressure relief valves	Pressure relief valves	Parker	4M4F-RH4A-EPRT-SS-K3	1
			4M4F-RH4A-VT-SS-K4	1
			4M4F-RH4A-EPRT-SS-K4	2
CO_2 Fittings and Valves	316/316L SSL Seamless	Swagelok (H.E. Lennon)	Misc.	NA
HTF Fittings and Valves	Copper fittings	Supply house	Misc.	NA

BIBLIOGRAPHY

BIBLIOGRAPHY

[1] M. J. Molina and F. S. Rowland, "Stratospheric sink for chlorofluoromethanes: chlorine atom-catalysed destruction of ozone," *Nature,* vol. 249, pp. 810-812, 1974.

[2] Montreal Protocol , "Montreal protocol on substances that deplete the ozone layer," *Washington, DC: US Government Printing Office,* vol. 26, 1987.

[3] M.-H. Kim, J. Pettersen and C. W. Bullard, "Fundamental process and system design issues in CO2 vapor compression systems," *Progress in energy and combustion science,* vol. 30, pp. 119-174, 2004.

[4] A. Mackay, "Climate change 2007: impacts, adaptation and vulnerability. Contribution of Working Group II to the fourth assessment report of the Intergovernmental Panel on Climate Change," *Journal of Environmental Quality,* vol. 37, pp. 2407-2407, 2008.

[5] NASA, "How climate is changing," 2019. [Online]. Available: https://climate.nasa.gov/effects/. [Accessed 13 Feb. 2019].

[6] Kyoto Protocol, "United Nations framework convention on climate change," *Kyoto Protocol,* vol. 19, 1997.

[7] A. A. Kharazi, P. Akbari and N. Müller, "Preliminary study of a novel R718 compression refrigeration cycle using a three-port condensing wave rotor," *Journal of engineering for gas turbines and power,* vol. 127, pp. 539-544, 2005.

[8] W. S. Bodinus, "The rise and fall of carbon dioxide systems: The first century of air conditioning," *ASHRAE journal,* vol. 41, p. 37, 1999.

[9] G. Lorentzen, "Trans-critical vapour compression cycle device Patent No," *WO/07683,* 1990.

[10] G. Lorentzen and J. Pettersen, "A new, efficient and environmentally benign system for car air-conditioning," *International Journal of Refrigeration,* vol. 16, pp. 4-12, 1993.

[11] P. Nekså, "CO2 as Refrigerant for systems in transcritical operation," *Principles and Technology status, EcoLibrium,* vol. 3, pp. 26-31, 2004.

[12] S. Sawalha, "Carbon dioxide in supermarket refrigeration," *Doctoral Dissertation, KTH,* 2008.

[13] E. W. Lemmon, M. L. Huber and M. O. McLinden, *NIST Standard Reference Database 23: Reference Fluid Thermodynamic and Transport Properties-REFPROP, Version 9.1, National Institute of Standards and Technology,* 2013.

[14] F. Kauf, "Determination of the optimum high pressure for transcritical CO2 refrigeration cycles," *International Journal of Thermal Sciences,* vol. 38, pp. 325-330, 1999.

[15] G. Lorentzen, "Revival of carbon dioxide as a refrigerant," *International journal of refrigeration,* vol. 17, pp. 292-301, 1994.

[16] N. Müller and J. O. Joseph, "A Closer Look at CO2 as a Refrigerant.," *ASHRAE Transactions,* vol. 115, 2009.

[17] H. Inokuty, "Graphical method of finding compression pressure of CO2 refrigerating machine for maximum coefficient of performance," in *The Fifth International Congress of Refrigeration, Rome,* 1928.

[18] L. Yang, H. Li, S.-W. Cai, L.-L. Shao and C.-L. Zhang, "Minimizing COP loss from optimal high pressure correlation for transcritical CO2 cycle," *Applied Thermal Engineering,* vol. 89, pp. 656-662, 2015.

[19] D. E. Boewe, R. P. McEnaney, Y. C. Park, J. M. Yin, C. W. Bullard and P. S. Hrnjak, "Comparative experimental study of subcritical R134a and transcritical R744 refrigeration systems for mobile applications," *Air Conditioning and Refrigeration Center. College of Engineering. University of Illinois at Urbana-Champaign,* 1999.

[20] S. M. Liao, T. S. Zhao and A. Jakobsen, "A correlation of optimal heat rejection pressures in transcritical carbon dioxide cycles," *Applied Thermal Engineering,* vol. 20, pp. 831-841, 2000.

[21] A. Yoshioka and S. Miura, "Development of Automobile Air Conditioning System Using CO2 Refrigerant," *Mitsubishi Heavy Industries Technical Review,* vol. 37, pp. 78-82, 2000.

[22] J. S. Brown, S. F. Yana-Motta and P. A. Domanski, "Comparitive analysis of an automotive air conditioning systems operating with CO2 and R134a," *International Journal of refrigeration,* vol. 25, pp. 19-32, 2002.

[23] V. Casson, L. Cecchinato, M. Corradi, E. Fornasieri, S. Girotto, S. Minetto, L. Zamboni and C. Zilio, "Optimisation of the throttling system in a CO2 refrigerating machine," *International Journal of Refrigeration,* vol. 26, pp. 926-935, 2003.

[24] J. Sarkar, S. Bhattacharyya and M. R. Gopal, "Optimization of a transcritical CO2 heat pump cycle for simultaneous cooling and heating applications," *International Journal of Refrigeration,* vol. 27, pp. 830-838, 2004.

[25] Y. Chen and J. Gu, "The optimum high pressure for CO2 transcritical refrigeration systems with internal heat exchangers," *International Journal of Refrigeration,* vol. 28, pp. 1238-1249, 2005.

[26] H. Liu, J. Chen and Z. Chen, "Experimental investigation of a CO2 automotive air conditioner," *International Journal of Refrigeration,* vol. 28, pp. 1293-1301, 2005.

[27] W. W. Yang, A. Fartaj and D. S. K. Ting, "CO2 automotive A/C system optimum high pressure control," in *SAE Technical Paper,* 2005.

[28] T. Tamura, Y. Yakumaru and F. Nishiwaki, "Experimental study on automotive cooling and heating air conditioning system using CO2 as a refrigerant," *International Journal of Refrigeration*, vol. 28, pp. 1302-1307, 2005.

[29] H. Cho, C. Ryu and Y. Kim, "Cooling performance of a variable speed CO2 cycle with an electronic expansion valve and internal heat exchanger," *International Journal of Refrigeration,* vol. 30, pp. 664-671, 2007.

[30] R. Cabello, D. Sánchez, R. Llopis and E. Torrella, "Experimental evaluation of the energy efficiency of a CO2 refrigerating plant working in transcritical conditions," *Applied thermal engineering,* vol. 28, pp. 1596-1604, 2008.

[31] Y. Chen and J. Gu, "The optimum high pressure for CO2 transcritical refrigeration systems with internal heat exchangers," *International Journal of Refrigeration,* vol. 28, pp. 1238-1249, 2005.

[32] S. C. Kim, J. P. Won and M. S. Kim, "Effects of operating parameters on the performance of a CO2 air conditioning system for vehicles," *Applied Thermal Engineering,* vol. 29, pp. 2408-2416, 2009.

[33] F. Xiaowei, X. Zhang, F. Wang and M. Qiang, "Experimental study of optimum heat rejection pressure for a CO2 heat pump water heater," in *Industrial Electronics and Applications (ICIEA), 2010 the 5th IEEE Conference on*, 2010.

[34] L. Cecchinato, M. Corradi and S. Minetto, "A critical approach to the determination of optimal heat rejection pressure in transcritical systems," *Applied Thermal Engineering,* vol. 30, pp. 1812-1823, 2010.

[35] X. P. Zhang, X. W. Fan, F. K. Wang and H. G. Shen, "Theoretical and experimental studies on optimum heat rejection pressure for a CO2 heat pump system," *Applied Thermal Engineering,* vol. 30, pp. 2537-2544, 2010.

[36] W.-J. Zhang and C.-L. Zhang, "A correlation-free on-line optimal control method of heat rejection pressures in CO2 transcritical systems," *International Journal of Refrigeration,* vol. 34, pp. 844-850, 2011.

[37] W.-J. Zhang, C.-L. Zhang and G.-L. Ding, "On three forms of momentum equation in transient modeling of residential refrigeration systems," *International Journal of Refrigeration,* vol. 32, pp. 938-944, 2009.

[38] L. Cecchinato, M. Corradi, G. Cosi, S. Minetto and M. Rampazzo, "A real-time algorithm for the determination of R744 systems optimal high pressure," *International Journal of Refrigeration,* vol. 35, pp. 817-826, 2012.

[39] P.-C. Qi, Y.-L. He, X.-L. Wang and X.-Z. Meng, "Experimental investigation of the optimal heat rejection pressure for a transcritical CO2 heat pump water heater," *Applied Thermal Engineering,* vol. 56, pp. 120-125, 2013.

[40] G. Boccardi, N. Calabrese, G. P. Celata, R. Mastrullo, A. W. Mauro, A. Perrone and R. Trinchieri, "Experimental performance evaluation for a carbon dioxide light commercial cooling application under transcritical and subcritical conditions," *Applied Thermal Engineering,* vol. 54, pp. 528-535, 2013.

[41] C. Baek, J. Heo, J. Jung, H. Cho and Y. Kim, "Optimal control of the gas-cooler pressure of a CO2 heat pump using EEV opening and outdoor fan speed in the cooling mode," *International Journal of Refrigeration,* vol. 36, pp. 1276-1284, 2013.

[42] M. S. Kim, C. S. Shin and M. S. Kim, "A study on the real time optimal control method for heat rejection pressure of a CO2 refrigeration system with an internal heat exchanger," *International Journal of Refrigeration,* vol. 48, pp. 87-99, 2014.

[43] I. Peñarrocha, R. Llopis, L. Tárrega, D. Sánchez and R. Cabello, "A new approach to optimize the energy efficiency of CO2 transcritical refrigeration plants," *Applied Thermal Engineering,* vol. 67, pp. 137-146, 2014.

[44] B. Hu, Y. Li, F. Cao and Z. Xing, "Extremum seeking control of COP optimization for air-source transcritical CO2 heat pump water heater system," *Applied Energy,* vol. 147, pp. 361-372, 2015.

[45] M. M. Hazarika, M. Ramgopal and S. Bhattacharyya, "Modelling And Simulation Of A R744 Based Air Conditioning Unit," in *Purdue International Refrigeration and Air Conditioning Conference*, West Lafayette, IN, 2016.

[46] J. L. Yang, Y. T. Ma and J. H. Zhang, "Optimal heat rejection pressure for transcritical CO2 refrigeration cycle with an expander," *International Journal of Green Energy,* vol. 13, pp. 208-212, 2016.

[47] S. Singh, N. Purohit and M. S. Dasgupta, "Comparative study of cycle modification strategies for trans-critical CO2 refrigeration cycle for warm climatic conditions," *Case Studies in Thermal Engineering,* vol. 7, pp. 78-91, 2016.

[48] K. Deb, A. Pratap, S. Agarwal and T. A. M. T. Meyarivan, "A fast and elitist multiobjective genetic algorithm: NSGA-II," *IEEE transactions on evolutionary computation,* vol. 6, pp. 182-197, 2002.

[49] A. Okasha and N. Müller, "Simulation and Performance Correlation for Transcritical CO2 Heat Pump Cycle," *International Refrigeration and Air Conditioning Conference,* p. 2643, 2018.

[50] T. M. Ortiz, D. Li and E. A. Groll, "Evaluation of the performance potential of CO2 as a refrigerant in air-to-air air conditioners and heat pumps: system modeling and analysis," *ARTI final report,* p. 10030, 2003.

[51] J. Sarkar, S. Bhattacharyya and M. Ramgopal, "A transcritical CO2 heat pump for simultaneous water cooling and heating: Test results and model validation," *International Journal of Energy Research,* vol. 33, pp. 100-109, 2009.

[52] T. Suzuki and K. Ishii, "Air conditioning system for electric vehicle," in *SAE Technical Paper,* 1996.

[53] D. E. Kramer, *Refrigeration system with suction line accumulator,* Google Patents, 1972.

[54] Parker Hannifin Corporation, *Accumulators and Receivers,* Parker, 2016.

[55] H. Rouse, Elementary Mechanics of Fluids, New York: John Wiley and Sons, 1946.

[56] L. F. Moody, "Friction factors for pipe flow," *Trans Asme,* vol. 66, pp. 671-684, 1944.

[57] N. H. Chen, "An explicit equation for friction factor in pipe," *Industrial & Engineering Chemistry Fundamentals,* vol. 18, pp. 296-297, 1979.

[58] C. F. Colebrook, T. Blench, H. Chatley, E. H. Essex, J. R. Finniecome, G. Lacey, J. Williamson and G. G. Macdonald, "Correspondence. Turbulent flow in pipes, with particular reference to the transition region between the smooth and rough pipe laws.(includes plates).," *Journal of the Institution of Civil engineers,* vol. 12, pp. 393-422, 1939.

[59] EnggCyclopedia, "Absolute Pipe Roughness," 2017. [Online]. Available: http://www.enggcyclopedia.com/2011/09/absolute-roughness/.

[60] D. Clamond, "Efficient resolution of the Colebrook equation," *Industrial & Engineering Chemistry Research,* vol. 48, pp. 3665-3671, 2009.

[61] F. a. a. R. B. Holland, Fluid Flow for Chemical Engineerings, 2nd edition, Edward Arnold, 1995.

[62] Coker, Ludwig's Applied Process Applied Process Design for Chemical Petrochemical Plants, Volume 1, Elsevier, 2007.

[63] Crane, Flow of Fluids through Valves, Fittings and Pipe, Crane Valve, 1991.

[64] B. Kilkovskỳ, Z. Jegla and P. Stehlík, "Comparison of Different Methods for Pressure Drop Calculation in 90o and 180o Elbows," *Chemical Engineering Transactions,* vol. 25, pp. 243-248, 2011.

[65] Blevins, Applied Fluid Dynamics Handbook, Reprint, Krieger Publishing Company, 2003.

[66] W. B. Hooper, "The 2-K Method Predicts Head Losses in Pipe Fittings," *Chemical Engineering,* vol. 88, pp. 96-100, 1981.

[67] Darby, "Correlate Pressure Drops through Fittings," *Chemical Engineering,* no. 108.4: 127-127, 2001.

[68] R. J. Dossat and T. J. Horan, Principles of Refrigeration, 2002.

[69] C. "Chilled water buffer tanks," 1999. [Online]. Available: http://cemline.com/images/document_library/brochures/pdf/cwb.pdfl.

[70] R. J. Moffat, "Using uncertainty analysis in the planning of an experiment.," pp. 173-178, 1985.

[71] R. Span and W. Wagner, "A new equation of state for carbon dioxide covering the fluid region from the triple-point temperature to 1100 K at pressures up to 800 MPa," *Journal of physical and chemical reference data,* vol. 25, pp. 1509-1596, 1996.